Title

LHC Dark Matter Working Group: Next-generation spin-0 dark matter models

Permalink

https://escholarship.org/uc/item/1px5g8wt

Authors

Abe, Tomohiro
Afik, Yoav
Albert, Andreas
et al.

Publication Date

2020

DOI

10.1016/j.dark.2019.100351

Peer reviewed

LHC Dark Matter Working Group:

Next-generation spin-0 dark matter models

Tomohiro Abe,[1,2] **Yoav Afik,**[3] **Andreas Albert,**[4]
Christopher R. Anelli,[5] **Liron Barak,**[6] **Martin Bauer,**[7]
J. Katharina Behr,[8] **Nicole F. Bell,**[9] **Antonio Boveia,**[10,*]
Oleg Brandt,[11] **Giorgio Busoni,**[9] **Linda M. Carpenter,**[10]
Yu-Heng Chen,[8] **Caterina Doglioni,**[12,*] **Alison Elliot,**[13]
Motoko Fujiwara,[14] **Marie-Helene Genest,**[15] **Raffaele Gerosa,**[16]
Stefania Gori,[17] **Johanna Gramling,**[18] **Alexander Grohsjean,**[8]
Giuliano Gustavino,[19] **Kristian Hahn,**[20,*] **Ulrich Haisch,**[21,22,23,*]
Lars Henkelmann,[11] **Junji Hisano,**[2,14,24] **Anders Huitfeldt,**[25]
Valerio Ippolito,[26] **Felix Kahlhoefer,**[27] **Greg Landsberg,**[28]
Steven Lowette,[29] **Benedikt Maier,**[30] **Fabio Maltoni,**[31]
Margarete Muehlleitner,[32] **Jose M. No,**[33,34] **Priscilla Pani,**[8,35]
Giacomo Polesello,[36] **Darren D. Price,**[37] **Tania Robens,**[38,39]
Giulia Rovelli,[40] **Yoram Rozen,**[3] **Isaac W. Sanderson,**[9]
Rui Santos,[41,42] **Stanislava Sevova,**[43] **David Sperka,**[44]
Kevin Sung,[20] **Tim M. P. Tait,**[17,*] **Koji Terashi,**[45]
Francesca C. Ungaro,[9] **Eleni Vryonidou,**[23] **Shin-Shan Yu,**[46]
Sau Lan Wu,[47] **and Chen Zhou.**[47]

[1]Institute for Advanced Research, Nagoya University,
Furo-cho Chikusa-ku, Nagoya, Aichi, 464-8602, Japan

[2]Kobayashi-Maskawa Institute for the Origin of Particles and the Universe,
Nagoya University, Furo-cho Chikusa-ku, Nagoya, Aichi, 464-8602, Japan

[3]Department of Physics, Technion: Israel Institute of Technology, Haifa, Israel

[4]III. Physikalisches Institut A, RWTH Aachen University,
Physikzentrum, Otto-Blumenthal-Straße, Aachen, Germany

[5]University of Victoria, Department of Physics and Astronomy,
Elliott Building, room 101, University of Victoria, Victoria, Canada

[6]Tel Aviv University, Haim Levanon (Ramat Aviv), Tel Aviv 69978, Israel

[7]Institute for Particle Physics Phenomenology, Department of Physics,
Durham University, South Road, Durham DH1 3LE, UK

[8]DESY, Notkestraße 85, D-22607 Hamburg, Germany

[9]ARC Centre of Excellence for Particle Physics at the Terascale
School of Physics, The University of Melbourne, Victoria 3010, Australia

[10]Ohio State University and Center for Cosmology and Astroparticle Physics,
191 W. Woodruff Avenue Columbus, OH 43210, USA

[11]Kirchhoff-Institut für Physik, Ruprecht-Karls-Universität Heidelberg,
Im Neuenheimer Feld 227, 69120 Heidelberg, Germany

[12]Fysiska institutionen, Lunds universitet, Professorsgatan 1, Lund, Sweden

[13]Department of Physics, Queen Mary University of London,
Mile End Rd, London E1 4NS, UK

[14]Department of Physics, Nagoya University, Furo-cho Chikusa-ku,
Nagoya, Aichi, 464-8602, Japan

[15]Univ. Grenoble Alpes, CNRS, Grenoble INP, LPSC-IN2P3, 38000 Grenoble, France

[16]University California San Diego (UCSD), Department of Physics,
9500 Gilman Drive, La Jolla, CA 92093-0319, USA

[17]Santa Cruz Institute for Particle Physics, 1156 High Street,
Santa Cruz, CA 95064, USA

[18]Department of Physics and Astronomy, University of California,
Irvine, California 92697, USA

[19]University of Oklahoma, 440 W. Brooks St. Norman, OK 73019, USA

[20]Department of Physics and Astronomy, Northwestern University,
Evanston, Illinois 60208, USA

[21]Max Planck Institute for Physics, Föhringer Ring 6, 80805 München, Germany

[22]Rudolf Peierls Centre for Theoretical Physics, University of Oxford,
Oxford, OX1 3PN, UK

[23]Theoretical Physics Department, CERN, CH-1211 Geneva 23, Switzerland

[24]Kavli IPMU (WPI), UTIAS, University of Tokyo, Kashiwa, Chiba 277-8584, Japan

[25]School of Physics, The University of Melbourne, Swanston St and Tin Alley,
Parkville, 3010, Victoria, Australia

[26]Università di Roma Sapienza and INFN, Piazza Aldo Moro, 2, 00185 Roma, Italy

[27]Institute for Theoretical Particle Physics and Cosmology (TTK),
RWTH Aachen University, D-52056 Aachen, Germany

[28]Brown University, Dept. of Physics, 182 Hope St, Providence, RI 02912, USA

[29]Vrije Universiteit Brussel, Pleinlaan 2, 1050 Brussel, Belgium

[30]Department of Physics, Massachusetts Institute of Technology, 77 Massachusetts Avenue,
Cambridge, MA 02139-4307, USA

[31]Centre for Cosmology, Particle Physics and Phenomenology (CP3),
Université catholique de Louvain, B-1348 Louvain-la-Neuve, Belgium

[32]Institute for Theoretical Physics, Karlsruhe Institute of Technology,
Wolfgang-Gaede-Str. 1, 76131 Karlsruhe, Germany

^{33}Departamento de Fisica Teorica and Instituto de Fisica Teorica, IFT-UAM/CSIC,
Universidad Autonoma de Madrid, Cantoblanco, 28049, Madrid, Spain

^{34}Department of Physics, King's College London, Strand, WC2R 2LS London, UK

^{35}DESY Zeuthen, Platanenallee 6, 15738 Zeuthen, Germany

^{36}INFN, Sezione di Pavia, Via Bassi 6, 27100 Pavia, Italy

^{37}School of Physics and Astronomy, University of Manchester, Manchester M13 9PL, UK

^{38}MTA-DE Particle Physics Research Group, University of Debrecen,
4010 Debrecen, Hungary

^{39}Theoretical Physics Division, Rudjer Boskovic Institute, 10002 Zagreb, Croatia

^{40}INFN Sezione di Pavia and Dipartimento di Fisica, Università di Pavia, Pavia, Italy.

^{41}ISEL - Instituto Superior de Engenharia de Lisboa,
Instituto Politécnico de Lisboa, 1959-007 Lisboa, Portugal

^{42}Centro de Física Teórica e Computacional, Faculdade de Ciências,
Universidade de Lisboa, Campo Grande, Edifício C8, 1749-016 Lisboa, Portugal

^{43}Stanford University, 450 Serra Mall, Stanford, CA 94305, USA

^{44}Boston University, 590 Commonwealth Avenue, 02215 Boston, MA, USA

^{45}International Center for Elementary Particle Physics (ICEPP), School of Science,
The University of Tokyo 7-3-1 Hongo, Bunkyo-ku, Tokyo 113-0033, Japan

^{46}Department of Physics, National Central University No. 300, Zhongda Rd.,
Zhongli District, Taoyuan City 32001, Taiwan

^{47}Department of Physics, University of Wisconsin, Thomas C Chamberlin Hall,
1150 University Ave 2320, Madison, WI 53706, USA

*DMWG organisers

Abstract. Dark matter (DM) simplified models are by now commonly used by the ATLAS and CMS Collaborations to interpret searches for missing transverse energy (E_T^{miss}). The coherent use of these models sharpened the LHC DM search program, especially in the presentation of its results and their comparison to DM direct-detection (DD) and indirect-detection (ID) experiments. However, the community has been aware of the limitations of the DM simplified models, in particular the lack of theoretical consistency of some of them and their restricted phenomenology leading to the relevance of only a small subset of E_T^{miss} signatures. This document from the LHC Dark Matter Working Group identifies an example of a next-generation DM model, called 2HDM+a, that provides the simplest theoretically consistent extension of the DM pseudoscalar simplified model. A comprehensive study of the phenomenology of the 2HDM+a model is presented, including a discussion of the rich and intricate pattern of mono-X signatures and the relevance of other DM as well as non-DM experiments. Based on our discussions, a set of recommended scans are proposed to explore the parameter space of the 2HDM+a model through LHC searches. The exclusion limits obtained from the proposed scans can be consistently compared to the constraints on the 2HDM+a model that derive from DD, ID and the DM relic density.

Contents

1 Introduction

Dark matter (DM) is one of the main search targets for LHC experiments (see for example [1] for a recent review). Based on the assumption that DM is a weakly interacting massive particle [2], the ATLAS and CMS Collaborations have searched for DM candidates manifesting as particles that escape the detectors, creating a sizeable transverse momentum imbalance (E_T^{miss}). Therefore, the minimal experimental signature of DM production at a hadron collider consists in an excess of events with a visible final-state object X recoiling against the E_T^{miss}, a so-called mono-X signal. The design of experimental searches for invisible particles can generally be kept independent from specific theoretical models, reflecting the lack of hints on the exact particle nature of DM. However, theoretical benchmarks are necessary to sharpen the regions of parameter space to which searches need to be optimised, to characterise a possible discovery and to define a theoretical framework for comparison with non-collider results.

Originally, supersymmetry was the main theoretical framework used as a benchmark for many DM searches at the LHC. Non-supersymmetric interpretations of the various E_T^{miss} searches have developed with time. At the start of data taking, DM effective field theories (DM-EFTs) were used due to their relative model independence [3–8]. DM simplified models, each representing a credible unit within a more complicated model and encapsulating the phenomenology of LHC DM interactions using a small set of parameters, provide more handles to study interactions when the momentum transfer of the collision is sufficient to probe the energy scale of a mediator particle. Further developments towards DM simplified models occurred before the start of the second LHC run [9, 10]. The coherent adoption of these DM simplified models by the LHC Collaborations focused the LHC DM search program, especially in the presentation of its results and their comparison to DM direct-detection (DD) and indirect-detection (ID) experiments [11, 12]. Throughout this time, the community has been aware of the shortcomings in DM simplified models, in particular the lack of theoretical consistency of some of them [13–19] and their limited phenomenology leading to the relevance of only a small set of experimental signatures.

With this white paper, we take a step beyond the proposed DM simplified models by identifying an example benchmark model and its parameters to be tested by LHC searches, with the following characteristics:

(I) the model should preferably be a theoretically consistent extension of one of the DM simplified models already used by the LHC Collaborations;

(II) the model should still be generic enough to be used in the context of broader, more complete theoretical frameworks;

(III) the model should have a sufficiently varied phenomenology to encourage comparison of different experimental signals and to search for DM in new, unexplored channels;

(IV) the model should be of interest beyond the DM community, to the point that other direct and indirect constraints can be identified.

One of the models that meets these characteristics and is explored in this white paper, referred to 2HDM+a in what follows, is a two-Higgs-doublet model (2HDM) containing an additional pseudoscalar boson which mediates the interactions between the visible and the dark sector. The 2HDM+a model is the simplest gauge-invariant and renormalisable extension of the simplified pseudoscalar model recommended by the ATLAS/CMS DM Forum (DMF) [10]. It includes a DM candidate which is a singlet under the Standard Model (SM) gauge group [20–24]. Since the DD constraints are weaker for models with pseudoscalar mediators compared to models with scalar mediators, the observed DM relic abundance can be reproduced in large regions of parameter space, making LHC searches particularly relevant to test the 2HDM+a or other pseudoscalar DM models.

In order to motivate the introduction of the 2HDM+a model, we describe in Section 2 the evolution of theories for LHC DM searches, focusing on the relevant case of pseudoscalar SM-DM interactions. A detailed description of the 2HDM+a model and its parameters can be found in Section 3. The constraints on the model parameters that arise from Higgs and flavour physics, LHC searches for additional spin-0 bosons, electroweak (EW) precision measurements and vacuum stability considerations are summarised in Section 4. This section also provides guidance on the choice of benchmark parameters to be used by LHC searches. Section 5 is dedicated to a short summary of other DM models that feature a 2HDM sector.

The more phenomenological part of this work commences with Section 6, where we describe the basic features of the most important mono-X channels and identify the experimental observables that can be exploited to search for them. We discuss both resonant and non-resonant E_T^{miss} signatures, emphasising that only the latter type of signals is present in the DMF pseudoscalar model. The most important non-E_T^{miss} signatures that can be used to explore the 2HDM+a parameter space are examined in Section 7. In Section 8 we then estimate the current experimental sensitivities in the mono-Higgs and mono-Z channel, which represent two of the most sensitive E_T^{miss} signatures for the 2HDM+a model. The constraints set on the parameter space of the 2HDM+a model from DD and ID experiments, as well as its DM relic density, are summarised in Section 9 and Section 10, respectively. In Section 11 we conclude by proposing four parameter scans that highlight many of the features that are special in the 2HDM+a model and showcase the complementarity of the various search strategies. Additional material can be found in the Appendices A, B, C and D.

2 Evolution of theories for LHC DM searches

The experimental results from DD and ID experiments are usually interpreted in the DM-EFT framework. The operators in these DM-EFTs are built from SM fermions and DM fields. Schematically, one has in the case of spin-0 interactions and Dirac fermion DM

$$\mathcal{L}_{\mathrm{DM\text{-}EFT}} = \sum_{f=u,d,s,c,b,t,e,\mu,\tau} \left(\frac{C_1^f}{\Lambda^2} \bar{f}f\bar{\chi}\chi + \frac{C_2^f}{\Lambda^2} \bar{f}\gamma_5 f\bar{\chi}\gamma_5\chi + \dots \right) , \qquad (2.1)$$
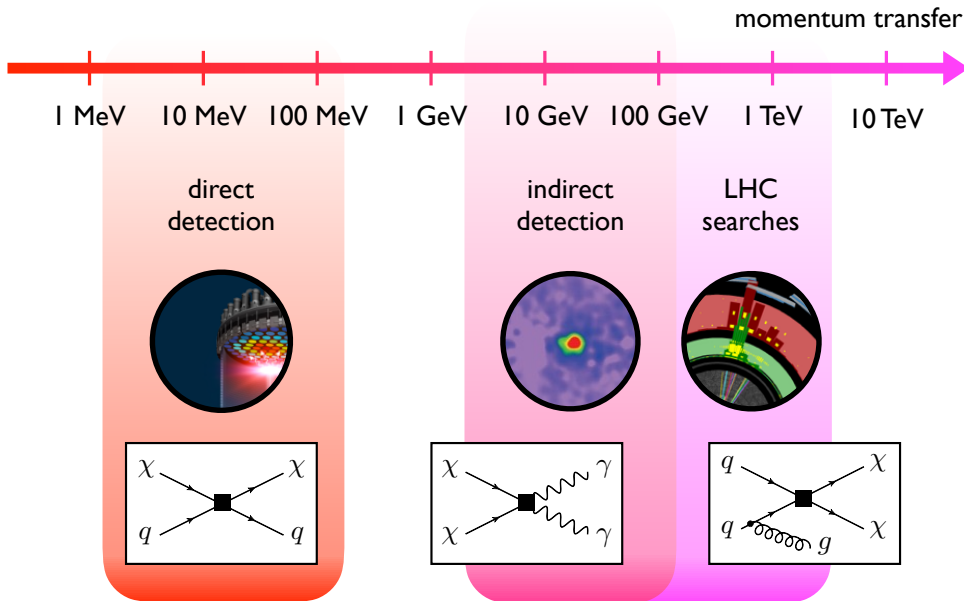
Figure 1: Range of momenta probed in DD experiments, ID experiments and LHC searches. Prototypes of relevant Feynman diagrams are also shown.

where the ellipsis represents additional operators not relevant for the further discussion, the sum over $f = u, d, s, c, b, t, e, \mu, \tau$ includes all SM quarks and charged leptons, the DM candidate is called χ and γ_5 denotes the fifth Dirac matrix. The above DM-EFT is fully described by the parameters

$$\left\{ m_\chi, \, C_n^f / \Lambda^2 \right\}. \tag{2.2}$$

Here m_χ is the mass of the DM candidate, Λ is the suppression scale of the higher-dimensional operators and the C_n^f are the so-called Wilson coefficients. It is important to note that Λ and C_n^f are not independent parameters but always appear in the specific combination given in (2.2).

The DM-EFT approach is justified for the small momentum transfer $q^2 \ll \Lambda^2$ in DM-nucleon scattering (set by the non-relativistic velocities of DM in the halo) and in DM annihilation (set by the mass of the annihilating DM candidate). Figure 1 illustrates the relevant energy scales explored by DD, ID and collider experiments. Early studies [3–8] of DM searches at colliders quantify the reach of the LHC in the parameter space in terms of (2.2) and similar operators. The momentum transfer at the LHC is however larger than the suppression scale, i.e. $q^2 \gg \Lambda^2$, for many theories of DM. In this case, the mediator of the interaction between the dark sector and the SM can be resonantly produced and predictions obtained using the DM-EFT framework often turn out to be inaccurate (see for instance [6, 25–31] and [32, 33] for exceptions).

The kinematics of on-shell propagators can be captured in DM simplified models, which aim to represent a large number of possible extensions of the SM, while keeping only the degrees of freedom relevant for LHC phenomenology [9, 10]. In the case of a

pseudoscalar mediator a, the relevant DM-mediator and SM-mediator interactions read

$$\mathcal{L}_{\text{DM-simp}} = -ig_\chi a\bar\chi\gamma_5\chi - ia\sum_j \left(g_u y_j^u \bar u_j \gamma_5 u_j + g_d y_j^d \bar d_j \gamma_5 d_j + g_\ell y_j^\ell \bar\ell_j \gamma_5 \ell_j\right), \qquad (2.3)$$

with j representing a flavour index. Since the mediator a is a singlet, it can also couple to itself and to $H^\dagger H$, where H denotes the SM Higgs doublet. The most general renormalisable scalar potential for a massive a is therefore

$$V_{\text{DM-simp}} = \frac{1}{2}m_a^2 a^2 + b_a a^3 + \lambda_a a^4 + b_H a H^\dagger H + \lambda_H a^2 H^\dagger H. \qquad (2.4)$$

The parameters b_H and λ_H determine the couplings between the a and the H fields, thereby altering the interactions of the SM-like scalar h at 125 GeV as well as giving rise to possible new decay channels such as $h \to aa$ (see [34, 35] for details on the LHC phenomenology). Avoiding the resulting strong constraints for any choice of m_a, requires that $b_H \ll m_a$ and $\lambda_H \ll 1$. While the former requirement can be satisfied by imposing a Z_2 symmetry $a \to -a$, in the latter case one has to assume that λ_H is accidentally small if $m_a \lesssim 100$ GeV (cf. the related discussion on invisible decays of the Higgs boson in Section 4.4). Under such an assumption and noting that the self-couplings b_a and λ_a are largely irrelevant for collider phenomenology, the DM simplified model is fully described by the parameters

$$\left\{m_\chi,\ m_a,\ g_\chi,\ g_u,\ g_d,\ g_\ell\right\}. \qquad (2.5)$$

In fact, in the limit of infinite mediator mass $m_a \to \infty$, the DM-simp Lagrangian (2.3) matches onto the DM-EFT Lagrangian (2.1). The corresponding tree-level matching conditions are $C_2^f/\Lambda^2 = g_\chi g_f y_f/m_a^2$ and $C_n^f = 0$ for all other Wilson coefficients. Here y_f denotes the Yukawa couplings of the fermions f entering (2.3).

Unfortunately, the operators in both $\mathcal{L}_{\text{DM-EFT}}$ and $\mathcal{L}_{\text{DM-simp}}$ violate gauge invariance, because the left- and right-handed SM fermions belong to different representations of the SM gauge group. In the case of the DM-EFT this suggests the Wilson coefficients C_n^f introduced in (2.1) actually scale as $C_n^f = c_n^f m_{f_i}/\Lambda$ [14], whereas for the DM simplified model restoring gauge invariance requires the embedding of the mediator a into an EW multiplet. The absence of gauge invariance leads to unitarity-violating amplitudes in DM simplified models (cf. [14, 16–18, 36, 37]). In the case of the DM simplified model described by (2.3), one can show e.g. that the amplitudes $\mathcal{A}(qb \to q'ta) \propto \sqrt{s}$ and $\mathcal{A}(gg \to Za) \propto \ln^2 s$ diverge in the limit of large center-of-mass energy $\sqrt{s}$. The Feynman diagrams that lead to this behaviour are depicted on the left-hand side in Figure 2. Similar singularities appear in other single-top processes and in the mono-Higgs case. Since the divergences are not power-like, weakly-coupled realisations of (2.3) do not break down for the energies accessible at the LHC. The appearance of the $\sqrt{s}$ and $\ln^2 s$ terms, however, indicates the omission of diagrams that would be present in any gauge-invariant extension that can be approximated by $\mathcal{L}_{\text{DM-EFT}}$ in the limit where all additional particles X are heavy (i.e. $M_X \gg \sqrt{s}$). For example, the $pp \to tja$ cross section is made finite by the exchange of a charged Higgs $H^\pm$, while in the case of $pp \to Za$ an additional scalar H unitarises the amplitude. The corresponding diagrams are displayed on the right in Figure 2. The
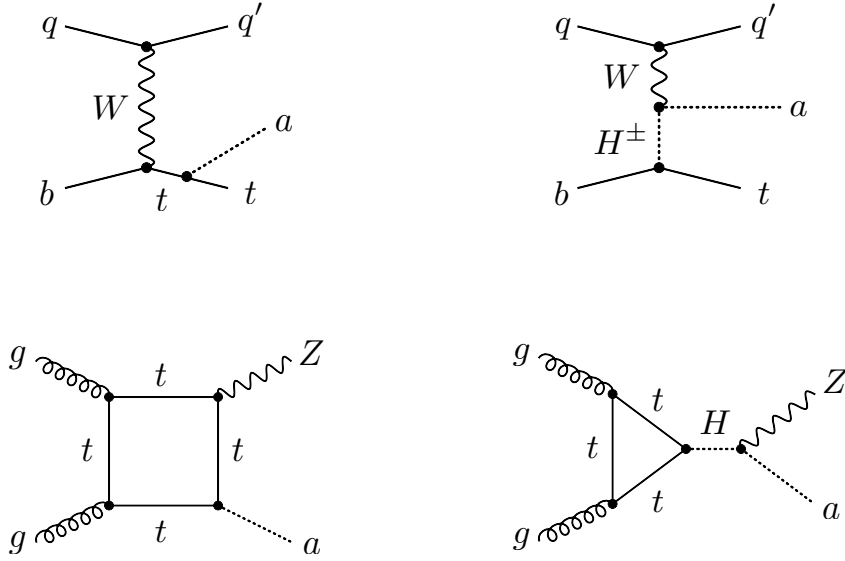
Figure 2: Diagrams contributing to the $qb \to q'ta$ (upper row) and $gg \to Za$ (lower row) scattering processes. Only the graphs on the left-hand side appear in the DM simplified model with a pseudoscalar, while in the 2HDM+a model in addition the diagrams on the right-hand side are present. See text for further details.

cancellation of unitarity-violating terms among the diagrams of the latter figure is not at all accidental, but a direct consequence of the local gauge invariance of the underlying model.

The additional degrees of freedom necessary to unitarise the amplitudes may change substantially the phenomenology of the DM simplified model. In fact, as shown by Figure 2, the presence of the $H^\pm$ (H) allows to produce a mono-top (mono-Z) signal resonantly. Since resonant production is strongly enhanced compared to initial-state radiation (ISR), the importance of the various mono-X signals in the extended DM model may then differ from the simplified model predictions [22, 23, 38]. In fact, we will see that in a specific extension of (2.3) called 2HDM+a model, the mono-Higgs, mono-Z and $tX + E_T^{\mathrm{miss}}$ signals can be as or even more important than the $t\bar{t} + E_T^{\mathrm{miss}}$ and mono-jet channel, which are the leading E_T^{miss} signatures in the DM simplified pseudoscalar model [39–47]. We emphasise that the embedding of (2.3) is not unique, since both the mediator and the DM particle can belong to different EW multiplets. In this white paper, we consider the simplest embedding with a single SM-singlet DM candidate, but we will briefly comment on other possible embeddings and related DM models in Section 5.

3   Description of the 2HDM+a model

The 2HDM+a model is a 2HDM that contains, besides the Higgs doublets H_1 and H_2, an additional pseudoscalar singlet P. It is the simplest renormalisable extension of (2.3) with an SM-singlet DM candidate [20–24]. The gauge symmetry is made manifest by coupling

the P to the dark Dirac fermion χ via

$$\mathcal{L}_\chi = -iy_\chi P\bar{\chi}\gamma_5\chi\,, \tag{3.1}$$

while the Higgs doublets couple to the SM fermions through

$$\mathcal{L}_Y = -\sum_{i=1,2}\left(\bar{Q}Y_u^i\tilde{H}_iu_R + \bar{Q}Y_d^iH_id_R + \bar{L}Y_\ell^iH_i\ell_R + \text{h.c.}\right)\,. \tag{3.2}$$

Here y_χ is a dark-sector Yukawa coupling, Y_f^i are Yukawa matrices acting on the three fermion generations (where indices concerning the flavour of the fermion are suppressed), Q and L are left-handed quark and lepton doublets, while u_R, d_R and ℓ_R are right-handed up-type quark, down-type quark and charged lepton singlets, respectively. Finally, $\tilde{H}_i = \epsilon H_i^*$ with ϵ denoting the two-dimensional antisymmetric tensor.

The particle that mediates the interactions between the dark sector and the SM is a superposition of the CP-odd components of H_1, H_2 and P. We impose a Z_2 symmetry under which $H_1 \to H_1$ and $H_2 \to -H_2$, such that only one Higgs doublet couples to a certain fermion in $\mathcal{L}_Y$. The different ways to construct these terms result in different Yukawa structures and in this white paper we will, for concreteness, consider only the so-called type-II 2HDM. This specific choice corresponds to setting $Y_u^1 = Y_d^2 = Y_\ell^2 = 0$ in (3.2) — see for example Section 2.2 of [23] for further explanations. The Z_2 symmetry is the minimal condition necessary to guarantee the absence of flavour-changing neutral currents at tree level [48, 49] and such a symmetry is realised at in many well-motivated complete ultraviolet (UV) theories in the form of supersymmetry, a $U(1)$ symmetry or a discrete symmetry acting on the Higgs doublets. The fields P and χ are Z_2-even and Z_2-odd, respectively, i.e. they transform as $P \to P$ and $\chi \to -\chi$. For these choices, the coupling introduced in (3.1) is the only DM Yukawa coupling that is allowed by symmetry, since a term of the form $\bar{L}\tilde{H}_1\chi_R + \text{h.c.}$ is forbidden.

In addition, all parameters in the scalar potential are chosen to be real, such that CP eigenstates are identified with the mass eigenstates, i.e. two scalars h and H, two pseudoscalars A and a and a charged scalar $H^\pm$. Under these conditions, the most general renormalisable scalar potential can be written as

$$V = V_H + V_{HP} + V_P\,, \tag{3.3}$$

with the potential for the two Higgs doublets

$$\begin{aligned}
V_H = {} & \mu_1 H_1^\dagger H_1 + \mu_2 H_2^\dagger H_2 + \left(\mu_3 H_1^\dagger H_2 + \text{h.c.}\right) + \lambda_1\left(H_1^\dagger H_1\right)^2 + \lambda_2\left(H_2^\dagger H_2\right)^2 \\
& + \lambda_3\left(H_1^\dagger H_1\right)\left(H_2^\dagger H_2\right) + \lambda_4\left(H_1^\dagger H_2\right)\left(H_2^\dagger H_1\right) + \left[\lambda_5\left(H_1^\dagger H_2\right)^2 + \text{h.c.}\right],
\end{aligned} \tag{3.4}$$

where the terms $\mu_3 H_1^\dagger H_2 + \text{h.c.}$ softly break the Z_2 symmetry. The potential terms which connect doublets and singlets are

$$V_{HP} = P\left(ib_P H_1^\dagger H_2 + \text{h.c.}\right) + P^2\left(\lambda_{P1}H_1^\dagger H_1 + \lambda_{P2}H_2^\dagger H_2\right), \tag{3.5}$$

where the first term breaks the Z_2 symmetry softly. The singlet potential is given by

$$V_P = \frac{1}{2} m_P^2 P^2 \,. \tag{3.6}$$

Notice that compared to [20–22, 24], which include only the trilinear portal coupling b_P, we follow [23] and also allow for quartic portal interactions proportional to λ_{P1} and λ_{P2}. A quartic self-coupling P^4 has not been included in (3.6), because such a term would not lead to any relevant effect in the E_T^{miss} observables studied in this white paper.

Upon rotation to the mass eigenbasis, we trade the five dimensionful and the eight dimensionless parameters in the potential for physical masses, mixing angles and four quartic couplings:

$$\left\{ \begin{array}{c} \mu_1, \, \mu_2, \, \mu_3, \, b_P, \, m_P, \, m_\chi \\ y_\chi, \, \lambda_1, \, \lambda_2, \, \lambda_3, \, \lambda_4, \, \lambda_5, \\ \lambda_{P1}, \, \lambda_{P2} \end{array} \right\} \quad \longleftrightarrow \quad \left\{ \begin{array}{c} v, \, M_h, \, M_A, \, M_H, \, M_{H^\pm}, \, M_a, \, m_\chi \\ \cos(\beta - \alpha), \, \tan\beta, \, \sin\theta, \\ y_\chi, \, \lambda_3, \, \lambda_{P1}, \, \lambda_{P2} \end{array} \right\} \,. \tag{3.7}$$

Here α denotes the mixing angle between the two CP-even weak spin-0 eigenstates, $\tan\beta$ is the ratio of the vacuum expectation values (VEVs) of the two Higgs doublets and θ represents the mixing angle of the two CP-odd weak spin-0 eigenstates. The parameters shown on the right-hand side of (3.7) will be used as input in the following sections. Out of these parameters, the EW VEV $v \simeq 246\,\mathrm{GeV}$ and the mass of the SM-like CP-even mass eigenstate $M_h \simeq 125\,\mathrm{GeV}$ are already fixed by observations. The experimental and theoretical constraints on the remaining parameter space will be examined in the next section.

4 Constraints on the 2HDM+a parameter space

In the following we examine the constraints on the input parameters (3.7) that arise from Higgs and flavour physics, LHC searches for additional spin-0 bosons, EW precision measurements and vacuum stability considerations. The discussed constraints will motivate certain parameter benchmarks, which will be summarised at the end of the section.

4.1 Constraints on $\cos(\beta - \alpha)$

The mixing angle α between the CP-even scalars h and H is constrained by Higgs coupling strength measurements and we display the regions in the $\cos(\beta - \alpha)$–$\tan\beta$ plane that are allowed by the LHC Run-I combination [50] in the left panel of Figure 3. See [51, 52] for the latest 13 TeV LHC results. The 95% confidence level (CL) contour shown has been obtained in the type-II 2HDM. For arbitrary values of $\tan\beta$, only parameter choices with $\cos(\beta - \alpha) \simeq 0$ are experimentally allowed. Additional exclusion limits in the $\cos(\beta - \alpha)$–$\tan\beta$ plane arise from searches for $A \to hZ$ [53, 54]. To avoid the constraints from Higgs physics and to simplify the further analysis, we will concentrate in this white paper on the so-called alignment limit of the 2HDM where $\cos(\beta - \alpha) = 0$ [55], treating $\tan\beta$ as a free parameter. In this limit the constraints from $A \to hZ$ are satisfied as well because the AhZ coupling scales as $g_{AhZ} \propto \cos(\beta - \alpha)$.
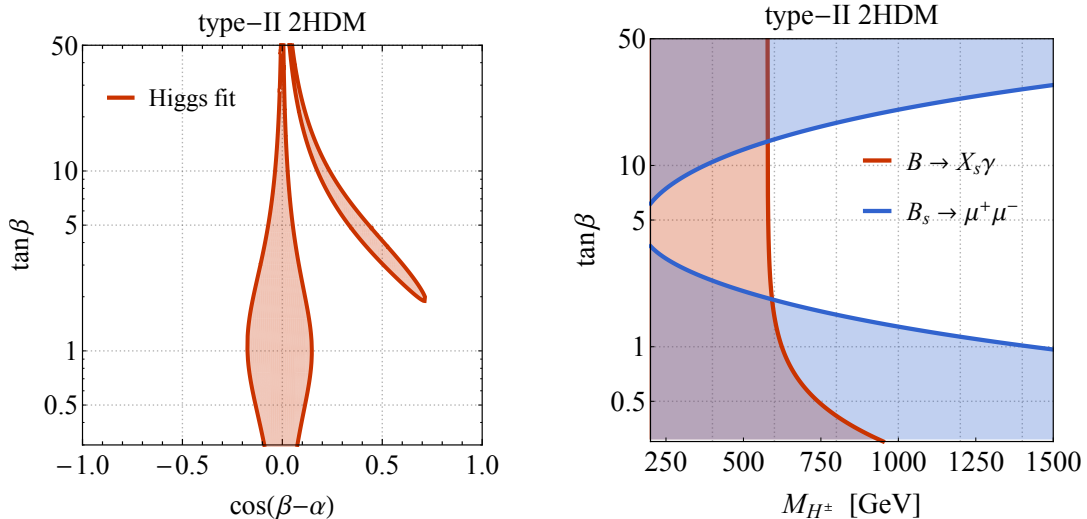
Figure 3: Left: Parameter space allowed, at 95% CL, by a global fit to the LHC Run-I Higgs coupling strength measurements in the context of a 2HDM type-II scenario. Right: Parameter space in the $M_{H^\pm} - \tan\beta$ plane that is disfavoured by the flavour observables $B \to X_s \gamma$ (red) and $B_s \to \mu^+ \mu^-$ (blue). The open region in the center of the plot is allowed at 95% CL.

4.2 Constraints on $\tan\beta$

Indirect constraints on $\tan\beta$ as a function of $M_{H^\pm}$ arise from $B \to X_s\gamma$ [56–58], B-meson mixing [59–62] as well as $B_s \to \mu^+\mu^-$ [63–69], but also follow from $Z \to b\bar{b}$ [70–72]. For the case of the type-II 2HDM, the most stringent constraints on the $M_{H^\pm} - \tan\beta$ plane are depicted in the right panel of Figure 3. From the shown results it is evident that $B \to X_s\gamma$ provides a lower limit on the charged Higgs mass of $M_{H^\pm} > 580\,\text{GeV}$ that is practically independent of $\tan\beta$ for $\tan\beta \gtrsim 2$, while $B_s \to \mu^+\mu^-$ is the leading constraint for very heavy charged Higgses, excluding for instance values of $\tan\beta < 1.3$ and $\tan\beta > 20$ for $M_{H^\pm} = 1\,\text{TeV}$. Since the indirect constraints arise from loop corrections they can in principle be weakened by the presence of additional particles that are too heavy to be produced at the LHC. We thus consider the bounds from flavour only as indicative, and will not directly impose them on the parameter space of the 2HDM+a in what follows. The constraints on $\tan\beta$ that follow from the existing LHC searches for heavy spin-0 bosons (see for instance [73–75, 77, 78]) will be discussed in Section 7.

4.3 Constraints on $\sin\theta$

EW precision measurements constrain the differences between the masses of the additional scalar and pseudoscalar particles $M_H, M_A, M_{H^\pm}$ and M_a, because the exchange of spin-0 states modifies the propagators of the W- and Z-bosons at the one-loop level and beyond. For $M_H = M_{H^\pm}$ and $\cos(\beta - \alpha) = 0$, these corrections vanish due to a custodial symmetry in the tree-level potential V_H [79–83] introduced in (3.4) and the masses of the CP-odd mass eigenstates can be treated as free parameters. This custodial symmetry is also present if

$M_A = M_{H^\pm}$ and $\cos(\beta - \alpha) = 0$, but the presence of the pseudoscalar mixing term in (3.5) breaks this symmetry softly [23]. As a result, the pseudoscalar mixing angle θ and the mass splitting between M_H, M_A and M_a are constrained in such a case. An illustrative example of the resulting constraints is given in the left panel of Figure 4. To keep $\sin\theta$ and M_a as free parameters, we consider below only 2HDM+a model configurations in which the masses of the H, A and $H^\pm$ are equal. The choice $M_H = M_A = M_{H^\pm}$ is also adopted in some 2HDM interpretations of the searches for heavy spin-0 resonances performed at the LHC (cf. [84–86] for example).

4.4 Constraints on M_a

Invisible decays of the Higgs boson allow to set a lower limit on the mass of the pseudoscalar a in 2HDM+a scenarios with light DM [23]. In the case of $m_\chi = 1\,\text{GeV}$, it turns out for instance that mediator masses $M_a \lesssim 100\,\text{GeV}$ are excluded by imposing the 95% CL limit on the branching ratio $\text{BR}(h \to \text{invisible}) \lesssim 25\%$ [87, 88]. This limit is largely independent of the choices of the other parameters since $\text{BR}(h \to \text{invisible}) \simeq \text{BR}(h \to aa^* \to 2\chi 2\bar{\chi}) \simeq 100\%$ for sufficiently light DM, unless the haa coupling, which for $\cos(\beta - \alpha) = 0$ and $M_H = M_{H^\pm}$ takes the following form [23]

$$g_{haa} = \frac{1}{M_h v} \left[\left(M_h^2 + 2M_H^2 - 2M_a^2 - 2\lambda_3 v^2 \right) \sin^2\theta \right.$$
$$\left. - 2 \left(\lambda_{P1} \cos^2\beta + \lambda_{P2} \sin^2\beta \right) v^2 \cos^2\theta \right], \tag{4.1}$$

is sufficiently suppressed by tuning, i.e. $|g_{haa}| \ll 1$. To evade the limits from invisible Higgs decays, we consider in this white paper only M_a values larger than $100\,\text{GeV}$ when studying E_T^{miss} signatures at the LHC.

4.5 Constraints on λ_3

The requirement that the scalar potential (3.3) of the 2HDM+a is bounded from below (BFB) restricts the possible choices of the spin-0 boson masses, mixing angles and quartic couplings. Assuming that $\lambda_{P1}, \lambda_{P2} > 0$, the BFB conditions in the 2HDM+a model turn out to be identical to those found in the pure 2HDM [55]. For our choice $M_H = M_A = M_{H^\pm}$ of heavy spin-0 boson masses, one finds that the tree-level BFB conditions can be cast into two inequalities. The first inequality connects λ_3 with the cubic SM Higgs self-coupling $\lambda = M_h^2/(2v^2) \simeq 0.13$ and simply reads

$$\lambda_3 > 2\lambda. \tag{4.2}$$

The second BFB condition relates λ_3 with $\tan\beta$, $\sin\theta$, the common heavy spin-0 boson mass M_H and M_a. In the limit $M_H \gg M_h, M_a$ it takes a rather simple form that we quote here for illustration:

$$\lambda_3 > \frac{M_H^2 - M_a^2}{v^2} \sin^2\theta - 2\lambda \cot^2(2\beta). \tag{4.3}$$

This formula implies that large values of $M_H^2/v^2 \sin^2\theta$ are only compatible with the requirements from BFB if the quartic coupling λ_3 is sufficiently large. The interplay between
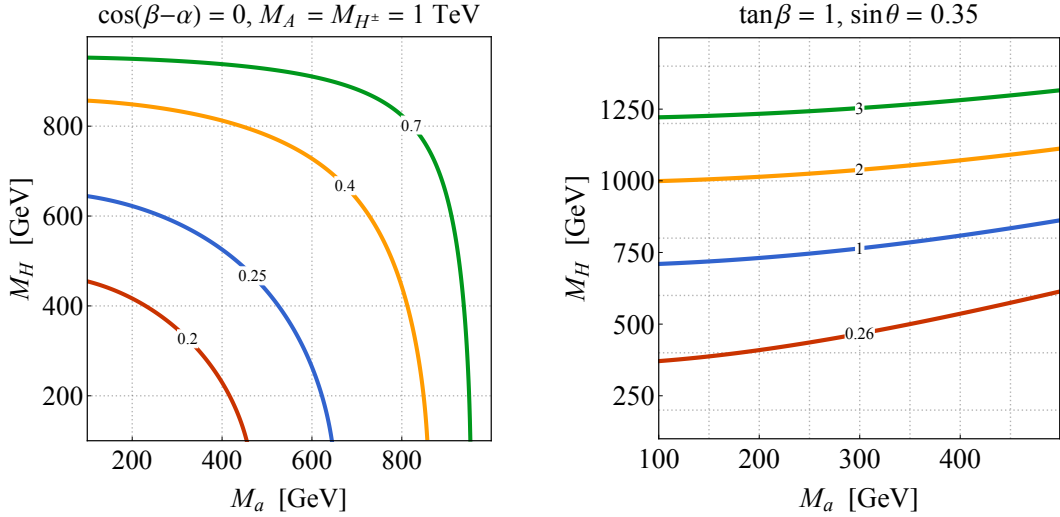
Figure 4: Left: Values of M_a and M_H allowed by EW precision constraints assuming $\cos(\beta - \alpha) = 0$, $M_A = M_{H^\pm} = 1\,\text{TeV}$ and four different values of $\sin\theta$, as indicated by the contour labels. The parameter space below and to the left of the contours is excluded. Right: Constraints in the M_a–M_H plane following from the BFB requirement. The results shown correspond to $\tan\beta = 1$, $\sin\theta = 0.35$ and degenerate heavy spin-0 boson masses $M_H = M_A = M_{H^\pm}$. The region above each contour is excluded for the indicated value of the quartic coupling λ_3.

BFB and perturbativity of λ_3, i.e. $\lambda_3 < 4\pi$, leads to a non-decoupling of H, A and $H^\pm$ for $|M_H - M_a| \neq 0$ and $\sin\theta \neq 0$ [22] such that the spin-0 states are potentially within LHC reach. The right plot in Figure 4 which shows the constraints in the M_a–M_H plane that derive from the exact version of (4.3) confirms the latter statement. For $\tan\beta = 1$, $\sin\theta = 0.35$ and $M_H = M_A = M_{H^\pm}$, values of $\lambda_3 \gtrsim 2$ are needed in order for $M_H \simeq 1\,\text{TeV}$ to be allowed by BFB. Due to the $\sin^2\theta$ dependence in (4.3), a common 2HDM spin-0 boson mass of $M_H = M_A = M_{H^\pm} \simeq 1\,\text{TeV}$ would only be viable for $\sin\theta = 0.7$ if the quartic coupling λ_3 takes close to non-perturbative values $\lambda_3 \gtrsim 8$. In order to allow for heavy Higgs above $1\,\text{TeV}$ to be acceptable while keeping λ_3 perturbative, we will choose $\sin\theta = 0.35$ and $\lambda_3 = 3$ as our benchmark in this white paper.

4.6 Constraints on λ_{P1} and λ_{P2}

The quartic couplings λ_3, λ_{P1} and λ_{P2} affect all cubic Higgs interactions. In the case of the Haa and Aha couplings, one obtains under the assumption that $\cos(\beta - \alpha) = 0$ and $M_H = M_A = M_{H^\pm}$, the following expressions [23]

$$
\begin{aligned}
g_{Haa} &= \frac{1}{M_H v}\left[\cot(2\beta)\left(2M_h^2 - 2\lambda_3 v^2\right)\sin^2\theta + \sin(2\beta)\left(\lambda_{P1} - \lambda_{P2}\right)v^2\cos^2\theta \right], \\
g_{Aha} &= \frac{1}{M_H v}\left[M_h^2 + M_H^2 - M_a^2 - 2\lambda_3 v^2 + 2\left(\lambda_{P1}\cos^2\beta + \lambda_{P2}\sin^2\beta\right)v^2 \right]\sin\theta\cos\theta\,.
\end{aligned}
\tag{4.4}
$$

Because $\Gamma(H \to aa) \propto g_{Haa}^2$ and $\Gamma(A \to ha) \propto g_{Aha}^2$, the relations (4.4) imply that in order to keep the total widths Γ_H and Γ_A small, parameter choices of the form $\lambda_3 = \lambda_{P1} = \lambda_{P2}$ are well suited.

4.7 Benchmark parameter choices

The above discussion motivates the following choice of parameters

$$M_H = M_A = M_{H^\pm}, \quad m_\chi = 10\,\mathrm{GeV},$$
$$\cos(\beta - \alpha) = 0, \quad \tan\beta = 1, \quad \sin\theta = 0.35, \quad (4.5)$$
$$y_\chi = 1, \quad \lambda_3 = \lambda_{P1} = \lambda_{P2} = 3.$$

For the choices $m_\chi = 10\,\mathrm{GeV}$ and $y_\chi = 1$ the branching ratio $\mathrm{BR}(a \to \chi\bar\chi)$ is sizeable for all values of M_a considered in this white paper, i.e. $M_a > 100\,\mathrm{GeV}$. For masses below the top threshold of around $350\,\mathrm{GeV}$, $a \to t\bar t$ is kinematically forbidden and therefore $\mathrm{BR}(a \to \chi\bar\chi)$ can be as large as 100%. The choice of $y_\chi = 1$ is thereby largely arbitrary for the mono-X phenomenology, which is not the case for the DD and ID cross sections where the magnitude of y_χ plays an important role. This feature has to be kept in mind when performing a comparison between LHC and DD/ID constraints. Concerning the mono-Higgs and mono-Z signals in the 2HDM+a model it is furthermore important to realise that the relevant couplings scale as $g_{Aha} \propto \sin\theta \cos\theta$ (cf. (4.4)) and $g_{HZa} \propto \sin\theta$. Since in addition $g_{t\bar t a} \propto \sin\theta$, it follows that in the limit $\sin\theta \to 0$ all mono-X signatures vanish. In order to obtain detectable LHC signals involving E_T^{miss}, we have chosen $\sin\theta = 0.35$ in the above benchmark parameter scenario. We furthermore add that since $\tan\beta$ has been set equal to 1 in (4.5), most of the results presented in this white paper are independent of the type chosen for the 2HDM+a Yukawa sector.

In the type-II 2HDM+a benchmark scenario (4.5) the only free parameters are M_H and M_a. We will study the sensitivity of the existing mono-X searches in the corresponding two-dimensional parameter plane in Section 8. Parameter scans in the M_a–$\tan\beta$ plane can also be found in this section. In these latter scans, the choices (4.5) are adopted except for $\tan\beta$, which is not fixed to 1 anymore but allowed to vary freely, as well as

$$M_H = M_A = M_{H^\pm} = 600\,\mathrm{GeV}. \quad (4.6)$$

Since the $g_{b\bar b A}$ and $g_{b\bar b a}$ couplings are $\tan\beta$-enhanced in the type-II 2HDM+a model, effects from $b\bar b$-initiated production can be relevant for $\tan\beta \gg 1$. Such $\tan\beta$-enhanced contributions will be included in our sensitivity studies of the mono-Higgs and mono-Z channels to be presented in Section 8.

At this point it is worthwhile to add that the mono-X signatures that are most sensitive to the mass splitting between the H and the A, the parameter $\sin\theta$ and the quartic couplings λ_3, λ_{P1}, λ_{P2} turn out to be the mono-Higgs and mono-Z channels (see Section 6 for details). Four benchmark scenarios that illustrate these model dependencies have been proposed and studied in [23]. We believe that the specific benchmarks chosen in (4.5) and (4.6) exemplify the rich structure of E_T^{miss} signatures in the 2HDM+a model, and they
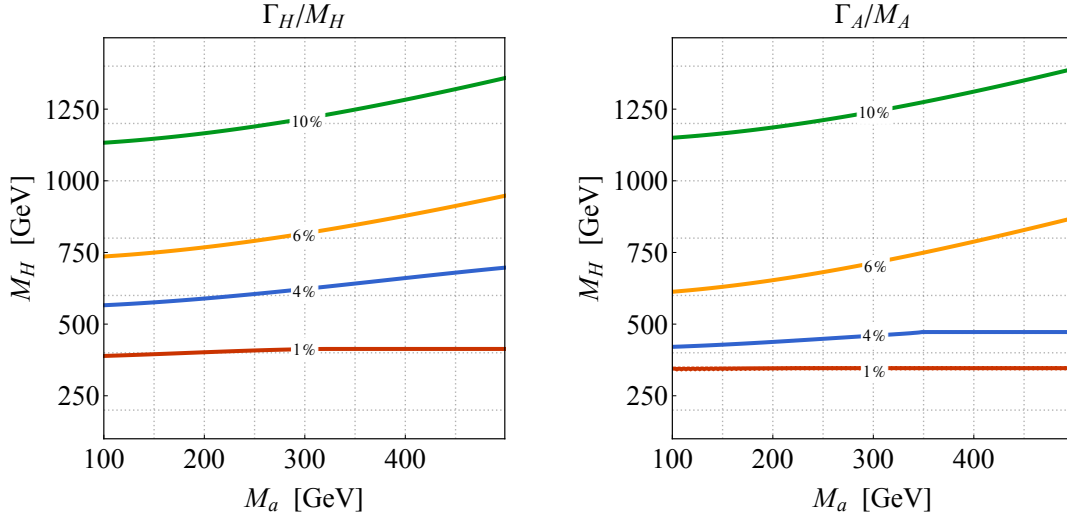
Figure 5: Predictions for Γ_H/M_H (left panel) and Γ_A/M_A (right panel). The results shown correspond to the type-II 2HDM+a benchmark parameter choices given in (4.5).

should therefore serve well as a starting point for further more detailed experimental and theoretical investigations.

As a final validation (or first application) of the proposed benchmark scenario, we present in Figure 5 the predictions for the ratios Γ_H/M_H (left) and Γ_A/M_A (right). We see that the heavy neutral Higgs states H and A are relatively narrow even for values $M_H > 1\,\text{TeV}$ and $M_a = 100\,\text{GeV}$. The narrow width assumption is thus justified in the entire parameter space considered in our M_a–M_H scans.

5   Comparison to other DM models

In this section we briefly discuss DM models that also feature a 2HDM sector. Our discussion will focus on the similarities and differences between these scenarios and the 2HDM+a model concerning the mono-X phenomenology.

5.1   2HDM with an extra scalar singlet

Instead of mixing an additional CP-odd singlet P with the pseudoscalar A, as done in (3.5), it is also possible to consider the mixing of a scalar singlet S with the CP-even spin-0 states h, H. Detailed studies of the DD and relic-density phenomenology of this so-called 2HDM+s model have been presented in [89, 90]. Like in the case of the 2HDM+a model, the presence of non-SM Higgs bosons in the 2HDM+s model can lead to novel E_T^{miss} signatures that are not captured by a DM simplified model with just a single scalar mediator. In the pure alignment limit, i.e. $\cos(\beta - \alpha) = 0$, the most interesting collider signals are mono-Higgs, mono-Z and the $tX + E_T^{\text{miss}}$ channels, because these signatures can all arise resonantly. In fact, the relevant one-loop diagrams are precisely those that lead to the leading mono-X signals in the 2HDM+a model (see Figure 6), and in consequence resonant

E_T^{miss} searches that can constrain the 2HDM+a model could also be interpreted in the 2HDM+s context. Away from alignment, the scalar mediator couples to the EW gauge bosons and as a result it may also be possible to have a sizeable amount of E_T^{miss} in association with a Z or W boson or in vector boson fusion (VBF). Due to the CP properties of the a, the latter tree-level E_T^{miss} signatures are not present in the 2HDM+a model.

5.2   2HDM with singlet-doublet DM

In both the 2HDM+a and the 2HDM+s model the DM particle is an EW singlet. The DM particle may, however, also be a mixture of an EW singlet and doublet(s) [91–94], as in the minimal supersymmetric SM with both bino and higgsino components. Generically, this model is referred to as singlet-doublet DM. The phenomenology of 2HDM models with singlet-doublet DM has been discussed in [95, 96], where only the $b + E_T^{\mathrm{miss}}$ and $t\bar{t} + E_T^{\mathrm{miss}}$ signatures have been considered and found to provide only weak constraints. Additionally, a recent study [97] suggests that $b + E_T^{\mathrm{miss}}$ and $tX + E_T^{\mathrm{miss}}$ may give stronger constraints in the 2HDM with singlet-doublet DM for scenarios in which the additional scalars have a mass not too far above the pseudoscalar mass.

5.3   2HDM with higher-dimensional couplings to DM

A gauge-invariant DM model where a pseudoscalar is embedded into a 2HDM that has renormalisable couplings to SM fields but an effective coupling to DM via the dimension-five operator $H_1^\dagger H_2 \bar{\chi} \gamma_5 \chi$ has been discussed in [97]. It has been shown that such an effective DM coupling can be obtained in different UV completions such as the 2HDM+a model or a 2HDM with singlet-doublet DM by integrating out heavy particles. Apart from the $tX + E_T^{\mathrm{miss}}$ signatures, the whole suite of mono-X signals has been considered in [97]. It was found that a resonant mono-Z signal via $pp \to H \to AZ \to Z + \chi\bar{\chi}$ is a universal prediction in all DM pseudoscalar mediator models, while other signatures such as mono-Higgs are model dependent. Given that a sizeable $H^\pm \to AW$ rate is also a generic feature of DM pseudoscalar models if $M_{H^\pm} > M_A + M_W$, channels like $tW + E_T^{\mathrm{miss}}$ [38] should also provide relevant constraints on the DM model introduced in [97].

5.4   Inert doublet model

In the scenarios discussed so far the DM particle has always been a fermion. The so-called inert doublet model (IDM) [98–100] is a DM model based on a 2HDM sector that can provide DM in the form of the spin-0 resonances H, A. The presence of a Z_2 symmetry renders the DM candidate stable and also implies that the bosonic states originating from the second (dark) Higgs doublet can only be pair-produced. Since the dark scalars do not couple to the SM fermions, $H, A, H^\pm$ production arises in the IDM dominantly from Drell-Yan processes. The IDM offers a rich spectrum of LHC E_T^{miss} signatures that ranges from mono-jet, mono-Z, mono-W, mono-Higgs to VBF + E_T^{miss} [101–112]. While the prospects to probe the IDM parameter space via the mono-jet channel seem to be limited [110], LHC searches for multiple leptons [101–104, 107, 108], multiple jets [106, 111] or a combination thereof [108, 112] are expected to probe the IDM parameter space in regions that are not accessible by DD experiments of DM or measurements of the invisible decay width of

the SM Higgs. Furthermore, in scenarios in which the mass of DM is almost degenerate with $M_{H^\pm}$, searches for disappearing charged tracks provide a rather unique handle on the IDM high-mass regime [110]. While the IDM can lead to the same E_T^{miss} signals as the 2HDM+a model, the resulting kinematic distributions will in general not be the same, due to the different production mechanisms and decay topologies in the two models. Selection cuts that are optimised for a 2HDM+a interpretation of a given mono-X search will thus often not be ideal in the IDM context. Dedicated ATLAS and CMS analyses of the mono-X signatures in the IDM do unfortunately not exist at the moment. Such studies would, however, be highly desirable.

5.5 2HDM with an extra scalar mediator and scalar DM

Like the 2HDM+s model, the DM scenario proposed in [113] contains an extra scalar singlet, which, however, does not couple to a fermionic DM current $\bar{\chi}\chi$ but to the scalar operator χ^2. The latter work focuses on the parameter space of the model where the mediator s is dominantly produced via either $pp \to H + j \to 2s + j \to j + 4\chi$ or $pp \to H \to sh \to h + 2\chi$. The resulting mono-jet and mono-Higgs cross sections, however, turn out to be safely below the existing experimental limits. In case the mass hierarchy $M_A > M_H + M_Z$ is realised, the channel $pp \to A \to HZ$ is also interesting, since it either leads to a mono-Z or a $hZ + E_T^{\text{miss}}$ signature, depending on whether $H \to 2s \to 4\chi$ or $H \to hs \to h\chi^2$ is the leading decay. We add that an effective version of the model brought forward in [113] has already been constrained by ATLAS [114] using the mono-Higgs channel.

6 E_T^{miss} signatures and parameter variations in the 2HDM+a model

The mono-X phenomenology in the 2HDM+a model is determined by the values of the parameters introduced in (3.7). These model parameters can affect the total signal cross sections of the E_T^{miss} signatures, their kinematic distributions, or both. In this section we will discuss the basic features of the most important mono-X channels and identify the experimental observables that can be exploited to search for them. Our discussion will mainly focus on the benchmark (4.5) but we will also present results for other parameter choices to illustrate how a given parameter affects a certain E_T^{miss} signature. All results in this section are obtained at the parton level (i.e. they are fixed-order predictions that do not include the effects of a parton shower) and employ no or only minimal selection requirements. The signal samples have been generated using an UFO [115] implementation of the type-II 2HDM+a model [116] together with MadGraph5_aMC@NLO [117]. Further details on the Monte Carlo (MC) simulations can be found in Appendix C.

6.1 Resonant E_T^{miss} signatures

In the 2HDM+a model there are broadly speaking two different kinds of E_T^{miss} signatures. In the first case, the spin-0 mediator can be resonantly produced as in Figure 6 depicting relevant Feynman diagrams. Channels such as $h + E_T^{\text{miss}}$, $Z + E_T^{\text{miss}}$ and $tW + E_T^{\text{miss}}$ belong to this class. In the case of the mono-Higgs signature, it is evident from the figure that for $M_A > M_h + M_a$ the triangle graph shown on the left in the upper row allows for
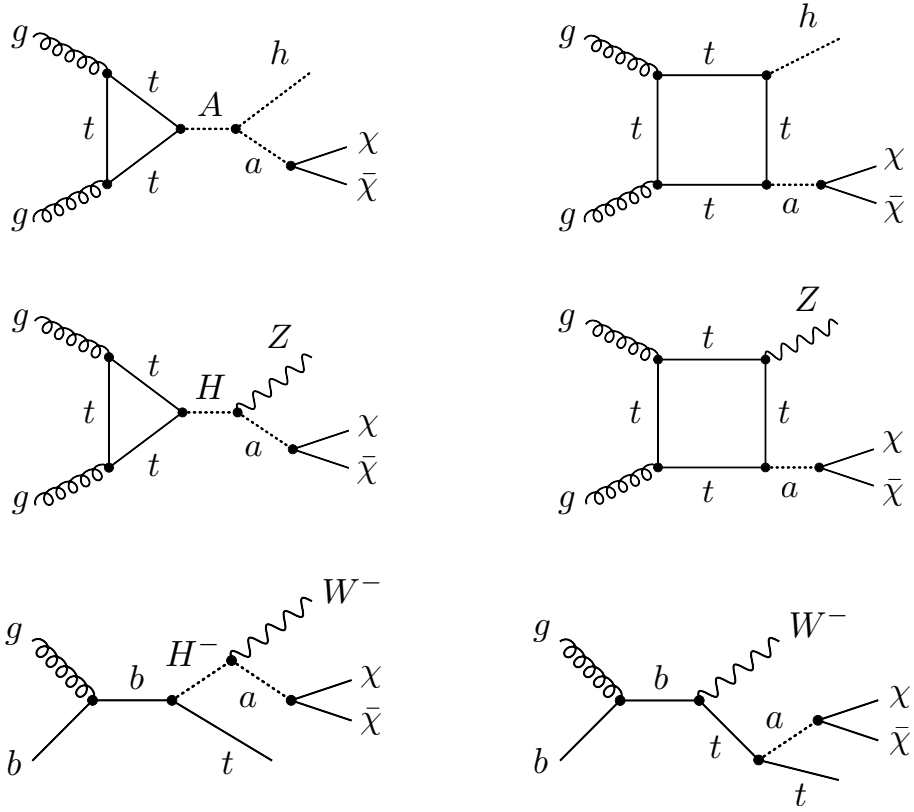
Figure 6: Example diagrams that give rise to an $h + E_T^{\text{miss}}$ (upper row), $Z + E_T^{\text{miss}}$ (middle row) and $tW + E_T^{\text{miss}}$ (lower row) signal in the 2HDM+a model. For further details consult the main text.

resonant mono-Higgs production. Similar resonance enhancements arise from the diagram on the left-hand side for the mono-Z (middle row) and $tW + E_T^{\text{miss}}$ (lower row) channel if $M_H > M_Z + M_a$ and $M_{H^\pm} > M_W + M_a$, respectively. The interference between the box diagram and the resonant production is further described in Section 6.3. Resonant $h + E_T^{\text{miss}}$, $Z + E_T^{\text{miss}}$ and $tW + E_T^{\text{miss}}$ production is not allowed in the spin-0 DM models proposed by the DMF because the mediators couple only to fermions at tree level. As a result only diagrams of the type shown on the right-hand side of Figure 6 are present in these models.

6.1.1 Mono-Higgs signature

Processes that are resonantly enhanced in the 2HDM+a model have in common that they involve the on-shell decay of a heavy Higgs $H, A, H^\pm$ to a SM particle and the mediator a, which subsequently decays to a pair of DM particles. The kinematics of the process $A \to BC$ is governed by the two-body phase space for three massive particles

$$\lambda(m_A, m_B, m_C) = (m_A^2 - m_B^2 - m_C^2)^2 - 4m_B^2 m_C^2 \,, \tag{6.1}$$
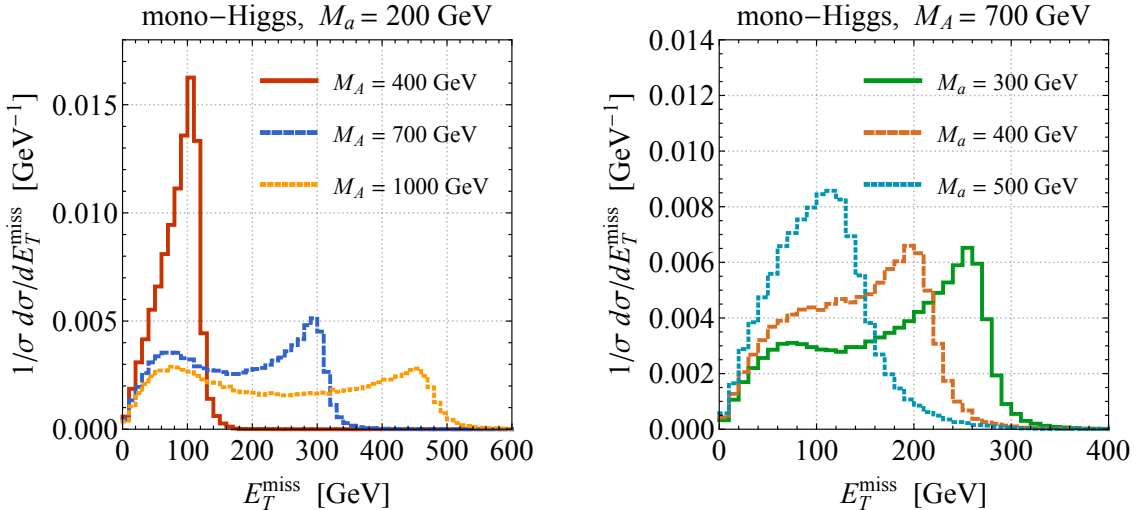
Figure 7: Normalised E_T^{miss} distributions of mono-Higgs production in the 2HDM+a model for different values of M_A and M_a as indicated in the legends. The results shown correspond to the benchmark parameter choices introduced in (4.5).

and this quantity determines the characteristic shape of resonant E_T^{miss} signals in the context of the 2HDM+a model. For instance, in the case of the mono-Higgs signal the E_T^{miss} spectrum will have a Jacobian peak with an endpoint at [21, 23]

$$E_{T,\text{max}}^{\text{miss}} \simeq \frac{\lambda^{1/2}(M_A, M_h, M_a)}{2M_A} \,, \tag{6.2}$$

for all mass configurations that satisfy $M_A > M_h + M_a$.

In Figure 7 we show the predictions for the normalised E_T^{miss} distribution of $h + E_T^{\text{miss}}$ production in the 2HDM+a model for different spin-0 boson masses M_A and M_a. Besides the indicated values of M_A and M_a the parameters used are those given in (4.5). Increasing M_A (M_a) shifts the endpoint of the Jacobian peak to higher (lower) E_T^{miss} values as expected from (6.2). A second feature that is also visible is that for large mass splittings $M_A - M_a$, the E_T^{miss} spectra develop a pronounced low-E_T^{miss} tail. The events in these tails arise dominantly from the box diagram shown on the right in the upper row of Figure 6. It can also be noted that these non-resonant contributions interfere with the resonant contributions that stem from triangle graphs. Due to the interplay of resonant and non-resonant contributions, the exact shape of the E_T^{miss} distribution is away from the endpoint (6.2) a non-trivial function of the 2HDM+a parameters (3.7).

At the LHC a mono-Higgs signal has so far been searched for in the $h \to \gamma\gamma$, $h \to b\bar{b}$ and $h \to \tau^+\tau^-$ channel (see [114, 118–121] for the latest ATLAS and CMS results). While all searches use E_T^{miss} as the main selection variable to discriminate signal from background, the $h\,(\gamma\gamma) + E_T^{\text{miss}}$ channel is sensitive to lower E_T^{miss} values than the $h\,(b\bar{b}) + E_T^{\text{miss}}$ channel, because events can be selected (triggered) based on the presence of photons, and data recording occurs at a sustainable rate at a lower E_T^{miss} threshold. The $h\,(b\bar{b}) + E_T^{\text{miss}}$ channel has instead the advantage that it is more sensitive to smaller $h + E_T^{\text{miss}}$ production
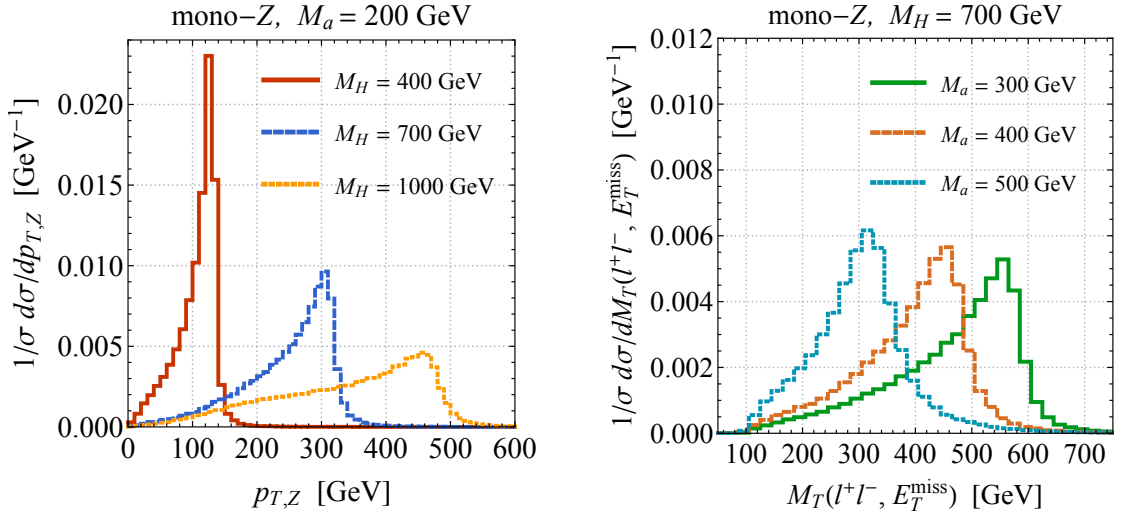
Figure 8: Normalised $p_{T,Z}$ (left panel) and $M_T(\ell^+\ell^-, E_T^{\mathrm{miss}})$ (right panel) distributions for $Z + E_T^{\mathrm{miss}}$ production followed by $Z \to \ell^+\ell^-$. The predictions shown have been obtained for the 2HDM+a benchmark parameter choices given in (4.5) and employ different values of M_H and M_a as indicated in the legends.

cross sections. These features make the two modes complementary, as models with small splittings $M_A - M_a$ are best probed in the former channel, while realisations with a larger mass hierarchy can be better probed via the $h(b\bar{b}) + E_T^{\mathrm{miss}}$ final state. We add that the CMS Collaboration has very recently provided first constraints on the 2HDM+a model using the $h(b\bar{b}) + E_T^{\mathrm{miss}}$ signal [119]. The results obtained are compatible with the ones presented in Section 8.1 of this white paper. The decay channel $h \to WW$ also offers interesting prospects to search for a mono-Higgs signal in the 2HDM+a model [122] but no results from LHC experiments have been presented so far.

6.1.2 Mono-Z signature

As for the mono-Higgs signal, an analysis of the shape of the E_T^{miss} variable in the mono-Z case offers a powerful way to enhance the signal-to-background ratio. The endpoint of the E_T^{miss} spectrum for the $Z + E_T^{\mathrm{miss}}$ signature can be obtained from (6.2) by replacing $M_A \to M_H$ and $M_h \to M_Z$. Since the four-momenta of the decay products Z and a that enter $H \to Za$ are fixed by H being preferentially on-shell, also the spectrum of the Z-boson transverse momentum $(p_{T,Z})$ in mono-Z production will have a characteristic shape if $M_H > M_Z + M_a$. In fact, the $p_{T,Z}$ distribution is predicted to be Jacobian with a cut-off at [21, 23]

$$p_{T,Z}^{\max} \simeq \frac{\lambda^{1/2}(M_H, M_Z, M_a)}{2M_H} \,, \tag{6.3}$$

that is smeared by the total decay width Γ_H of the heavy Higgs H. Ignoring higher-order QED and EW corrections and detector effects the shapes of the $p_{T,Z}$ and E_T^{miss} spectra are identical. Whether a shape fit to E_T^{miss} or $p_{T,Z}$ provides a better experimental reach thus

depends to first approximation only on which of the two variables can be better measured and the corresponding backgrounds can be controlled.

Another useful observable to study the properties of the mono-Z signal is the transverse mass

$$M_T(\ell^+\ell^-, E_T^{\mathrm{miss}}) = \sqrt{2p_{T,\ell^+\ell^-} E_T^{\mathrm{miss}} (1 - \cos\Delta\phi)}, \tag{6.4}$$

constructed from the $\ell^+\ell^-$ system and the amount of E_T^{miss}. Here $p_{T,\ell^+\ell^-}$ denotes the transverse momentum of the lepton pair and $\Delta\phi$ is the azimuthal angle between the $\ell^+\ell^-$ system and the E_T^{miss} direction.

Figure 8 displays $p_{T,Z}$ and $M_T(\ell^+\ell^-, E_T^{\mathrm{miss}})$ distributions for different choices of the masses M_H and M_a. The parameters not explicitly specified in the plots have been fixed to the values reported in (4.5). The differential distributions in $p_{T,Z}$ and $M_T(\ell^+\ell^-, E_T^{\mathrm{miss}})$ have Jacobian peaks, a feature that reflects the resonant production of a H with the subsequent decay $H \to Za \to \ell^+\ell^- \chi\bar{\chi}$. Increasing M_H (M_a) again shifts the endpoints of the distributions to higher (lower) values of $p_{T,Z}$ and $M_T(\ell^+\ell^-, E_T^{\mathrm{miss}})$. Like in the mono-Higgs case, for large mass differences $M_H - M_a$, box diagrams lead to a non-negligible mono-Z rate at low values of $p_{T,Z}$ and $M_T(\ell^+\ell^-, E_T^{\mathrm{miss}})$. Compared to the $h + E_T^{\mathrm{miss}}$ signature, the interference effects between resonant and non-resonant contributions are less pronounced in the $Z + E_T^{\mathrm{miss}}$ case.

The existing LHC searches for a mono-Z signal (cf. [123, 124] for the most recent results) have focused either on invisible decays of the SM-like Higgs boson or on topologies where the Z boson is produced in the form of ISR. Since ISR of a Z boson is suppressed by both the coupling of the Z to SM fermions and its mass compared to the radiation of a gluon [125–127], the mono-Z signal is generically not a discovery channel in models that lead to ISR-like mono-X signatures. In contrast, in the 2HDM+a model the $Z + E_T^{\mathrm{miss}}$ signature is more sensitive than the $j + E_T^{\mathrm{miss}}$ channel.

The above discussion has focused on the leptonic decay of the Z boson, but searching for a mono-Z signal in the hadronic channel is also possible. In fact, the hadronic and leptonic signatures are complementary, since hadronic decays of the Z boson are more frequent than leptonic decays, but suffer from larger backgrounds. An improved background suppression is possible if "boosted" event topologies are studied as in [128, 129], making the hadronic mono-Z signature an interesting channel if the 2HDM+a model includes high-mass Higgs states.

6.1.3 Single-top signatures

Single-top production in association with E_T^{miss} is also a promising mono-X channel in the case of spin-0 models [38, 130, 131]. The single-top production in the s-channel, t-channel or in association with a W boson can be studied. In the following, we will focus on the $tW + E_T^{\mathrm{miss}}$ channel, which in the context of the 2HDM+a model has been identified as the most interesting mode [38]. Example diagrams leading to a $tW + E_T^{\mathrm{miss}}$ signature are shown in the lower row of Figure 6. The $tW + E_T^{\mathrm{miss}}$ signal can be searched for in the single-lepton and double-lepton final state. Analysis strategies for both channels have been developed in [38]. In the former case, $M_T(\ell, E_T^{\mathrm{miss}})$ and the asymmetric transverse
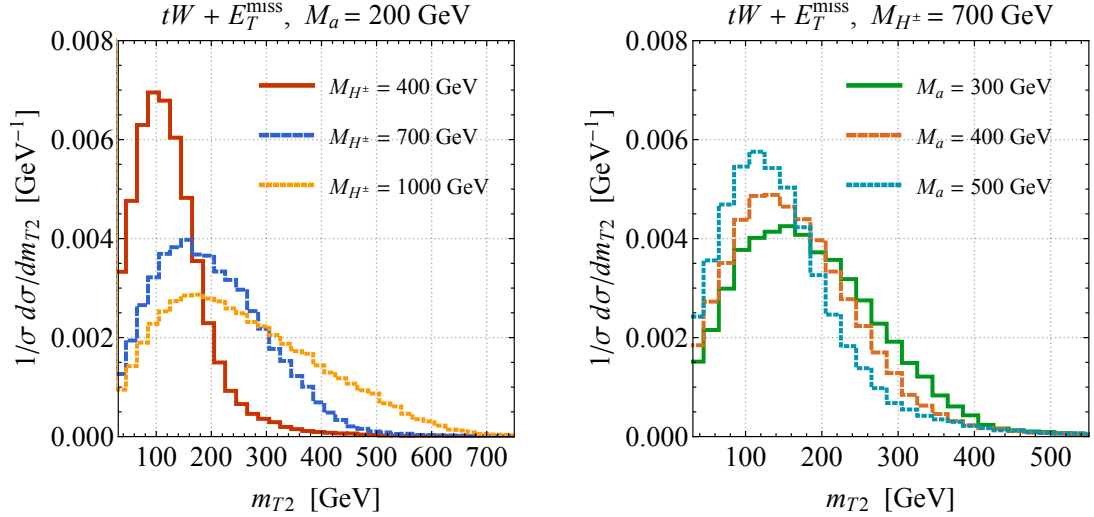
Figure 9: Normalised m_{T2} distributions for $tW + E_T^{\text{miss}}$ production in the double-lepton channel. The results shown correspond to the 2HDM+a benchmark (4.5) and employ different values of $M_{H^\pm}$ and M_a as indicated in the legends.

mass am_{T2} [132, 133] can be used to discriminate between signal and background, while in the latter case the stransverse mass m_{T2} [134, 135] plays a crucial role in the background suppression.

Examples of normalised m_{T2} distributions obtained in the 2HDM+a model are shown in Figure 9. The coloured histograms correspond to different masses $M_{H^\pm}$ and M_a. The parameters not indicated in the legends have been set to the values given in (4.5). The shape of the m_{T2} spectrum is sensitive to the values that are chosen for $M_{H^\pm}$ and M_a. In particular, the maximum of the m_{T2} distribution is shifted to higher values for larger (smaller) values of $M_{H^\pm}$ (M_a). For heavy charged Higgses the m_{T2} spectrum develops a pronounced high-m_{T2} tail. This feature can be traced back to the resonant contribution $bg \to tH^+ \to tW^+a \to tW^+\chi\bar{\chi}$ (see lower left graph in Figure 6). At present, only a single LHC analysis exists [136] that considers the $tW + E_T^{\text{miss}}$ or other single-top-like signatures with E_T^{miss}. Performing further studies of these channels would, however, be worthwhile, since enhanced single-top signatures are expected to appear in many DM model that features an extended Higgs sector.

6.2 Non-resonant E_T^{miss} signatures

Besides the resonant E_T^{miss} signatures discussed in Section 6.1, the 2HDM+a model also predicts to non-resonant mono-X signatures. The most important channels in this class are $t\bar{t} + E_T^{\text{miss}}$ and $j + E_T^{\text{miss}}$ production. In addition, the $b\bar{b} + E_T^{\text{miss}}$ mode is interesting because its rate is $\tan\beta$ enhanced if a Yukawa sector of type-II is realised. Feynman graphs leading to the first two signatures are depicted in Figure 10. For $M_A \gg M_a > 2m_\chi$ the dominant contribution to the $t\bar{t} + E_T^{\text{miss}}$ and mono-jet signals arise from diagrams involving the mediator a. In this limit the normalised kinematic distributions of the $t\bar{t} + E_T^{\text{miss}}$ and $j + E_T^{\text{miss}}$ signals in the 2HDM+a model resemble those obtained in the DMF pseudoscalar
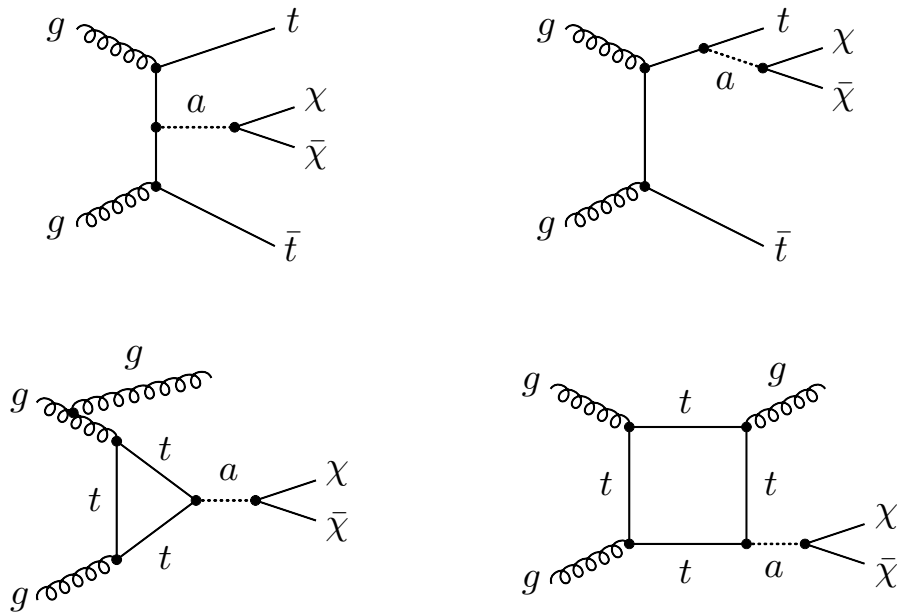
Figure 10: Prototype diagrams that lead to a $t\bar{t} + E_T^{\mathrm{miss}}$ (upper row) and $j + E_T^{\mathrm{miss}}$ (lower row) signal in the 2HDM+a model. Graphs involving a heavier pseudoscalar A also contribute to the signals but are not shown explicitly.

model. Since the contributions associated to a and A exchange interfere with each other, shape differences can, however, occur if the pseudoscalars are not widely separated in mass [23].

6.2.1 Heavy-quark signatures

Two of the main channels that have been used up to now to search for spin-0 states with large invisible decay widths at the LHC are $t\bar{t} + E_T^{\mathrm{miss}}$ and $b\bar{b} + E_T^{\mathrm{miss}}$. The latest ATLAS and CMS analyses of this type can be found in [136–138]. These searches have been interpreted in the context of the DMF spin-0 models, and for $M_A \gg M_a$ the obtained cross-section limits can be used to derive exclusion bounds in the 2HDM+a model by using [23]

$$\frac{\sigma\big(pp \to t\bar{t} + E_T^{\mathrm{miss}}\big)_{\mathrm{2HDM+a}}}{\sigma\big(pp \to t\bar{t} + E_T^{\mathrm{miss}}\big)_{\mathrm{DMF}}} \simeq \left(\frac{y_\chi \sin\theta}{g_\chi g_q \tan\beta} \right)^2 . \tag{6.5}$$

Here g_χ (g_q) denotes the DM-mediator (universal quark-mediator) coupling in the DMF pseudoscalar model. An analog formula holds in the case of the $b\bar{b} + E_T^{\mathrm{miss}}$ signature with $\tan\beta$ replaced by $\cot\beta$ in the type-II 2HDM+a model.

In Figure 11 we compare two normalised E_T^{miss} spectra obtained in the 2HDM+a model (coloured histograms) to the prediction of the DMF pseudoscalar model (black histograms). The left panel illustrates the case $M_A \gg M_a$, and one observes that the shape of the 2HDM+a distribution resembles the one of the DMF model within statistical uncertainties. As shown in the plot on the right-hand side, shape distortions instead arise
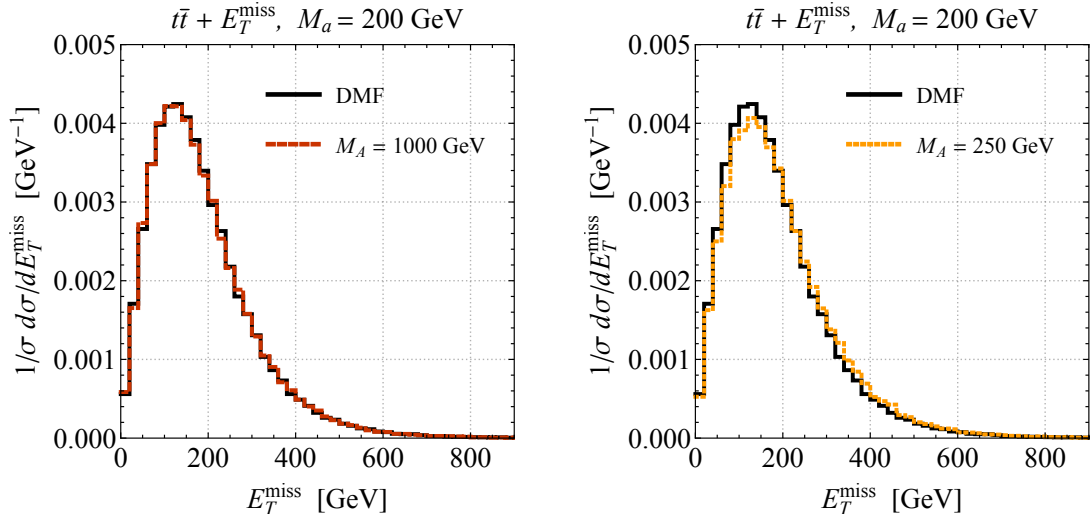
Figure 11: Normalised E_T^{miss} distributions for $t\bar{t} + E_T^{\text{miss}}$ production. The black curves correspond to the prediction of the DMF pseudoscalar model, while the coloured predictions illustrate the results in the 2HDM+a benchmark model (4.5) for two different choices of M_A and M_a.

if the particle masses M_A and M_a are not widely separated. Similar findings apply to other variables such as m_{T2} which plays a crucial role in suppressing the $t\bar{t}$ background in two-lepton analyses of the $t\bar{t} + E_T^{\text{miss}}$ signature [137, 139, 140]. It follows that in order to accurately reproduce the kinematic distributions of the signal in the entire 2HDM+a parameter space, one should not rely on (6.5) but should use a more sophisticated method. A general approach that allows to faithfully translate existing limits on DMF spin-0 models into the 2HDM+a parameter space is described in Appendix A. There it is also shown that this rescaling procedure reproduces the results of a direct MC simulation. In Appendix B we furthermore demonstrate that the same findings apply to the $t\bar{t} + E_T^{\text{miss}}$ signature in the 2HDM+s model (see Section 5.1 for a brief discussion of the model).

6.2.2 Mono-jet signature

At the LHC the most studied mono-X signal is the $j + E_T^{\text{miss}}$ channel (the newest analyses have been presented in [129, 141]) because this mode typically provides the strongest E_T^{miss} constraints on models with ISR-type signatures. Since only loop diagrams where a mediator couples to a quark (see the graphs in the lower row in Figure 10) contribute to the mono-jet signature in both the 2HDM+a and the DMF spin-0 models, the normalised kinematic distributions of the $j + E_T^{\text{miss}}$ signal turn out to be very similar in these models. In the case that the 2HDM pseudoscalar A is decoupled, i.e. $M_A \gg M_a$, one can use the right-hand side of the relation (6.5) to translate the existing mono-jet results on the DMF pseudoscalar model into the 2HDM+a parameter space, while in general one can apply the recasting procedure detailed in Appendix A.
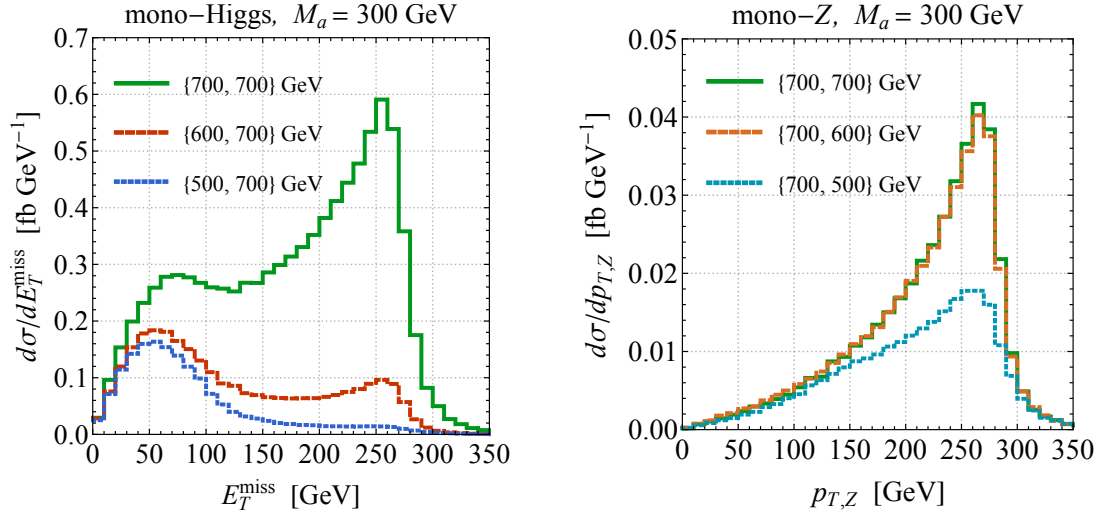
Figure 12: E_T^{miss} ($p_{T,Z}$) distributions for mono-Higgs (mono-Z) production at 13 TeV in the 2HDM+a model. The predictions shown correspond to different sets $\{M_H, M_A\}$ of masses and employ $M_{H^\pm} = \min(M_H, M_A)$, $M_a = 300\,\text{GeV}$ as well as the parameters (4.5).

6.3 Parameter variations

The kinematic distributions shown in Sections 6.1 and 6.2 all employ the parameters (4.5) and consider only variations of the common heavy spin-0 boson mass $M_H = M_A = M_{H^\pm}$ and the mediator mass M_a. In this subsection we study the impact that modifications of the parameters away from the proposed 2HDM+a benchmark scenarios have. The discussion will thereby focus on the mono-Higgs and mono-Z signatures since the rates and kinematic distributions of these two channels turn out to be most sensitive to parameter changes.

6.3.1 Variations of M_H and M_A

In Figure 12 we display E_T^{miss} distributions in $h + E_T^{\text{miss}}$ production (left panel) and $p_{T,Z}$ distributions in $Z + E_T^{\text{miss}}$ production (right panel) for different M_H and M_A values. As indicated, the coloured histograms correspond to different choices of $M_{H,A}$ and $M_{H^\pm} = \min(M_H, M_A)$, but all employ $M_a = 300\,\text{GeV}$. From the figure it is evident that the inclusive mono-Higgs (mono-Z) cross section is reduced compared to the benchmark prediction if M_H (M_A) is taken to be smaller than M_A (M_H). We furthermore observe that a change of M_H strongly affects the shape of the E_T^{miss} distribution in the mono-Higgs channel, while the distortions in the $p_{T,Z}$ distribution of the mono-Z signature under variations of M_A are much less pronounced. The strong M_H-dependence of the E_T^{miss} spectrum in $h + E_T^{\text{miss}}$ production can be traced back to the structure of the coupling g_{Aha}. From (4.4) one sees that for smaller M_H also g_{Aha} is smaller, leading to a reduced $A \to ha$ branching ratio and in turn to a lower rate of resonant production. In contrast, the coupling $g_{HZa} \propto \sin\theta$ that drives resonant production in the case of the mono-Z signal does not depend on the value of M_A.
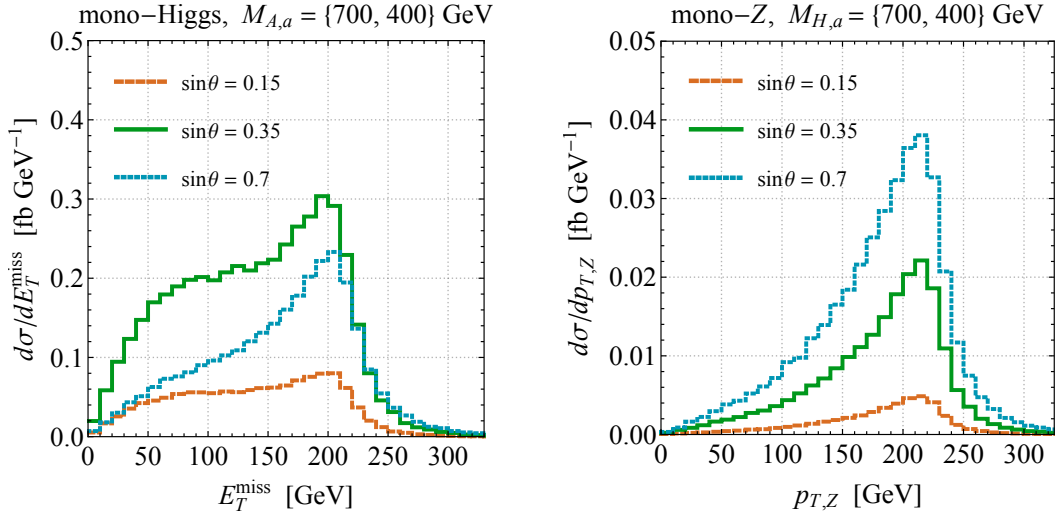
Figure 13: E_T^{miss} ($p_{T,Z}$) distributions for mono-Higgs (mono-Z) production at $13\,\text{TeV}$ in the 2HDM+a model. The displayed results correspond to different choices of $\sin\theta$. The remaining parameters are fixed to (4.5) using $M_H = M_A = M_{H^\pm} = 700\,\text{GeV}$ and $M_a = 400\,\text{GeV}$.

In order to minimise the constraints from EW precision observables (see the discussion in Section 4.3) we have chosen $M_H = M_{H^\pm}$ in the benchmark scenario (4.5). The further choice of having a common 2HDM spin-0 boson mass $M_H = M_A = M_{H^\pm}$ is then motivated by the observation that in such a case both the $h + E_T^{\text{miss}}$ and $Z + E_T^{\text{miss}}$ signature are dominated by resonant production. While in our sensitivity studies presented in the next section we will always employ the choice $M_H = M_A = M_{H^\pm}$, in future 2HDM+a interpretations of mono-X searches one might, however, also want to consider cases with $M_H \neq M_A$.

6.3.2 Variation of $\sin\theta$

Figure 13 shows E_T^{miss} distributions in $h + E_T^{\text{miss}}$ production (left panel) and $p_{T,Z}$ distributions in $Z + E_T^{\text{miss}}$ production (right panel) for different values of $\sin\theta$. The spin-0 masses are chosen as $M_H = M_A = M_{H^\pm} = 700\,\text{GeV}$ and $M_a = 400\,\text{GeV}$, and the remaining parameters are fixed to (4.5). It can be observed that the variation of $\sin\theta$ leads to both a rate and shape change in the case of the mono-Higgs signal, while in the case of the mono-Z channel only the total cross section gets rescaled to first approximation (in the peak region the shape changes of the $p_{T,Z}$ distribution amount to at most $\pm10\%$ for the considered $\sin\theta$ values). The strong sensitivity of the shape of the E_T^{miss} spectrum in $h + E_T^{\text{miss}}$ production is again a result of the interplay of resonant and non-resonant contributions. While the $gg \to A \to ha \to h\chi\bar{\chi}$ amplitude scales as $\sin\theta\cos^2\theta$, the $gg \to ha \to h\chi\bar{\chi}$ matrix element shows a $\sin\theta$ dependence. These scalings imply that at moderate (small and large) $\sin\theta$ the resonant (non-resonant) amplitudes provide the dominant contribution to the E_T^{miss} distribution in mono-Higgs production. In the case of the mono-Z signal the resonant and non-resonant amplitudes both scale as $\sin\theta$ and in consequence all kinematic distributions are essentially not distorted under changes of the mixing angle θ. The latter statement
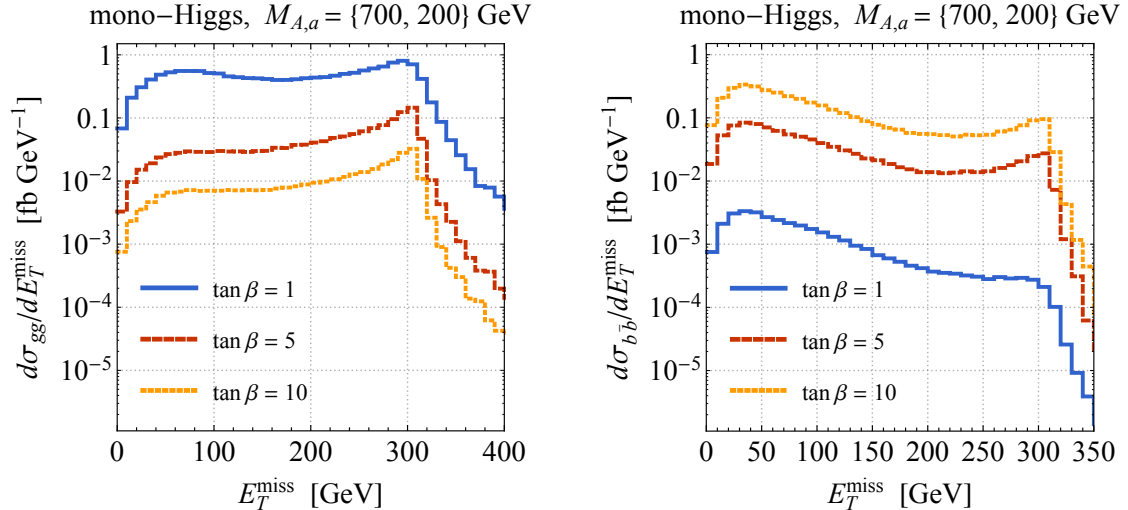
Figure 14: E_T^{miss} distributions for mono-Higgs production in gg-fusion (left panel) and $b\bar{b}$-fusion (right panel) in the 2HDM+a model. The displayed results correspond to pp collisions at $13\,\mathrm{TeV}$ and different choices of $\tan\beta$. The parameters not detailed in the plots are set to (4.5) using $M_H = M_A = M_{H^\pm} = 700\,\mathrm{GeV}$ and $M_a = 200\,\mathrm{GeV}$.

also holds in the case of the $t\bar{t} + E_T^{\mathrm{miss}}$, $b\bar{b} + E_T^{\mathrm{miss}}$ and mono-jet signatures. This can be deduced from (6.5).

From the above discussion it follows that the choice $\sin\theta = 0.35$ made in (4.5) leads to an enhanced sensitivity of the mono-Higgs signal to the 2HDM+a parameter space. To perform parameter scans in scenarios with larger mixing angles like $\sin\theta = 0.7$ would, however, also be worthwhile because such a choice would lead to an improved coverage via the mono-Z channel. We finally note that in scenarios with $\sin\theta > 0.35$ the maximal allowed size of mass splitting $|M_H - M_a|$ can, depending on the choice of λ_3, be severely constrained by vacuum stability arguments. This can be seen from (4.3).

6.3.3 Variation of $\tan\beta$

In Figure 14 we display E_T^{miss} distributions in mono-Higgs production for different choices of $\tan\beta$. The left (right) panel illustrates the contributions from the $gg \to h + E_T^{\mathrm{miss}}$ ($b\bar{b} \to h + E_T^{\mathrm{miss}}$) channel. The results shown employ (4.5) with $M_H = M_A = M_{H^\pm} = 700\,\mathrm{GeV}$ and $M_a = 200\,\mathrm{GeV}$. The total production cross section in gg-fusion strongly decreases with increasing $\tan\beta$, while in the case of $b\bar{b}$-fusion the opposite behaviour is observed. The strong reduction/enhancement of the production rates originates from the fact that in the type-II 2HDM+a model considered in this white paper the couplings of H, A, a to top quarks are proportional to $\cot\beta$, while the corresponding couplings to bottom quarks are proportional to $\tan\beta$. Numerically, we find that at the inclusive level the gg-fusion and $b\bar{b}$-fusion contributions to mono-Higgs production are comparable in size for $\tan\beta \simeq 5$. This means that for $\tan\beta \gtrsim 5$ both channels have to be included to obtain accurate predictions. From the two panels it is furthermore apparent that variations of $\tan\beta$ do not only change the overall signal strength, but also have a pronounced impact on the shapes of the E_T^{miss}
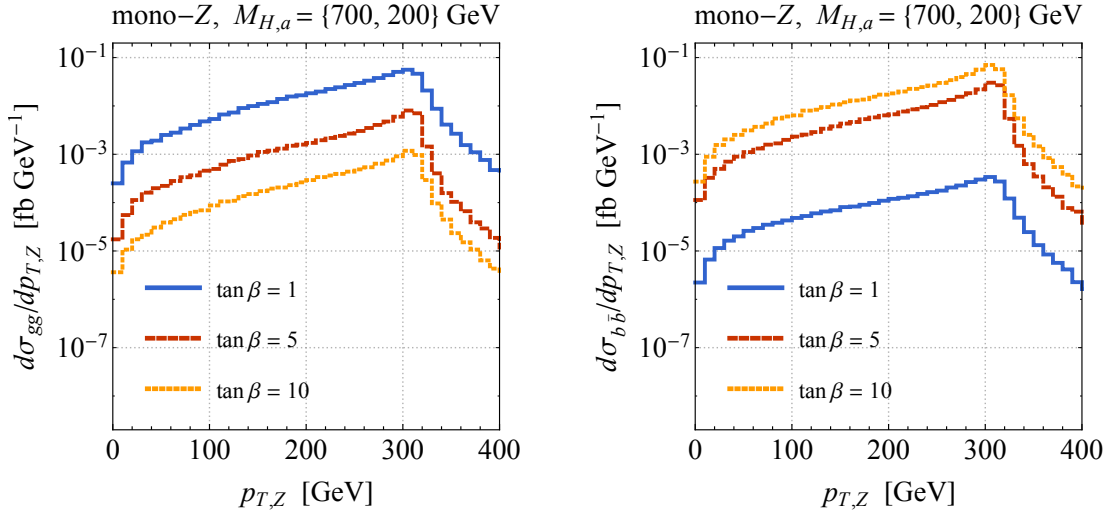
Figure 15: $p_{T,Z}$ distributions for mono-Z production in gg-fusion (left panel) and $b\bar{b}$-fusion (right panel) in the 2HDM+a model. The predictions shown correspond to pp collisions at $13\,\mathrm{TeV}$ and the same choices of parameters as in Figure 14 are employed.

distributions. In particular, changes in $\tan\beta$ influence the importance of resonant versus non-resonant contributions.

Similar to the mono-Higgs channel, $b\bar{b}$-initiated production can also be relevant for the mono-Z signal, if $\tan\beta$ is sufficiently large [23]. Figure 15 displays $p_{T,Z}$ spectra in mono-Z production for different choices of $\tan\beta$ in both the gg-fusion (left panel) and $b\bar{b}$-fusion (right panel) channel. From the plots one sees that for the considered parameters $M_H = M_A = M_{H^\pm} = 700\,\mathrm{GeV}$ and $M_a = 200\,\mathrm{GeV}$, production in $b\bar{b}$-fusion dominates over gg-fusion already for the choice $\tan\beta = 5$. In the mono-Z case the shapes of the differential distributions are less distorted under changes of $\tan\beta$ than the mono-Higgs spectra. We furthermore add that the modifications in the kinematic distributions of $t\bar{t} + E_T^{\mathrm{miss}}$ and $j + E_T^{\mathrm{miss}}$ production under changes of $\tan\beta$ are, like in the mono-Z case, not very pronounced.

Our scans in the M_a–M_H plane are based on the choice $\tan\beta = 1$, since for this value the existing mono-Higgs and mono-Z searches already provide sensitivity to/exclude large regions in the mass planes. These scans are complemented by sensitivity studies in the M_a–$\tan\beta$ (cf. Section 8 and [21, 23, 38]). We add that, if $\tan\beta$ is scanned, special attention has to be given to the fact that in the large-$\tan\beta$ limit the total decay widths of some of the Higgs states can become very large, potentially invalidating the narrow width assumption. To give an example, for the choice made in (4.6) one has $\Gamma_H/M_H \gtrsim 30\%$ for $\tan\beta \gtrsim 10$ and $M_a \lesssim 300\,\mathrm{GeV}$.

6.3.4 Variation of m_χ

The modifications of the E_T^{miss} ($p_{T,Z}$) spectrum in $h + E_T^{\mathrm{miss}}$ ($Z + E_T^{\mathrm{miss}}$) production under a variation of the DM mass m_χ are illustrated in the two panels of Figure 16. The
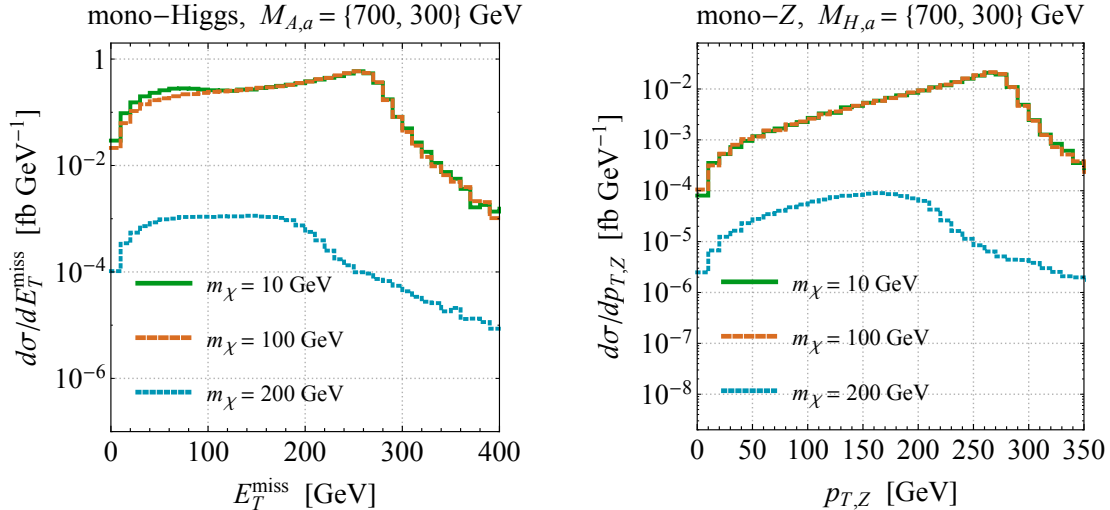
Figure 16: E_T^{miss} ($p_{T,Z}$) distributions for mono-Higgs (mono-Z) production at 13 TeV. The presented results correspond to different values of the DM mass m_χ. The other 2HDM+a parameters are set to (4.5) using $M_H = M_A = M_{H^\pm} = 700\,\text{GeV}$ and $M_a = 300\,\text{GeV}$.

given predictions correspond to pp collision at 13 TeV and employ the benchmark parameters (4.5) with $M_H = M_A = M_{H^\pm} = 700\,\text{GeV}$ and $M_a = 300\,\text{GeV}$. The depicted scenarios with $M_a > 2m_\chi$ (green and orange histograms) lead to almost identical rates, E_T^{miss} and $p_{T,Z}$ spectra, while the choice $M_a < 2m_\chi$ (blue histograms) largely reduces the total rates and also modifies the shapes of the shown distributions. This feature is expected since for $M_a > 2m_\chi$ the decay channel $a \to \chi\bar{\chi}$ is kinematically allowed, while for $M_a < 2m_\chi$ it is forbidden. In order to have detectable mono-X signals even for light mediators a, we have chosen a value of $m_\chi = 10\,\text{GeV}$ as the baseline for the following sensitivity studies. We will discuss the role that the DM mass m_χ plays in the context of DD, ID and the DM relic density in Section 9 and Section 10, respectively.

7 Non-E_T^{miss} collider signatures in the 2HDM+a model

In this section we will discuss the most important non-E_T^{miss} signals that can be used to explore the parameter space of the 2HDM+a model at the LHC. Most of the discussion will be centred around final states containing top quarks since these channels provide the best sensitivity to model realisations with low $\tan\beta$ such as our benchmark parameter choice (4.5). Final states that give access to the 2HDM+a parameter space with large $\tan\beta$ such as di-tau searches will, however, also be discussed briefly.

7.1 Di-top searches

In all 2HDM models, the spin-0 bosons H, A decay dominantly to top-quark pairs if these states have masses above the top threshold, i.e. $M_{H,A} > 2m_t$, and if $\cos(\beta - \alpha) \simeq 0$ and $\tan\beta = \mathcal{O}(1)$. New-physics scenarios of this kind can thus be tested by studying the $t\bar{t}$
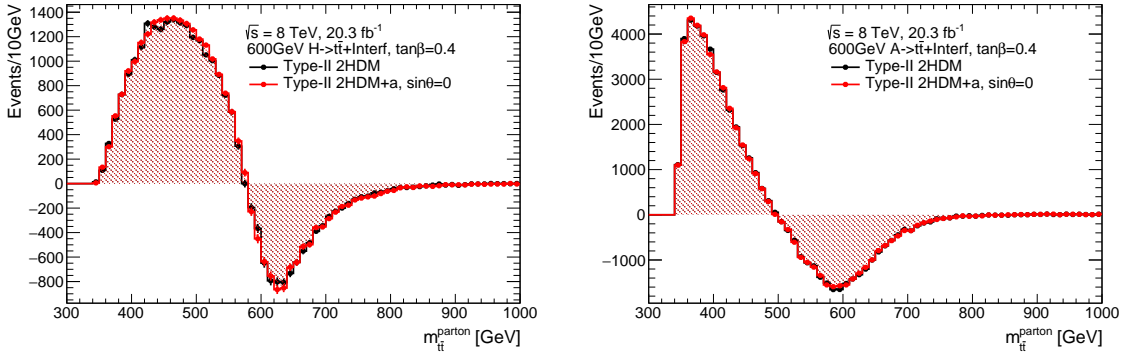
Figure 17: $m_{t\bar{t}}$ spectra for $gg \to H \to t\bar{t}$ (left) and $gg \to A \to t\bar{t}$ (right). The black (red) predictions correspond to the type-II 2HDM (2HDM+a) model. The results shown employ $M_H = M_A = M_{H^\pm} = 600\,\text{GeV}$, $M_a = 100\,\text{GeV}$, $\tan\beta = 0.4$ and $\sin\theta = 0$, and correspond to $20.3\,\text{fb}^{-1}$ of 8 TeV data. The parameters not explicitly specified are chosen as in (4.5).

invariant mass spectrum $m_{t\bar{t}}$. Interference effects between the signal process and the SM $t\bar{t}$ background, however, distort the $m_{t\bar{t}}$ signal shape from a single peak to a peak-dip structure [142–147], a feature that represents a serious obstacle to probe 2HDM models with $M_{H,A} > 350\,\text{GeV}$ and small $\tan\beta$ values [148–151].

The first LHC analysis that takes into account interference effects between the signal process $gg \to H/A \to t\bar{t}$ and the SM background $gg \to t\bar{t}$ is the ATLAS search [75]. This search is based on an integrated luminosity of $20.3\,\text{fb}^{-1}$ collected at 8 TeV. The results are interpreted in the alignment limit of the usual type-II 2HDM. The obtained exclusion limits in the $M_{H,A}$–$\tan\beta$ plane turn out to be significantly stronger than previously published LHC constraints on the 2HDM parameter space with low $\tan\beta$ and $M_{H,A} \simeq [500, 650]\,\text{GeV}$. For instance, for $M_{H,A} = 500\,\text{GeV}$ values of $\tan\beta < 1$ are excluded at 95% CL.

Di-top invariant mass spectra for various $\tan\beta$ and $\sin\theta$ scenarios and 2HDM models are shown in Figures 17 and 18. The signal process has been obtained by treating the loop contributions from top and bottom quarks as form factors [152]. In this way the interference between the signal and the tree-level SM background from $gg \to t\bar{t}$ can be calculated at leading order in QCD. In Figure 17, we show predictions for the $m_{t\bar{t}}$ spectra in $gg \to H \to t\bar{t}$ (left panel) and $gg \to A \to t\bar{t}$ (right panel). The black histograms illustrate the 2HDM predictions [75], while the red curves represent the corresponding 2HDM+a predictions for the choice $\sin\theta = 0$, which effectively decouples the mediator a from the 2HDM Higgs sector. The agreement between the black and red predictions serves as a validation of our form factor implementation in the 2HDM+a model.

As examples of the parameter dependencies of the $t\bar{t}$ predictions in the 2HDM+a model, we display in Figure 18 several $m_{t\bar{t}}$ spectra in $pp \to A \to t\bar{t}$, either fixing $\sin\theta$ and varying $\tan\beta$ (left panel) or vice versa (right panel). The spin-0 boson masses are chosen $M_H = M_A = M_{H^\pm} = 600\,\text{GeV}$ and $M_a = 100\,\text{GeV}$, which implies that only the decays $H/A \to t\bar{t}$ are kinematically possible but not $a \to t\bar{t}$. From the left panel one sees that increasing $\tan\beta$ leads to a reduction of the signal strength. Likewise, larger values of
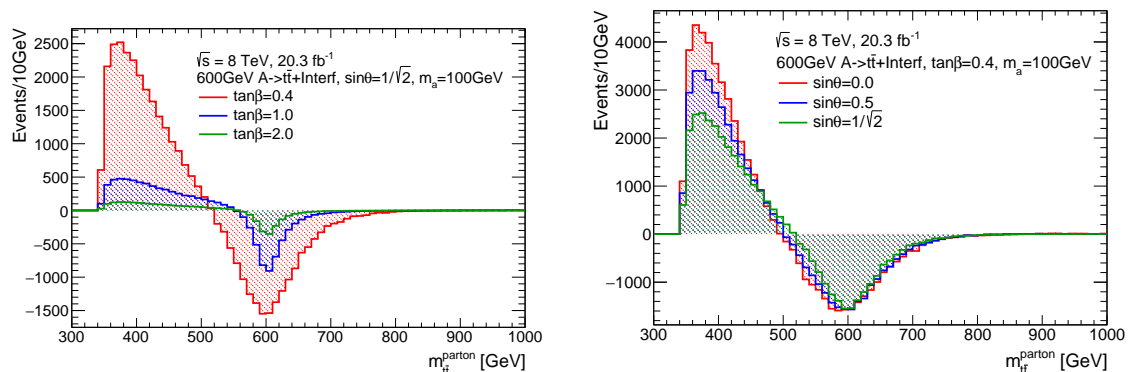
Figure 18: Left: $\tan\beta$ dependency of $m_{t\bar{t}}$ spectrum for fixed $\sin\theta = 1/\sqrt{2}$. Right: $\sin\theta$ dependency of $m_{t\bar{t}}$ spectrum for fixed $\tan\beta = 0.4$. The chosen 2HDM+a parameters are $M_H = M_A = M_{H^\pm} = 600\,\text{GeV}$ and $M_a = 100\,\text{GeV}$ and the depicted distributions correspond to $20.3\,\text{fb}^{-1}$ of integrated luminosity collected at 8 TeV. Parameters not explicitly specified are set to (4.5).

$\sin\theta$ also lead to lower $t\bar{t}$ cross sections as illustrated on the right-hand side of the latter figure. These are expected features because the $gg \to A$ amplitude scales as $\cot\beta\cos\theta$. Additionally, the interference between the $t\bar{t}$ signal and the corresponding background, and thus the shape of the $m_{t\bar{t}}$ spectrum, depends on the precise choice of $\tan\beta$ and $\sin\theta$. Before moving on, let us add that the results of [75] have already been recast to the 2HDM+a model in [23]. For the parameter benchmarks studied in the latter paper it turns out that only values $\tan\beta < \mathcal{O}(0.5)$ can be excluded based on the 8 TeV ATLAS search, making the resulting $t\bar{t}$ constraints weaker than those arising at present from flavour physics (see Section 4.2).

7.2 Four-top searches

The four-top final state is a rare, yet increasingly important signature (see for instance [76–78, 149, 150, 153]). In fact, in the work [76] the results of a search for the four-top final state based on $13.2\,\text{fb}^{-1}$ of 13 TeV LHC data has already been interpreted in the context of the standard 2HDMs. The comparison to the predictions for a type-II 2HDM in the alignment limit allows the exclusion at the 95% CL of $\tan\beta$ below 0.17 (0.11) for $M_H = 400\,\text{GeV}$ $(M_H = 1\,\text{TeV})$. While these limits are weaker than those that can be obtained from $t\bar{t}$ production in the $M_H \simeq [500, 650]\,\text{GeV}$ range [75], in the long run, four-top searches can be expected to have a better sensitivity than $t\bar{t}$ searches for mediators with masses either close to the top threshold or in the ballpark of $1\,\text{TeV}$.

In this white paper we perform a first characterisation of the four-top signature in the 2HDM+a context by studying the predicted cross section for different parameter choices. Predictions for the four-top cross section (σ_{4t}) as a function of $\tan\beta$ (left panel) and M_a (right panel) are presented in Figure 19. The total four-top production cross section in the SM ($|\text{SM}|^2$) is indicated by a black line in both panels, while the new-physics (NP)
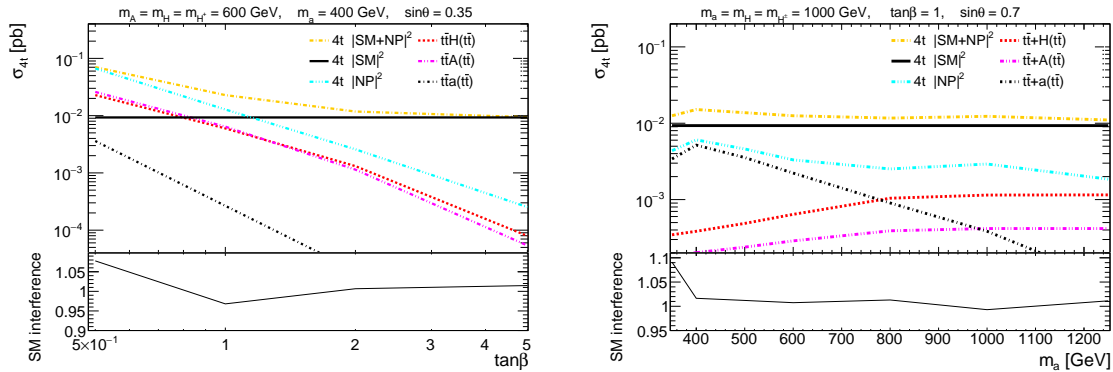
Figure 19: Four-top cross sections as function of $\tan\beta$ (left) and M_a (right) for pp collisions at 13 TeV. In the left panel $M_H = M_A = M_{H^\pm} = 600\,\text{GeV}$ and $M_a = 400\,\text{GeV}$ have been used, while in the right panel $M_H = M_A = M_{H^\pm} = 1\,\text{TeV}$ and $\sin\theta = 0.7$ have been employed. Parameters not explicitly specified are set to (4.5). The SM and the different new-physics contributions are indicated by the black and coloured lines. See text for further explanations.

contributions ($|\text{NP}|^2$) are represented by the blue curves. The predictions that account for both the SM and the 2HDM+a contribution as well as their interference ($|\text{SM} + \text{NP}|^2$) are coloured yellow. The contributions from associated $t\bar{t}$ production of an on-shell H, A, a with the subsequent decay $H/A/a \to t\bar{t}$ are also given. A brief description of how the different channels have been separated in our MC simulations is given in Appendix C. From the left panel one can see that for the chosen parameters on-shell production of H and A provides the dominant contribution to inclusive cross section. Interference effects turn out to be small as they modify the results by only $\mathcal{O}(5\%)$ at the inclusive level. This feature is illustrated in the lower part of the left plot.

On the right-hand side in Figure 19 we instead study the M_a dependence of the cross section. For the chosen parameters the $|\text{NP}|^2$ contribution is rather flat in M_a. The breakdown of the on-shell contributions furthermore shows that for $M_a \lesssim 800\,\text{GeV}$ the contribution from $t\bar{t}a$ production dominates, while for $M_a \gtrsim 800\,\text{GeV}$ the $t\bar{t}H/A$ channels are numerically more important. The small bump at $1\,\text{TeV}$ is due to interference effects between the three Higgs states. As for the previous benchmark, the impact of the signal-background interference on the inclusive cross section is found to be small (i.e. below 2%), except for M_a values close to the top threshold.

In Figure 20 we finally plot the $\sin\theta$ dependence of the new-physics contribution $|\text{NP}|^2$ to the cross section of four-top production for the two benchmarks studied before. In the case of $M_H = M_A = M_{H^\pm} = 1\,\text{TeV}$ and $M_a = 350\,\text{GeV}$ (black curve) the cross section increases for increasing $\sin\theta$. This is expected because the dominant contribution to the signal arises from $t\bar{t}a$ production followed by $a \to t\bar{t}$ and the coupling of the a to top quarks scales as $\sin\theta$. In the case of $M_H = M_A = M_{H^\pm} = 600\,\text{GeV}$ and $M_a = 200\,\text{GeV}$ (magenta curve) the cross section instead decreases with increasing $\sin\theta$. In this case the $H \to t\bar{t}$ decay gives the largest contribution, since $a \to t\bar{t}$ is kinematically closed. The observed
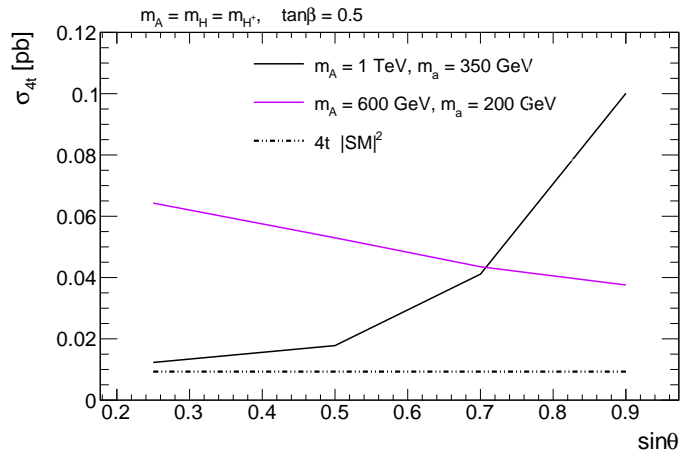
Figure 20: Four-top cross sections as a function of $\sin\theta$ at the 13 TeV LHC. The black dashed-dotted corresponds to the SM prediction, while the solid black (magenta) line employs $M_H = M_A = M_{H^\pm} = 1\,\mathrm{TeV}$ and $M_a = 350\,\mathrm{GeV}$ ($M_H = M_A = M_{H^\pm} = 600\,\mathrm{GeV}$ and $M_a = 200\,\mathrm{GeV}$). Both $|\mathrm{NP}|^2$ curves are based on $\tan\beta = 0.5$ and all parameters not explicitly specified in the legend are set to (4.5).

$\sin\theta$ dependence then arises from the interplay between $\Gamma(H \to t\bar{t})$ which does not depend on $\sin\theta$ and $\Gamma(H \to aa)$ as well as $\Gamma(H \to Za)$ which are both proportional to $\sin^2\theta$.

7.3 Other final states

The $\tau^+\tau^-$ final state is one of the most common channels that experiments have considered to search for additional neutral Higgs bosons (see [73, 74] for the latest LHC results). The sensitivity of the $\tau^+\tau^-$ searches to the 2HDM+a parameter space has been studied in [23] and found to be weak. The limited sensitivity of the $\tau^+\tau^-$ channel arises because the rates in $A/a \to \tau^+\tau^-$ are predicted to be generically small if the $A/a \to \chi\bar{\chi}$ decays are open. In fact, the decay rate $\Gamma(a \to \chi\bar{\chi})$ dominates over $\Gamma(a \to \tau^+\tau^-)$ for all parameter choices that fulfill $M_a > 2m_\chi$ and $y_\chi^2 \cot^2\beta \cot^2\theta > m_\tau^2/v^2 \simeq 5.2 \cdot 10^{-5}$ in the type-II 2HDM+a model. The latter inequality implies that it will be very difficult to test the benchmark models (4.6) through $\tau^+\tau^-$ searches. Future $\tau^+\tau^-$ analyses may however be able to exclude scenarios like (4.5) for $M_H = M_A = M_{H^\pm} = \mathcal{O}(300\,\mathrm{GeV})$ and $M_H \lesssim 2M_a$. Since such realisations are not easy to test otherwise, interpreting the results of forthcoming $\tau^+\tau^-$ searches in the 2HDM+a context seems to be worthwhile.

If $M_H > M_a + M_Z$ and the mediator a is sufficiently heavy, i.e. $M_a > 2m_t$, another channel that offers sensitivity to the 2HDM+a parameter space is $pp \to aZ$ with $a \to t\bar{t}$ instead of $a \to \chi\bar{\chi}$ [122]. The corresponding $t\bar{t}Z$ final state has been recently studied [154] in the context of the standard 2HDMs and shown to lead to a robust coverage of the 2HDM parameter space with $M_{H,A} > 350\,\mathrm{GeV}$, $|M_H - M_A| > M_Z$ and $\tan\beta = \mathcal{O}(1)$ at future LHC runs. The analysis strategy detailed in [154] can be directly applied to the 2HDM+a case, and should provide sensitivity to realisations that feature a mediators with masses above

the top threshold in the high-luminosity phase of the LHC. Such scenarios are generically difficult to explore via a mono-Z search (see Section 8.2).

The ATLAS and CMS Collaborations have set limits on the production of charged Higgses in both the $\tau\nu$ [155, 156] and the tb [157–159] final state. The limits given in [159] have been used in [38] to derive constraints on the 2HDM+a model. It turns out that the constraints on the 2HDM+a parameter space are generically weaker than those obtained in the 2HDM context, because in the 2HDM+a model the $H^{\pm} \to tb$ branching ratio tends to be reduced compared to the 2HDM since the partial decay width $H^{\pm} \to aW^{\pm}$ is generically non-vanishing. However, compared to the $tW + E_T^{\mathrm{miss}}$ signature, tb searches can still provide complementary information, because the non-E_T^{miss} search can test $M_{H^{\pm}}$ values below around $350\,\mathrm{GeV}$ which are not easily accessible with the corresponding E_T^{miss} signature [38]. Another signal that can be used to search for charged Higgses is the tbW final state [154]. This channel has, however, not yet been explored in the 2HDM+a context.

8   Sensitivity studies

In this section we present sensitivity estimates for two of the main E_T^{miss} signatures in the 2HDM+a model, namely the $h + E_T^{\mathrm{miss}}$ and the $Z + E_T^{\mathrm{miss}}$ channels. Specifically, we will consider the mono-Higgs (mono-Z) signal in the $b\bar{b}$ ($\ell^+\ell^-$) channel. Our studies are based on reinterpretation of existing results that use $36\,\mathrm{fb}^{-1}$ of LHC data taken at $\sqrt{s} = 13\,\mathrm{TeV}$. These results contain different amounts of public information. In the mono-Higgs case model-independent limits presented in [160] are used for the reinterpretation, while in the mono-Z case the sensitivity is estimated using information on the signal together with published background estimates [123]. The sensitivities that other mono-X searches provide are also briefly discussed below. A concise description of how the mono-X signals considered in our sensitivity study have been generated can be found in Appendix C.

8.1   Mono-Higgs study

The sensitivity estimates of the ATLAS and CMS mono-Higgs searches in the $b\bar{b}$ channel to the 2HDM+a model are based on the model-independent limits on the anomalous production of the SM Higgs boson in association with E_T^{miss} derived in [160]. As these limits are set in terms of the observed production cross section of non-SM events with large E_T^{miss} and a Higgs boson, they can be compared directly to the cross sections obtained in the 2HDM+a model after taking into account the kinematic acceptance $\mathcal{A}$ of the event selection and the detection efficiency ε. The variables of interest for the sensitivity study of the $h\,(b\bar{b}) + E_T^{\mathrm{miss}}$ searches are

$$S_i = \frac{\sigma_i\left(pp \to h + E_T^{\mathrm{miss}}\right)_{\mathrm{2HDM+a}} \cdot \mathrm{BR}\left(h \to b\bar{b}\right)_{\mathrm{SM}} \cdot (\mathcal{A} \cdot \varepsilon)_i}{\sigma_i\left(pp \to h + E_T^{\mathrm{miss}} \to b\bar{b} + E_T^{\mathrm{miss}}\right)_{\mathrm{obs}}}, \qquad (8.1)$$

where $\sigma_i\left(pp \to h + E_T^{\mathrm{miss}}\right)_{\mathrm{2HDM+a}}$ is the partonic cross section of the 2HDM+a signal, the branching ratio of the SM Higgs boson is denoted by $\mathrm{BR}\left(h \to b\bar{b}\right)_{\mathrm{SM}} \simeq 58\%$ and $\sigma_i\left(pp \to h + E_T^{\mathrm{miss}} \to b\bar{b} + E_T^{\mathrm{miss}}\right)_{\mathrm{obs}}$ represents the observed upper cross-section limit on $h + E_T^{\mathrm{miss}}$ production with $h \to b\bar{b}$. In our mono-Higgs sensitivity study we include gg-fusion
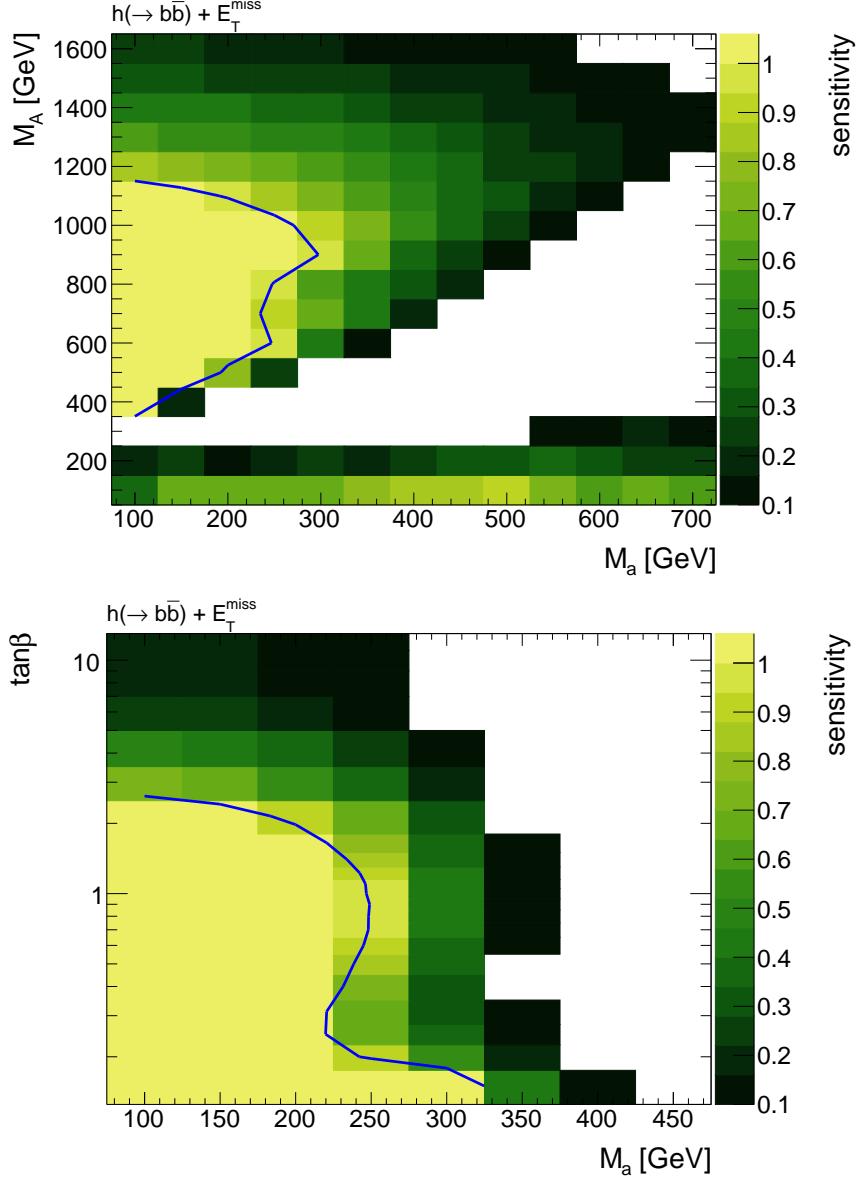
Figure 21: Estimated sensitivities with the $h + E_T^{\mathrm{miss}}$ signature in the $h \to b\bar{b}$ channel. The upper (lower) panel shows our results in the $M_a{-}M_A$ ($M_a{-}\tan\beta$) plane. The remaining parameters are set to (4.5) in the upper panel, while in the lower panel $\tan\beta$ is left to vary but the common 2HDM spin-0 boson mass is fixed to (4.6). The blue contours correspond to $S = 1$ and bins with no content have a negligible sensitivity $S < 0.1$ (see text for further explanations). The grid generated is evenly spaced in M_A and M_a, each bin corresponding to one grid point.

as well as $b\bar{b}$-initiated production. The cross sections as well as the product $\mathcal{A} \cdot \varepsilon$ depend on the considered E_T^{miss} bin as indicated by the index i. A particular point in parameter space is expected to be excluded if the sum $S = \sum_i S_i$ of the individual sensitivities is larger than 1.

The results of our sensitivity study for the mono-Higgs signal in the $b\bar{b}$ decay channel are shown in Figure 21. The upper panel in the figure displays S as a function of M_a and M_A. The existing mono-Higgs searches allow us to probe/exclude 2HDM+a scenarios with $M_A > M_h + M_a$ and sufficiently small M_a values, while they are only weakly sensitive to models where the mass hierarchy between A and a is reversed, i.e. $M_a > M_h + M_A$. Numerically, we find that for a light a with $M_a \simeq 100\,\text{GeV}$ one has $S > 1$ for all values $M_A \simeq [350, 1150]\,\text{GeV}$. In the parameter region $M_A > M_h + M_a$ the strong sensitivity of the search arises because the mono-Higgs signature is resonantly produced via $pp \to A \to ha \to h\chi\bar{\chi}$ — see the discussion in Section 6.1. The sensitivity of the search decreases for increasing (decreasing) M_A because the production rate of $pp \to A$ decreases (the Jacobian peak (6.2) is shifted to lower E_T^{miss} values). In the region $M_a > M_h + M_A$, the largest contribution to the $h + E_T^{\text{miss}}$ cross section again originates from resonant production, namely $pp \to a \to hA \to h\chi\bar{\chi}$. The resulting sensitivities are, however, much smaller compared to the case discussed before, because $\sigma(pp \to a)/\sigma(pp \to A) = \sin^2\theta/\cos^2\theta \simeq 1/7$, $\text{BR}(a \to Ah)/\text{BR}(A \to ah) < 1$ and $\text{BR}(A \to \chi\bar{\chi})/\text{BR}(a \to \chi\bar{\chi}) \ll 1$ for the parameter choices made in (4.5). Notice that in the parameter region with $M_A \gtrsim 1250\,\text{GeV}$ the BFB condition (4.3) is not satisfied (see the right panel in Figure 4) for the choice of parameters employed in the upper panel of Figure 21.

The lower panel in Figure 21 shows the sensitivity S in the M_a–$\tan\beta$ plane fixing M_H, M_A and $M_{H^\pm}$ to (4.6). The existing mono-Higgs searches allow to exclude $\tan\beta \lesssim 2.5$ for $M_a \simeq 100\,\text{GeV}$ and $\tan\beta \lesssim 1$ for $M_a \lesssim 240\,\text{GeV}$. From Figure 14 it is apparent that for such small values of $\tan\beta$, the $h + E_T^{\text{miss}}$ signal is dominantly produced through top-quark loops in gg-fusion. The corresponding production rate scales as $\sigma(gg \to A) \propto \cot^2\beta$, and as a result the sensitivity rapidly decreases for $\tan\beta > 1$. The decrease is to some extent counteracted by the fact that the Jacobian peak becomes more pronounced when $\tan\beta$ is increased (cf. the left panel in Figure 14). For $\tan\beta \gtrsim 10$ the sensitivity of the mono-Higgs search starts to increase again, because the $b\bar{b}$-initiated production cross section behaves like $\sigma(b\bar{b} \to A) \propto \tan^2\beta$. Further plots of our mono-Higgs sensitivity study can be found in Appendix D. We add that our $h(b\bar{b}) + E_T^{\text{miss}}$ results are compatible with those provided very recently by the CMS Collaboration in [119]. More restrictive experimental analyses such as [121] are expected to have an even higher sensitivity than the case studied here.

8.2 Mono-Z study

The expected sensitivity of the mono-Z search to the 2HDM+a model is estimated by comparing the number of signal events to the number of expected background events. Published background predictions for $Z + E_T^{\text{miss}}$ production followed by $Z \to \ell^+\ell^-$ [123] are used which correspond to $36\,\text{fb}^{-1}$ of $13\,\text{TeV}$ data. The selection requirements and E_T^{miss} binnings that are applied to the signal events resemble those employed in the ATLAS analysis [123]. A typical reconstruction efficiency of 75% is assumed for signal events [124], and a conservative background systematic uncertainty of 20% (10%) is taken for events with $E_T^{\text{miss}} < 120\,\text{GeV}$ ($E_T^{\text{miss}} > 120\,\text{GeV}$). Following the Asimov approximation [161], the significance $Z_{A,i}$ for individual bins i is calculated as a Poisson ratio of likelihoods modified
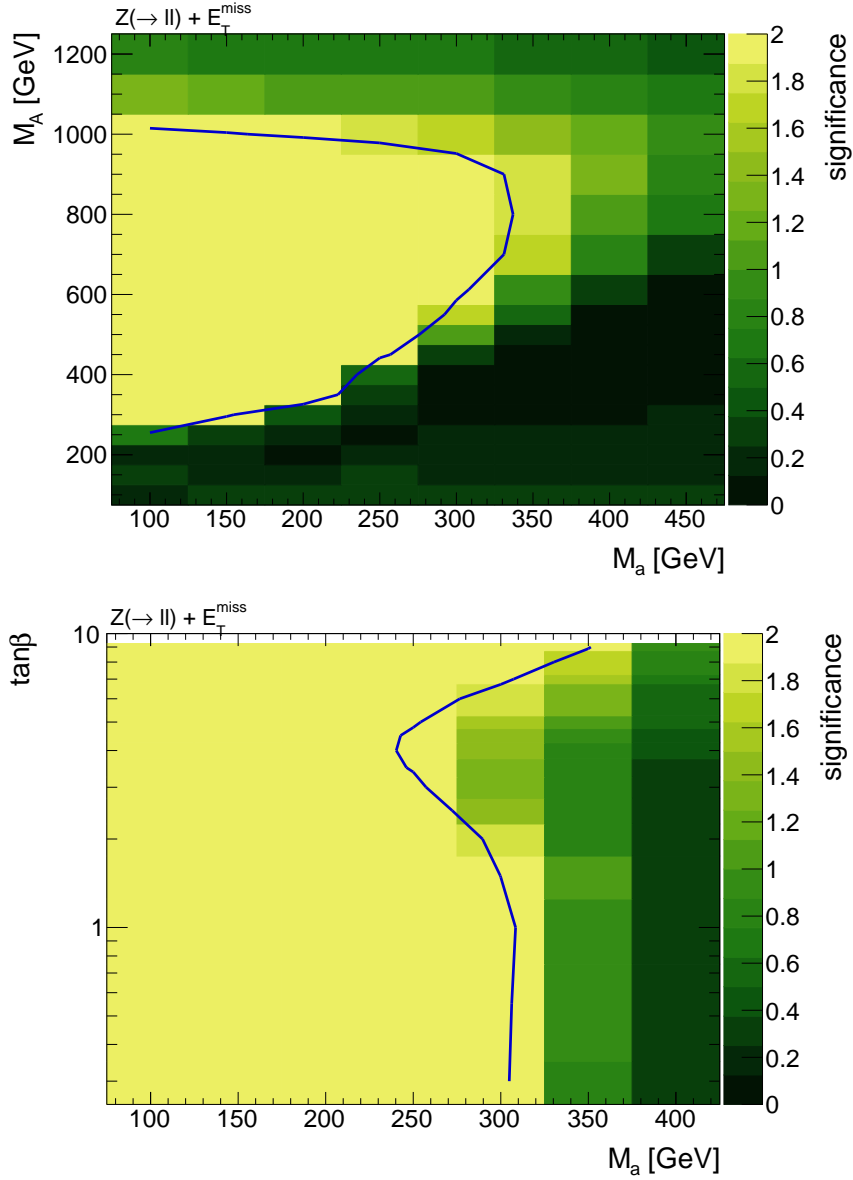
Figure 22: Estimated significance of the $Z + E_T^{\text{miss}}$ signature in the $Z \to \ell^+\ell^-$ channel. The upper (lower) panel shows our results in the M_a–M_A (M_a–$\tan\beta$) plane. The choice of parameters is identical to those made in Figure 21. The blue contours correspond to $Z_A = 2$ and the grid generated is evenly spaced in M_A and M_a, each bin corresponding to one grid point. Further details can be found in the text.

to incorporate systematic uncertainties on the background. Explicitly one has [162]

$$Z_{A,i} = \sqrt{2\left((s+b)\ln\left[\frac{(s+b)\left(b+\sigma_b^2\right)}{b^2+(s+b)\,\sigma_b^2}\right] - \frac{b^2}{\sigma_b^2}\ln\left[1+\frac{\sigma_b^2 s}{b\left(b+\sigma_b^2\right)}\right]\right)}, \qquad (8.2)$$

where $s\,(b)$ represents the expected number of signal (background) events and σ_b denotes the standard deviation that characterises the systematic uncertainties of the background. The total significance Z_A is then defined by adding the individual $Z_{A,i}$ in quadrature. In this approximation, one expects to exclude regions with total significances of $Z_A > 2$.

The results of our sensitivity study for the mono-Z signature in the $\ell^+\ell^-$ channel are presented in Figure 22. The upper (lower) panel displays the total significance Z_A in the M_a–M_A (M_a–$\tan\beta$) plane. Comparing the obtained results to those depicted in Figure 21, one observes that for the parameter choices (4.5) the mono-Z and mono-Higgs searches allow to test quite similar parameter regions in the M_a–M_A plane. Numerically, we find that for $M_a \simeq 100\,\mathrm{GeV}$ the existing $Z + E_T^{\mathrm{miss}}$ searches are sensitive to 2HDM pseudoscalar masses in the range of $M_A \simeq [250, 1000]\,\mathrm{GeV}$. The mono-$Z$ sensitivity to lower values of M_A is slightly better than the one found in the mono-Higgs case. This enhanced sensitivity arises because for fixed M_A and M_a and given that $M_Z < M_h$ the endpoint $E_{T,\mathrm{max}}^{\mathrm{miss}}$ of the E_T^{miss} distribution in $Z + E_T^{\mathrm{miss}}$ production is always higher than that in the $h + E_T^{\mathrm{miss}}$ channel. In contrast, in the parameter region with $M_a > M_Z + M_A$ the sensitivity of the mono-Z signature is weaker than that of the mono-Higgs signal. This feature is readily understood by noticing that the $pp \to a \to ZH$ channel does not lead to an E_T^{miss} signature, since the scalar H does not decay invisibly in the 2HDM+a model. For $M_a > M_Z + M_A$ hence only non-resonant diagrams contribute to the $Z + E_T^{\mathrm{miss}}$ signature, and the sensitivity to such model realisations is consequently very weak.

In the lower panel of Figure 22 we show the significance Z_A in the M_a–$\tan\beta$ plane for the choice (4.6). We see that present mono-Z searches are expected to exclude all $\tan\beta$ values for $M_a \lesssim 240\,\mathrm{GeV}$ and for $M_a \simeq 300\,\mathrm{GeV}$ the ranges $\tan\beta \lesssim 1.5$ and $\tan\beta \gtrsim 6.5$. The drop in sensitivity for $\tan\beta \simeq 4$ is a result of the interplay between gg- and $b\bar{b}$-fusion production cross sections $\sigma(gg \to H) \propto \cot^2\beta$ and $\sigma(b\bar{b} \to H) \propto \tan^2\beta$. The existing $Z\,(\ell^+\ell^-) + E_T^{\mathrm{miss}}$ searches thus have sensitivity to values $\tan\beta \gtrsim 2.5$, which is presently not the case for the $h\,(b\bar{b}) + E_T^{\mathrm{miss}}$ searches (cf. Figure 21). Both features can be understood from the discussion presented in Section 6.3.3.

8.3   Sensitivity of other mono-X channels

The sensitivities of the LHC to the associated production of DM with a single top have been studied in the framework of the 2HDM+a model in [38]. This analysis assumes $300\,\mathrm{fb}^{-1}$ of data and finds that the $tX + E_T^{\mathrm{miss}}$ signatures complement the parameter space coverage of the mono-Higgs and mono-Z signals considered by us in detail. In fact, repeating the analysis of [38] using only $36\,\mathrm{fb}^{-1}$ of integrated luminosity, one finds that a combination of the single-lepton and double-lepton channel allows to exclude values of $M_H = M_A = M_{H^\pm}$ in the range of around $[400, 1000]\,\mathrm{GeV}$ for $M_a = 150\,\mathrm{GeV}$, $\tan\beta < 1$ and $\sin\theta = 1/\sqrt{2}$. For $M_H = M_A = M_{H^\pm} = 700\,\mathrm{GeV}$ even a bound of $\tan\beta < 2$ can be set at 95% CL. While a direct comparison with the limits obtained in the mono-Higgs and mono-Z case is not possible due to the different value of $\sin\theta$ used in Sections 8.1 and 8.2, we note that the $\tan\beta$ values probed by all three searches lie in the same ballpark. Another feature that is worth recalling is that the $h + E_T^{\mathrm{miss}}$, $Z + E_T^{\mathrm{miss}}$ and $tW + E_T^{\mathrm{miss}}$ signature can be resonantly enhanced through A, H and $H^\pm$ exchange in the 2HDM+a model (see Figure 6).
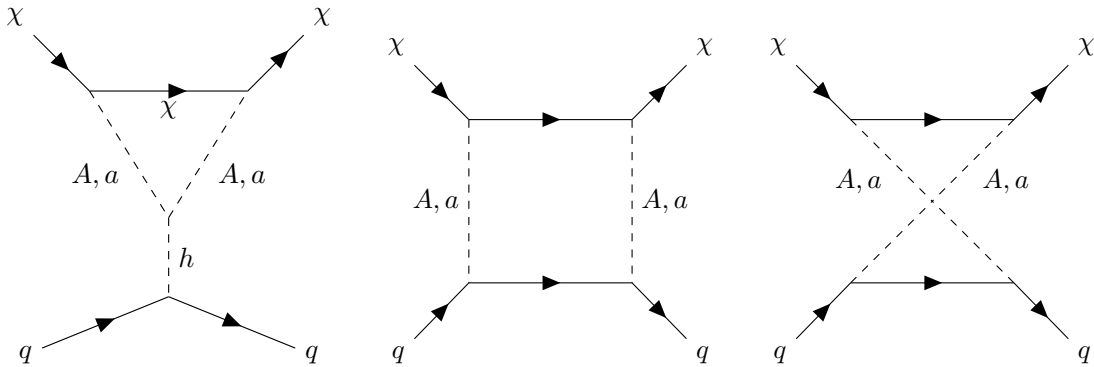
Figure 23: One-loop diagrams that lead to a SI DM-nucleon scattering cross section in the 2HDM+a model. Both triangle diagrams (left) as well as box graphs (middle and right) contribute in general. For further details consult the text.

Observing correlated deviations in all three channels might hence allow to determine the complete non-SM Higgs spectrum.

Sensitivity studies of the $t\bar{t} + E_T^{\mathrm{miss}}$ and $j + E_T^{\mathrm{miss}}$ channels in the 2HDM+a have been performed in [23]. The results presented in that work imply that for the benchmark parameter choices (4.5), the latest $t\bar{t} + E_T^{\mathrm{miss}}$ and mono-jet searches that are based on $36\,\mathrm{fb}^{-1}$ of 13 TeV data have only a very weak sensitivity to the parameter space shown in Figures 21 and 22. Given the limited sensitivity of the $t\bar{t} + E_T^{\mathrm{miss}}$ and $j + E_T^{\mathrm{miss}}$ modes, we leave detailed sensitivity studies for these channels for future work. The $b\bar{b} + E_T^{\mathrm{miss}}$ channel is also not considered here due to the same reason. Notice, however, that a reinterpretation of existing $t\bar{t} + E_T^{\mathrm{miss}}$, $b\bar{b} + E_T^{\mathrm{miss}}$ and $j + E_T^{\mathrm{miss}}$ results is straightforward by using the general rescaling strategy discussed in Appendix A.

9 Constraints from other DM experiments

In this section we discuss the constraints that DD and ID experiments set on the parameter space of the 2HDM+a model. We will illustrate both the existing constraints as well as show future projections.

9.1 DD experiments

The constraints from DD for pseudoscalar mediators are generally suppressed at tree level, so that the dominant contributions arise from one-loop Feynman diagrams [20, 163–165]. In the case of the 2HDM+a model a spin-independent (SI) DM-nucleon scattering cross section is generated by the graphs shown in Figure 23. Notice that the triangle diagram shown on the left-hand side is proportional to a single power of the Yukawa coupling y_q, while the box diagrams that are displayed in the middle and on the right of the figure are proportional to y_q^3. It follows that the triangle graph generically provides the dominant contribution to the SI DM-nucleon scattering cross section. The only exceptions are models that feature a Yukawa sector with $\tan\beta$-enhanced down-type Yukawa couplings such as
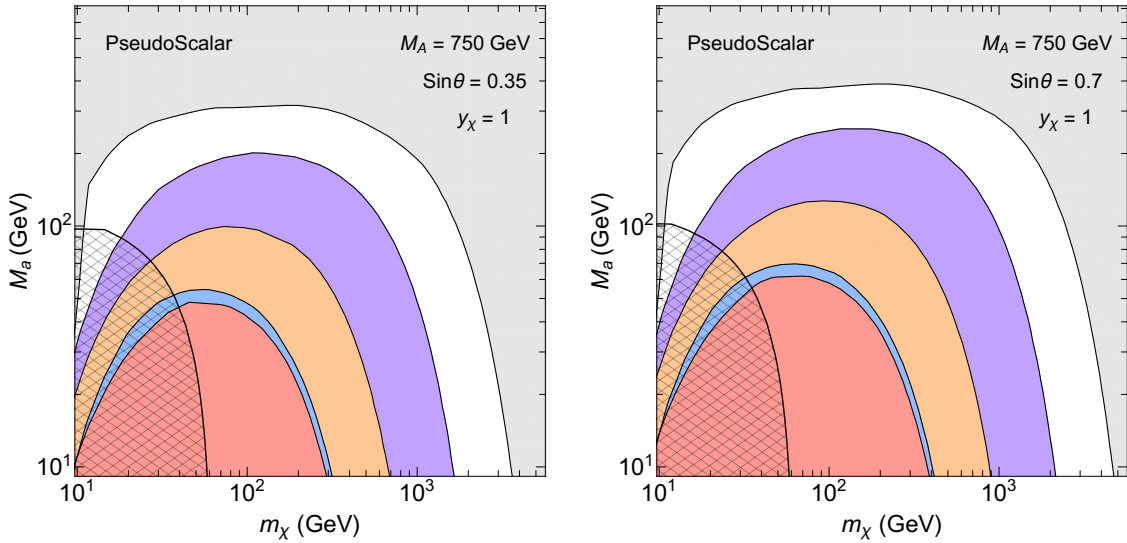
Figure 24: DD exclusions in the 2HDM+a model as function of m_χ and M_a. The constraints from LUX 2016 (red) [166], XENON1T 2017 (blue) [167] and the projections from XENON1T 2ty (orange) and XENONnT 20ty (purple) [168] are shown. The grey shaded area is not accessible to ordinary DD experiments due to the presence of the neutrino background [169], while the black hatched regions are excluded by the LHC bounds on invisible Higgs decays. In the left (right) panel the parameters $\sin\theta = 0.35$ ($\sin\theta = 0.7$), $M_A = 750\,\mathrm{GeV}$ and $y_\chi = 1$ are employed.

type-II models, where the box diagrams can be numerically important if $\tan\beta \gtrsim 50$. This has first been pointed out in [20]. Unlike the box graphs the triangle diagram does not depend on the Yukawa sector of the 2HDM+a model [163, 164].

The bounds that DD experiments can or may set on the 2HDM+a model are presented in Figure 24. In the left (right) panel the choices $\sin\theta = 0.35$ ($\sin\theta = 0.7$), $M_A = 750\,\mathrm{GeV}$ and $y_\chi = 1$ are employed. For $\sin\theta = 0.35$, current limits from LUX 2016 (red) [166] and XENON1T 2017 (blue) [167] are able to exclude the portion of parameter space with $m_\chi \simeq [10, 300]\,\mathrm{GeV}$ and $M_a \lesssim 50\,\mathrm{GeV}$. Projected limits from XENON1T 2ty (orange) and XENONnT 20ty (purple) [168] are expected to expand the exclusions to $m_\chi \lesssim 1700\,\mathrm{GeV}$ and $M_a \lesssim 200\,\mathrm{GeV}$. In the case $\sin\theta = 0.7$, the obtained limits are slightly better because of the larger mixing angle. The XENON1T 1ty constraints [170] are not explicitly shown in Figure 24. They would fall between the XENON1T 2017 and the XENON1T 2ty exclusions. For comparison also the regions in the m_χ–M_a plane excluded by the present LHC bounds on invisible Higgs decays — see Section 4.4 and [23] — are shown as black hatched regions. The results displayed in Figure 24 imply that present and future DD experiments cannot probe benchmarks like (4.5) since these employ $m_\chi = 10\,\mathrm{GeV}$. In fact, the sensitivity of DD is complementary to that of the mono-X searches beca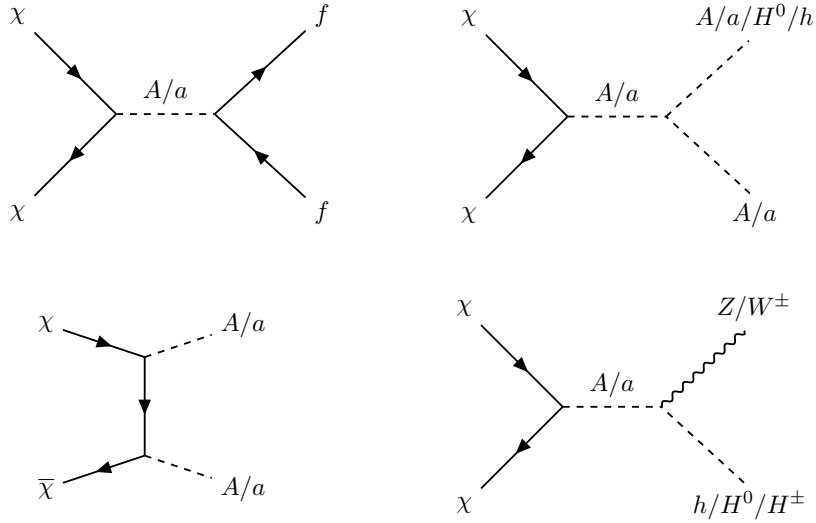use the former constraints are strongest for $M_a < 2m_\chi$ while the latter searches provide the best exclusions for $M_a > 2m_\chi$.

Figure 25: Tree-level annihilation diagrams of DM in the 2HDM+a model. Annihilation into pairs of SM fermions (f), spin-0 states (h, H, A, a) and a spin-0 particle and a EW gauge boson (HZ and $H^\pm W^\pm$) are possible in the alignment limit.

The loop calculations of $\sigma_{\rm SI}$ performed in [20, 163–165] have been recently revisited and improved in [171]. In fact, the latter article has presented the first complete leading order calculation of the SI DM-nucleon scattering cross section in the 2HDM+a context. It includes the full set of two-loop diagrams that induce an effective interaction between DM and gluons and takes into account all terms in (3.5). In contrast, in the works [20, 163–165] as well as in this white paper, two-loop effects have merely been included in an approximate fashion and only the term $P(ib_P H_1^\dagger H_2 + \text{h.c.})$ has been considered. Depending on the specific choice of parameters, the additional contributions calculated in [171] can lead to both an enhancement and a reduction of the SI DM-nucleon scattering cross section in the 2HDM+a model. For parameters where $\sigma_{\rm SI}$ is enhanced, the predicted SI DM-nucleon scattering cross sections, however, still turn out to be smaller than the current upper bounds from DD experiments, if y_χ is fixed so as for the thermal relic abundance to coincide with the observed value of Ωh^2. The main conclusion drawn before that DD experiments have only a limited sensitivity to benchmarks like (4.5) thus remains valid.

9.2 ID experiments

Due to the large number of couplings that the A, a have with SM or 2HDM states, the ID signals in the 2HDM+a model are complex. In fact, for $\cos(\beta - \alpha) = 0$, the possible annihiliation channels of DM are $f\bar{f}$, hA, HA, HZ, $H^\pm W^\mp$, ha, Ha, AA, aa and Aa. Here f denotes all SM fermions that are kinematically accessible for a given DM mass, i.e. those fermions with $m_f < m_\chi$. Relevant diagrams are shown in Figure 25. Since the SM gauge bosons and the Higgs states decay further into pairs of SM fermions, the final states resulting from the $\chi\bar{\chi}$ annihilation can contain either two or four SM particles.
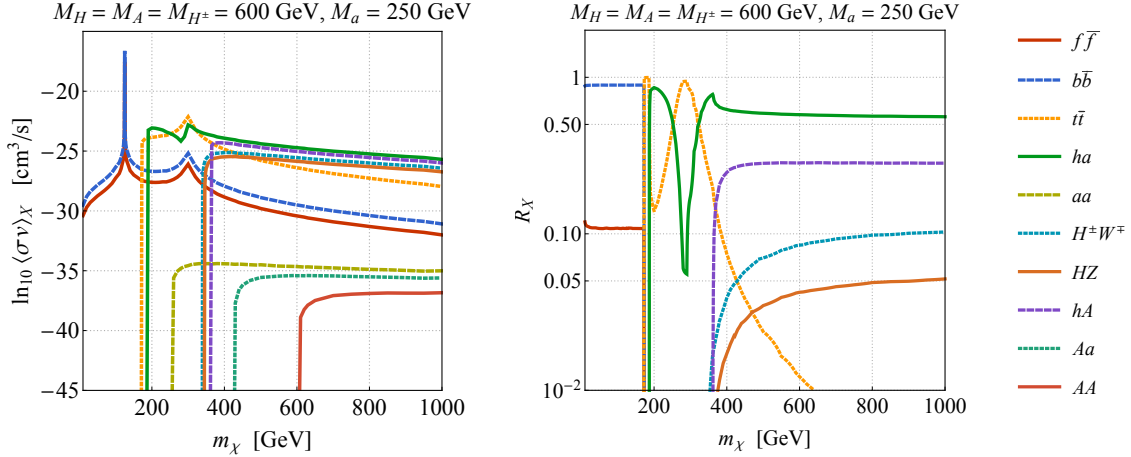
Figure 26: The velocity-averaged DM annihilation cross sections (left panel) and the corresponding relative rates (right panel) in the 2HDM+a model. The shown results correspond to $M_H = M_A = M_{H^\pm} = 600\,\text{GeV}$, $M_a = 250\,\text{GeV}$ and the benchmark choices made in (4.5). See text for further details.

In Figure 26 we display an example of the various velocity-averaged DM annihilation cross sections (left) and the corresponding relative rates $R_X = \langle \sigma v \rangle_X / \sum_Y \langle \sigma v \rangle_Y$ (right) predicted in the 2HDM+a model. Here $Y = f\bar{f}$, $b\bar{b}$, $t\bar{t}$, hA, HA, HZ, $H^\pm W^\mp$, ha, Ha, AA, aa, Aa. The employed input parameters are given by $M_H = M_A = M_{H^\pm} = 600\,\text{GeV}$, $M_a = 250\,\text{GeV}$ and (4.5). The numerical results for $\langle \sigma v \rangle$ have been obtained with `MadGraph5_aMC@NLO` using the latest `MadDM` [172] plugin. The average velocity of DM is taken to be $2 \cdot 10^{-5}\,c$, which is a typical velocity for Milky Way dwarf spheroidal satellite galaxies (see e.g. [173, 174]). Focusing on the region of DM masses below the top threshold, one sees that in this case only the annihilation cross sections for $\chi\bar{\chi} \to f\bar{f}$ with $f = e, \mu, \tau, u, d, s, c$ and $\chi\bar{\chi} \to b\bar{b}$ are non-zero. Notice that both cross sections are resonantly enhanced at $m_\chi \simeq M_a/2$ due to $\chi\bar{\chi} \to a \to f\bar{f}$, leading to narrow peaks in the spectra. For $m_\chi > m_t$ the process $\chi\bar{\chi} \to t\bar{t}$ is also possible, representing the dominant fermionic annihilation channel for DM masses above the top threshold. One furthermore notices that all fermionic channels are enhanced for $m_\chi \simeq M_A/2$. This is again a resonance effect driven by $\chi\bar{\chi} \to A \to f\bar{f}$ with an on-shell A. The remaining annihilation processes $\chi\bar{\chi} \to AB$ with A, B either two spin-0 bosons or a spin-0 and a EW gauge boson turn on whenever the relevant threshold is reached, i.e. $m_\chi > (m_A + m_B)/2$. The largest channel of this type is $\chi\bar{\chi} \to ha$ which for the chosen parameters dominantly leads to a $b\bar{b}b\bar{b}$ final state. Also DM annihilation to $H^\pm W^\mp$, HZ and hA is relevant for $m_\chi \gtrsim (M_h + M_A)/2$, while the remaining channels involving two pseudoscalars, i.e. aa, Aa and AA, are all numerically negligible. We also add that the annihilation cross section corresponding to $\chi\bar{\chi} \to HA$ is exactly zero due to our parameter choices $\tan\beta = 1$ and $\lambda_{P1} = \lambda_{P2}$.

Figure 26 also shows that the total DM annihilation cross section is lowest for light DM and in this mass region fully dominated by the annihilation into the $b\bar{b}$ final state. For

our benchmark choice $m_\chi = 10\,\text{GeV}$, we obtain for instance a velocity-averaged $\chi\bar\chi \to b\bar b$ annihilation cross section of $\langle\sigma v\rangle_{b\bar b} = 3.0 \cdot 10^{-30}\,\text{cm}^3/\text{s}$. The corresponding Fermi-LAT bound is compared to this weaker by more than three orders of magnitude as it amounts to $4.8 \cdot 10^{-27}\,\text{cm}^3/\text{s}$ [175]. In fact, for the parameters chosen to obtain the results depicted in the latter figure, we find that DM masses in the range of $m_\chi \simeq [110, 115]\,\text{GeV}$ and $m_\chi \simeq [190, 405]\,\text{GeV}$ are excluded at 95% CL by the Fermi-LAT constraints on $\chi\bar\chi \to b\bar b$ and $\chi\bar\chi \to t\bar t$, respectively. Notice that for $m_\chi > (m_h + m_a)/2$ also the $\chi\bar\chi \to AB \to 4f$ channels may lead to constraints when confronted with the Fermi-LAT data. These additional annihilation contributions have however not been considered when quoting the excluded m_χ ranges (a full treatment of ID bounds would require to calculate the sum of the photon energy (E_γ) spectra from all contributing channels and to construct a joint likelihood across all E_γ bins of the photon flux to determine if a specific point in parameter space is ruled out; cf. [176, 177] for instance). The different dependence on m_χ makes ID experiments and LHC mono-X searches complementary in constraining the 2HDM+a parameter space.

10   DM relic density

In this section, we check the consistency of the 2HDM+a model as a function of the parameters chosen for the scans with the measured DM relic density, according to the standard thermal relic "freeze-out" scenario. This exercise requires the following assumptions, already detailed in [12]. First, the DM annihilation cross section receives only contributions from the interactions of the 2HDM+a model, while possible additional degrees of freedom and couplings not included in the model are ignored. Second, the DM number density in the Universe today is entirely determined by the DM annihilation cross section predicted by the 2HDM+a model. In particular, no additional mechanisms exist that enhance or deplete the DM relic density. It is important to realise that if one or both of these assumptions are violated there is no strict correlation between the relic density and the strength of mono-X signals. For instance, if DM is overproduced, the relic density can be reduced if the DM has large annihilation cross sections to new hidden sector states. These states might however not be directly accessible at LHC energies. Conversely, the correct DM relic density can still be obtained if the DM is underproduced. For instance, if the hidden sector carries a particle-antiparticle asymmetry (similar to the baryon asymmetry) then this necessarily leads to a larger relic density compared to the conventional freeze-out picture.

10.1   Calculation

The Feynman diagrams of the annihilation processes taken into account in the calculation of the DM relic density in the 2HDM+a model are shown in Figure 25. Generally, the annihilation proceeds via single (upper and lower right graphs) or double exchange (lower left graph) of the pseudoscalars A and a with subsequent decays. The MadDM [178, 179] plugin for MadGraph5_aMC@NLO is used to calculate the present-day DM relic density. Since MadDM uses only $2 \to 2$ scattering diagrams, contributions from off-shell pseudoscalars can only be taken into account for the case of single mediation with direct decay of the pseudoscalars to SM fermions. If the pseudoscalars instead decay to other bosons or if the
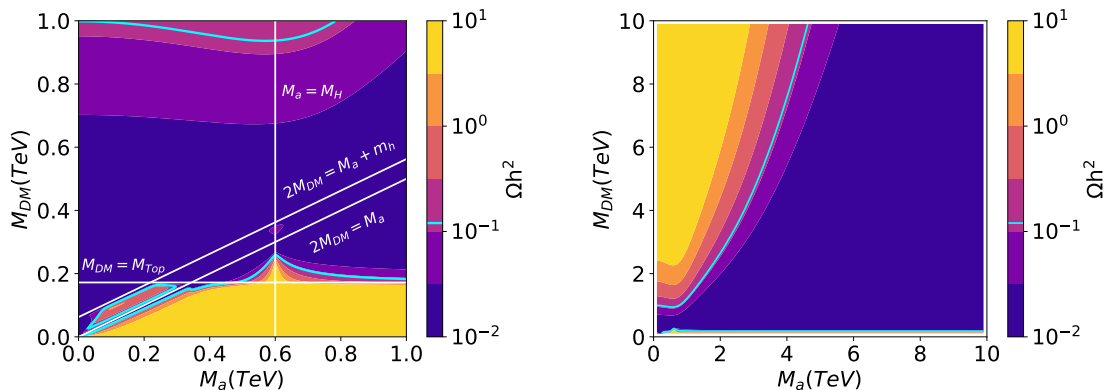
Figure 27: Predicted DM relic density for a two-dimensional scan of M_a and m_χ. The other parameters remain fixed at $M_H = M_A = M_{H^\pm} = 600\,\text{GeV}$ and $\tan\beta = 1$, as well as the benchmark choices given in (4.5). The color scale indicates the DM relic density, the cyan solid line shows the observed value of $\Omega h^2 = 0.12$. The color scale is truncated at its ends, i.e. values larger than the maximum or smaller than the minimum are shown in the same color as the maximum/minimum. While the left panel focuses on the mass region relevant to collider searches, the right panel shows the development of the DM relic density for a larger mass region.

annihilation proceeds through double-exchange diagrams, the outgoing bosons are taken to be on-shell and their decays are not simulated. All tree-level annihilation processes are considered, and the Yukawa couplings of all fermions are taken to be non-zero.

10.2 Scan results

If not stated otherwise, the results shown in this section use the benchmark values from (4.5). The DM relic density is displayed in the M_a–m_χ plane in the two panels of Figure 27. The parameters not indicated in the plots are fixed to $M_H = M_A = M_{H^\pm} = 600\,\text{GeV}$ and $\tan\beta = 1$. For values of m_χ below the mass of the top quark, DM is mostly overabundant. In this regime, annihilation to quarks is suppressed by the small Yukawa couplings of the light fermions. The observed DM relic density can only be achieved for $m_\chi \simeq M_a/2$, where annihilation is resonantly enhanced, or for $m_\chi \simeq (M_a + M_h)/2$, close to the threshold for the $\chi\chi \to ha$ process. Above the top threshold, annihilation into fermions becomes very efficient and DM is typically underabundant. Exceptions are regions in parameter space where $M_a \gtrsim m_t$ and $m_\chi \simeq m_t$ in which the observed DM relic density can be achieved. As m_χ increases further, annihilation via single-exchange diagrams is more and more suppressed and the observed DM relic density can again be reproduced. At low values of M_a this happens for $m_\chi \simeq 1\,\text{TeV}$. The right panel of Figure 27 shows in addition the two branches of solutions for masses up to $10\,\text{TeV}$.

The dependence of the DM relic density on the choice of m_χ is further explored in Figure 28 (left). The red curve represents the choices $M_H = M_A = M_{H^\pm} = 600\,\text{GeV}$, $M_a = 250\,\text{GeV}$ and $\tan\beta = 1$. The result shown confirms the presence of the previ-
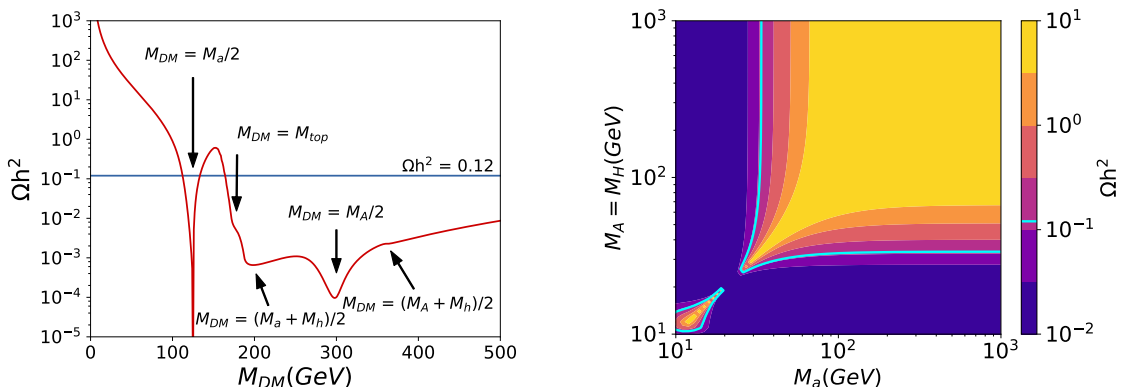
Figure 28: Left: DM relic density in the 2HDM+a model as a function of m_χ. The predictions shown are obtained for $M_H = M_A = M_{H^\pm} = 600\,\text{GeV}$, $M_a = 250\,\text{GeV}$ and $\tan\beta = 1$. See text for further details. Right: Predicted DM relic density for the 2HDM+a model in the M_a–M_A plane. A common mass $M_H = M_A = M_{H^\pm}$ is used. The colour coding resembles that of Figure 27.

ously discussed regions of resonant enhancement and kinematic boundaries. Overall, the behaviour is dominated by the low-m_χ suppression of the annihilation cross section, the resonant enhancement at $m_\chi = M_a/2$ and the top thresholds. Other effects, such as the resonant enhancement of $\chi\chi \to A$ annihilation are present, but are small.

The DM relic density values for the M_a–M_A scan are shown in the right panel of Figure 28. The regions where the 2HDM+a model predicts a DM relic density compatible with the measured value $\Omega h^2 = 0.12$ are located either at $M_a < 30\,\text{GeV}$ or at $M_A = M_H = M_{H^\pm} < 30\,\text{GeV}$. As explained in Section 4.4 the first option is excluded by the LHC bounds on invisible Higgs decays, while the second possibility is ruled out directly by LEP and LHC searches for charged Higgses and indirectly by flavour physics. This means that the benchmark (4.5) employed in this white paper cannot give rise to the correct DM relic density as it generically predicts $\Omega h^2 \gg 0.12$. Since the cosmological production of DM is largely driven by the choice of m_χ it is however possible to tune the DM mass such that the correct DM relic density is obtained in scenarios (4.5) with $m_\chi \neq 10\,\text{GeV}$. For instance, by choosing the DM mass to be slightly below the a threshold, i.e. $m_\chi = M_a/2$, one can obtain $\Omega h^2 \lesssim 0.12$ (see the left panel in Figure 28). Given that both the total cross sections and the kinematic distributions of the mono-X signatures are largely insensitive to the precise choice of m_χ as long as $m_\chi < M_a/2$ (cf. Figure 16), our sensitivity studies performed in Section 8 apply to first approximation also to scenarios like (4.5) where the measured DM relic density is obtained by tuning $m_\chi \simeq M_a/2$. From the collider perspective another interesting parameter region is $M_a \gtrsim 2m_t$ and $m_\chi \simeq m_t$ since it can be probed by LHC searches and can lead to the observed DM relic density (see the left-hand side of Figure 27).

In Figure 29 we display $\tan\beta$ scans as a function of M_a (left panel) and m_χ (right panel). Both panels show that the values of M_a (m_χ) for which $\Omega h^2 = 0.12$ do not depend strongly on the precise choice of $\tan\beta$. For choices of $\tan\beta \simeq 0.6$ the relic density becomes
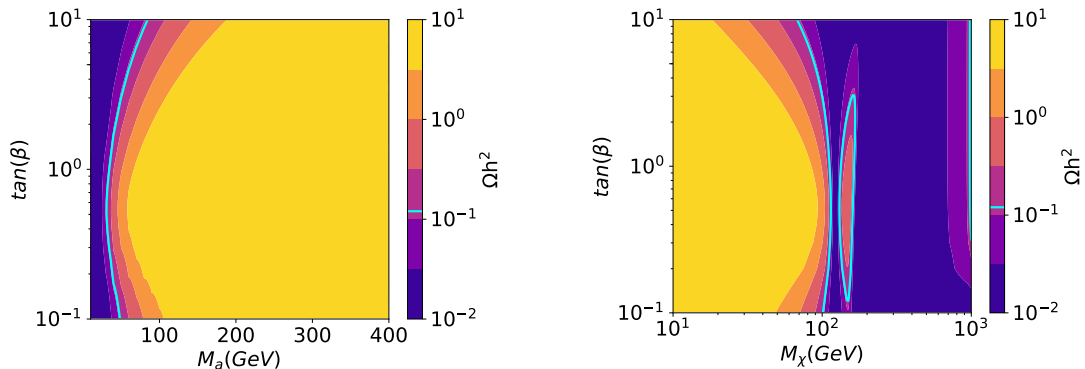
Figure 29: Predicted DM relic density in the 2HDM+a model in the $M_a - \tan\beta$ (left panel) and $m_\chi - \tan\beta$ (right panel) plane, respectively. In the left (right) panel, $m_\chi = 10\,\text{GeV}$ ($m_a = 250\,\text{GeV}$) is employed as well as $M_H = M_A = M_{H^\pm} = 600\,\text{GeV}$. The color coding is identical to Figure 27.

maximal and steadily decreases for larger and smaller values of $\tan\beta$. In the case of the $m_\chi - \tan\beta$ scan, the reduction of the DM relic density at $\tan\beta \simeq 0.1$ and $\tan\beta \simeq 3$ leads to the disappearance of the overabundant island around $m_\chi \simeq M_a/2$.

11 Proposed parameter scans

The discussion of the theoretical motivations presented in Section 4 together with our explicit studies in Sections 6, 7, 8, 9 and 10 suggest certain benchmarks for the parameters given in (3.7). In this section, we describe how the parameter space of the 2HDM+a model can be effectively explored through two-dimensional (2D) and one-dimensional (1D) scans of five input parameters: a common 2HDM heavy spin-0 boson mass $M_H = M_A = M_{H^\pm}$, the pseudoscalar mass M_a, the sine of the mixing angle $\sin\theta$, the ratio $\tan\beta$ of VEVs of the two 2HDM Higgs doublets and the DM mass m_χ. The benchmark scenarios proposed in this white paper are a product of the work of the LHC Dark Matter Working Group members and have been agreed upon [180]. They are not meant to provide an exhaustive scan of the entire 2HDM+a parameter space, but are supposed to highlight many of the features that are special in the model, to showcase the complementarity of the various signatures and to ensure that the results of different analyses can be compared consistently.

11.1 Scan in the M_a, $M_H = M_A = M_{H^\pm}$ plane

The main 2D parameter grid proposed to explore the 2HDM+a model with LHC data spans the combination of the pseudoscalar mass M_a and a common heavy 2HDM spin-0 boson mass $M_H = M_A = M_{H^\pm}$. The proposed values of the remaining 2HDM+a parameters are given in (4.5). Two example scans in the suggested mass-mass plane are given in the upper panels of Figures 21 and 22. These plots show the results of our sensitivity studies in the $h(b\bar{b}) + E_T^{\text{miss}}$ and $Z(\ell^+\ell^-) + E_T^{\text{miss}}$ channel, respectively, and are based on $36\,\text{fb}^{-1}$ of $13\,\text{TeV}$ LHC data. From the figures it is evident that in the benchmark scenario (4.5),

one can already probe M_a values up to almost $350\,\text{GeV}$ and common heavy 2HDM spin-0 boson masses in the range of around $[300, 1000]\,\text{GeV}$ with existing data. The interpretation of other mono-X channels such as $tW + E_T^{\text{miss}}$, $t\bar{t} + E_T^{\text{miss}}$ and $j + E_T^{\text{miss}}$ (cf. Section 6) as well as non-E_T^{miss} searches for final states like $\tau^+\tau^-$, tb and $t\bar{t}t\bar{t}$ (cf. Section 7) in this plane will allow to illustrate the complementary of the different search strategies for the spin-0 2HDM+a states at the LHC. Furthermore, combinations of the results of different searches can be done consistently for (4.5) and are expected to cover more parameter space than considering one signature at a time.

11.2   Scan in the $M_a-\tan\beta$ plane

A 2D scan in the $M_a-\tan\beta$ plane with the common heavy 2HDM spin-0 boson masses fixed to $M_H = M_A = M_{H^\pm} = 600\,\text{GeV}$ is proposed. The remaining parameters should be chosen as in (4.5). Two examples of such a scan can be found in the lower panels of Figures 21 and 22. With $36\,\text{fb}^{-1}$ of $13\,\text{TeV}$ LHC data, mono-Higgs and mono-Z searches are already sensitive to $\tan\beta = \mathcal{O}(1)$ values for M_a values up to around $300\,\text{GeV}$. Other mono-X searches like $t\bar{t} + E_T^{\text{miss}}$ and $j + E_T^{\text{miss}}$ are at present only sensitive to $\tan\beta \lesssim 0.5$, which emphasises the special role that resonant E_T^{miss} signatures such as $h + E_T^{\text{miss}}$, $Z + E_T^{\text{miss}}$ and $tW + E_T^{\text{miss}}$ play in the 2HDM+a model (see Section 6.1). Like the mass-mass plane discussed before, also the $M_a-\tan\beta$ plane offers a nice way to compare and to contrast the LHC reach of E_T^{miss} and non-E_T^{miss} searches in the 2HDM+a context.

11.3   Scans in $\sin\theta$

Two 1D scans in $\sin\theta$ are also proposed, one with $M_H = M_A = M_{H^\pm} = 600\,\text{GeV}$ and $M_a = 200\,\text{GeV}$ and a second one with $M_H = M_A = M_{H^\pm} = 1000\,\text{GeV}$ and $M_a = 350\,\text{GeV}$. In both scans, the remaining parameters should be set equal to (4.5). We recommend the scans in $\sin\theta$ because they will allow for a further comparison of the sensitivities of the mono-Higgs and mono-Z searches given that these two channels have a different $\sin\theta$ dependence (cf. Figure 13). We add that for the two proposed scans only values of $\sin\theta < 0.75$ and $\sin\theta < 0.45$ will lead to a scalar potential that satisfies the BFB conditions. This follows from the inequality (4.3).

11.4   Scan in m_χ

To make contact to DD, ID and DM relic density calculations, which are strongly dependent on the DM mass, we also recommend to perform 1D scans in m_χ spanning from $1\,\text{GeV}$ to $500\,\text{GeV}$. The spin-0 boson masses should be taken as $M_H = M_A = M_{H^\pm} = 600\,\text{GeV}$ and $M_a = 250\,\text{GeV}$ in these scans and the other 2HDM+a parameters set to (4.5). We recall that for masses $m_\chi \simeq M_a/2$ the observed DM relic density can be obtained (cf. Section 10). Such fine-tuned 2HDM+a scenarios are hence in agreement with cosmological observations (assuming a standard freeze-out picture) and it should be possible to probe/exclude them with the help of the LHC, since the mono-X signatures are largely insensitive to the precise choice of the DM mass as long as $m_\chi < M_a/2$ (cf. Figure 16). Other interesting parameter choices are $M_a \gtrsim 2m_t$ and $m_\chi \simeq m_t$ since in this parameter space $\Omega h^2 = 0.12$ can be obtained and such configurations can be tested with both E_T^{miss} and non-E_T^{miss} searches.

While in all our scan recommendations we have employed a common 2HDM heavy spin-0 boson mass $M_H = M_A = M_{H^\pm}$, in future 2HDM+a interpretations of LHC data one may also want to consider cases with $M_H \neq M_A$, since having a mass splitting between the H, A and $H^\pm$ can lead to interesting effects in the mono-Higgs and mono-Z searches (see Figure 12) as well as the $t\bar{t}Z$ and tbW final states (cf. the discussion in Section 7.3).

Acknowledgments

A Recasting procedure

In this appendix we discuss a general strategy that can be used to reinterpret existing $t\bar{t} + E_T^{\mathrm{miss}}$, $b\bar{b} + E_T^{\mathrm{miss}}$ and $j + E_T^{\mathrm{miss}}$ results obtained in the DMF pseudoscalar model in terms of the 2HDM+a model. Example diagrams that lead to these mono-X signatures in the 2HDM+a model are displayed in Figure 10. Only graphs involving the exchange of an a are depicted in this figure but similar diagrams with an A are not explicitly shown.

The relevance of the contributions from both the a and A in the 2HDM+a model can be demonstrated by considering the invariant mass $m_{\chi\bar{\chi}}$ of the $\chi\bar{\chi}$ system. Examples
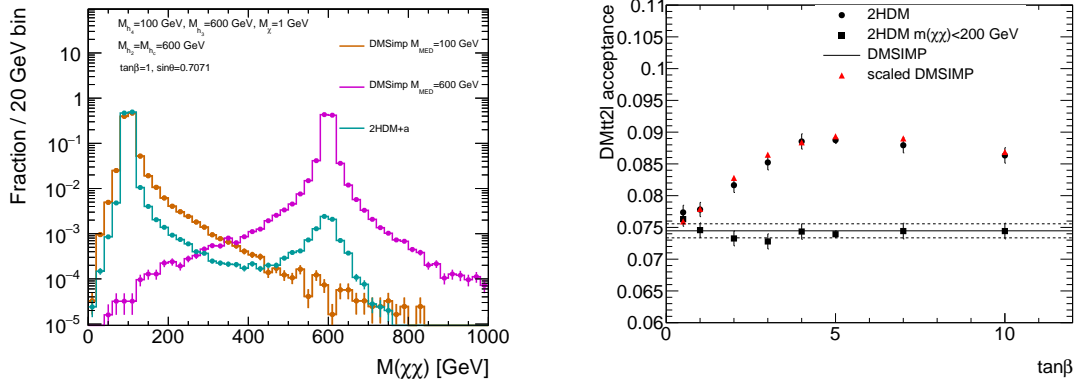
Figure 30: Left: Invariant mass of the $\chi\bar{\chi}$ system in $t\bar{t} + E_T^{\mathrm{miss}}$ production for the DMF pseudoscalar model with $M_a = 100\,\mathrm{GeV}$ (brown) and $M_a = 600\,\mathrm{GeV}$ (magenta) compared to the 2HDM+a model with $M_a = 100\,\mathrm{GeV}$, $M_H = M_A = M_{H^\pm} = 600\,\mathrm{GeV}$, $\sin\theta = 1/\sqrt{2} = 0.7071$ and $\tan\beta = 1$ (cyan). Right: Acceptances of the two-lepton $t\bar{t} + E_T^{\mathrm{miss}}$ analysis [137] as a function of $\tan\beta$. Shown are the predictions in the 2HDM+a model without (round black markers) and with the cut $m_{\chi\bar{\chi}} < 200\,\mathrm{GeV}$ (square black markers), assuming $M_a = 150\,\mathrm{GeV}$, $M_H = M_A = M_{H^\pm} = 600\,\mathrm{GeV}$ and $\sin\theta = 0.35$. The DMF pseudoscalar model result (full black line) with its statistical uncertainty (dashed black lines) as well as the acceptance $\mathcal{A}_{\mathrm{2HDM+a}}(M_a, M_A)$ (red triangles) as defined in (A.1) is also depicted.

of $m_{\chi\bar{\chi}}$ distributions in $t\bar{t} + E_T^{\mathrm{miss}}$ production are shown in the left panel of Figure 30. The brown (magenta) histogram corresponds to the prediction in the DMF pseudoscalar model assuming a mediator mass of $M_a = 100\,\mathrm{GeV}$ ($M_a = 600\,\mathrm{GeV}$), while the cyan histogram illustrates the result in the 2HDM+a model for the choices $M_a = 100\,\mathrm{GeV}$, $M_H = M_A = M_{H^\pm} = 600\,\mathrm{GeV}$, $\sin\theta = 1/\sqrt{2} = 0.7071$ and $\tan\beta = 1$. The predictions obtained in the DMF pseudoscalar model both show a single Breit-Wigner peak at $m_{\chi\bar{\chi}} = M_a$, which corresponds to the on-shell production of the mediator a that subsequently decays to a pair of DM particles. The 2HDM+a result instead features two mass peaks, one at $m_{\chi\bar{\chi}} = M_a$ and another one at $m_{\chi\bar{\chi}} = M_A$, because both pseudoscalars can be produced on-shell and then decay invisibly via either $a \to \chi\bar{\chi}$ or $A \to \chi\bar{\chi}$.

The above discussion suggests that once the contributions from a and A production are separated, $t\bar{t} + E_T^{\mathrm{miss}}$, $b\bar{b} + E_T^{\mathrm{miss}}$ and $j + E_T^{\mathrm{miss}}$ results obtained in the DMF pseudoscalar model can be mapped into the 2HDM+a parameter space. In practice, the remapping is achieved by calculating the selection acceptances $\mathcal{A}_{\mathrm{DMF}}(M_a)$ and $\mathcal{A}_{\mathrm{DMF}}(M_A)$ in the DMF pseudoscalar model and the respective cross sections $\sigma_{a,\mathrm{DMF}}$ and $\sigma_{A,\mathrm{DMF}}$. The acceptance $\mathcal{A}_{\mathrm{2HDM+a}}(M_a, M_A)$ in the 2HDM+a model is then obtained by computing the following weighted average

$$\mathcal{A}_{\mathrm{2HDM+a}}(M_a, M_A) = \frac{\mathcal{A}_{\mathrm{DMF}}(M_a)\,\sigma_{a,\mathrm{DMF}} + \mathcal{A}_{\mathrm{DMF}}(M_A)\,\sigma_{A,\mathrm{DMF}}}{\sigma_{a,\mathrm{DMF}} + \sigma_{A,\mathrm{DMF}}}. \tag{A.1}$$

In the right panel of Figure 30 we show the results that are obtained by applying
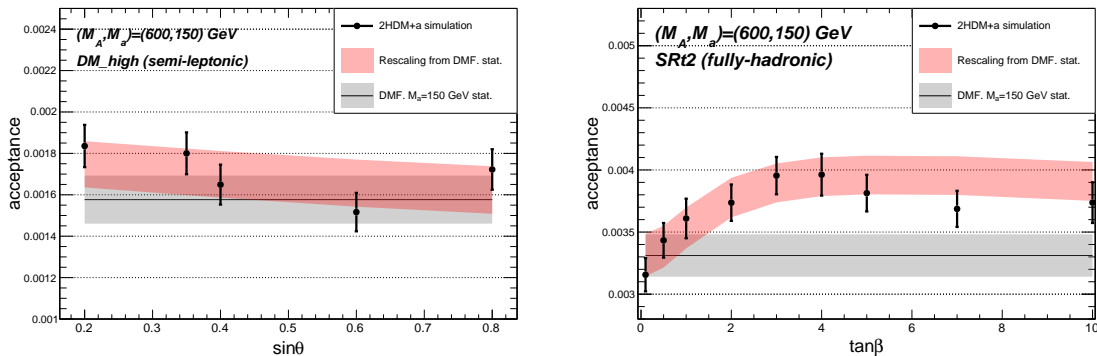
Figure 31: Validation of (A.1) in the case of the one-lepton (left panel) and the hadronic (right panel) final state arising from the $t\bar{t} + E_T^{\text{miss}}$ signature. The direct 2HDM+a calculations are indicated by the black dots and error bars, while the grey and red bands indicate the result in the DMF pseudoscalar model and the prediction obtained using the rescaling formula. In the left (right) panel, the chosen parameters are $M_a = 150\,\text{GeV}$, $M_H = M_A = M_{H^\pm} = 600\,\text{GeV}$ and $\tan\beta = 1$ ($\sin\theta = 0.35$).

the latter equation to a parton-level implementation of the two-lepton $t\bar{t} + E_T^{\text{miss}}$ analysis described in [137]. The round (square) black markers indicate the results of a direct calculation in the 2HDM+a model without a $m_{\chi\bar{\chi}}$ cut (imposing the cut $m_{\chi\bar{\chi}} < 200\,\text{GeV}$), using $M_a = 150\,\text{GeV}$, $M_H = M_A = M_{H^\pm} = 600\,\text{GeV}$ and $\sin\theta = 0.35$. The DMF pseudoscalar model result with its statistical uncertainty is represented by the solid and dashed black lines. The acceptance calculated from (A.1) is finally indicated by the red triangles. Two features are evident from the figure. First, the 2HDM+a acceptance with cut agrees with uncertainties with the acceptance of the DMF pseudoscalar model. This is expected because the cut $m_{\chi\bar{\chi}} < 200\,\text{GeV}$ strongly suppresses the A contribution in the 2HDM+a model. Second, the acceptance estimated using (A.1) agrees within uncertainties with the acceptance evaluated directly in the 2HDM+a sample.

Further validations of (A.1) are presented in Figure 31. In this figure we apply the rescaling formula to the case of the one-lepton [181] (left panel) and the hadronic [137] (right panel) final state in $t\bar{t} + E_T^{\text{miss}}$ production. The direct 2HDM+a calculations are indicated by the black dots and error bars, while the grey and red bands illustrate the result in the DMF pseudoscalar model and the prediction obtained using (A.1) including statistical uncertainties. In the left (right) panel, we have employed $M_a = 150\,\text{GeV}$, $M_H = M_A = M_{H^\pm} = 600\,\text{GeV}$ and $\tan\beta = 1$ ($\sin\theta = 0.35$). The rescaled results describe the $\sin\theta$ and $\tan\beta$ dependence of the 2HDM+a result well with uncertainties. We finally add that the formula (A.1) has also been successfully tested in the case that $|M_A - M_a| \simeq 50\,\text{GeV}$, in which case the interference between the a and A contributions is relevant.
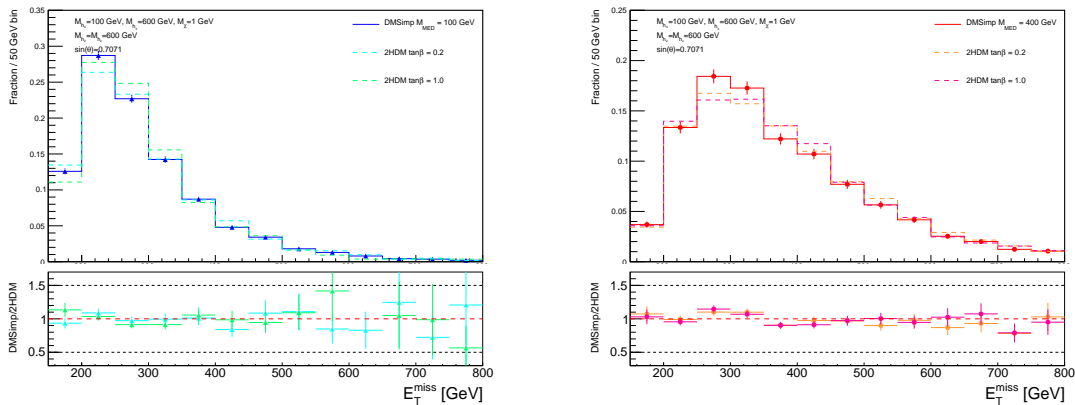
Figure 32: Normalised E_T^{miss} distributions for $t\bar{t} + E_T^{\text{miss}}$ production in the 2HDM+s model. The black curves correspond to the prediction of the DMF scalar model, while the coloured predictions illustrate the results in the 2HDM+s model. In both panels the choices $M_H = M_A = M_{H^\pm} = 600\,\text{GeV}$, $\sin\theta = 1/\sqrt{2} = 0.7071$, $m_\chi = 1\,\text{GeV}$ and either $\tan\beta = 0.2$ or $\tan\beta = 1$ have been made. The mass of the scalar mediator s is set to $M_s = 100\,\text{GeV}$ ($M_s = 400\,\text{GeV}$) in the left (right) panel.

B Distributions of the $t\bar{t} + E_T^{\text{miss}}$ signal in the 2HDM+s model

In this appendix, we present a concise study of the kinematic features of the $t\bar{t} + E_T^{\text{miss}}$ signature in the 2HDM+s model [89, 90], focusing like in the case of the 2HDM+a model on the E_T^{miss} spectrum (for the related studies in the 2HDM+a model see Section 6.2). In Figure 32, we display normalised E_T^{miss} spectra corresponding to either the 2HDM+s model (coloured curves) or the DMF scalar model (black curves). In both panels the chosen parameters are $M_H = M_A = M_{H^\pm} = 600\,\text{GeV}$, $\sin\theta = 1/\sqrt{2} = 0.7071$, $m_\chi = 1\,\text{GeV}$ and $\tan\beta = 0.2$ as well as $\tan\beta = 1$, while in the left (right) plot we have employed $M_s = 100\,\text{GeV}$ ($M_s = 400\,\text{GeV}$). We observe that the shape of the 2HDM+s distributions always resembles the corresponding one of the DMF model within uncertainties. This feature is expected because in the considered parameter benchmarks the 2HDM non-SM spin-0 states are significantly heavier than the additional scalar mediator, and thus decouple. We add that by studying simple observables like E_T^{miss} it is in principle not possible to disentangle DM-scalar from DM-pseudoscalar interactions. Angular correlations between two visible final state objects in $X + E_T^{\text{miss}}$ events can, however, serve such a purpose [139, 182–184].

C Details on the MC generation

The studies presented in this white paper are all based on MC simulations that use an `UFO` implementation of the type-II 2HDM+a model as described in Section 3. The `UFO` implementation called `Pseudoscalar_2HDM` [116] has been provided by the authors of [23] and a brief introduction to its basic usage can be found in `README.txt` [185]. Below we

MadGraph5_aMC@NLO syntax	Legend symbol	Details
`p p > t t~ t t~ / a z h1 QED<=2`	$\lvert \mathrm{SM} + \mathrm{NP} \rvert^2$	Four-top production including both SM and NP contributions and their interference.
`p p > t t~ t t~ / a z h1 QCD<=2`	$\lvert \mathrm{NP} \rvert^2$	Four-top production from NP processes, including interference terms among H, A, a.
`p p > t t~ t t~ / a z h1 QED<=0`	$\lvert \mathrm{SM} \rvert^2$	Four-top production within the SM.

Table 1: `MadGraph5_aMC@NLO` syntax used to obtain the different curves shown in the two panels in Figure 19.

give some details on the signal generation of the $t\bar{t}t\bar{t}$ channel discussed in Section 7.2 as well as the $h\left(b\bar{b}\right) + E_T^{\mathrm{miss}}$ and $Z\left(\ell^+\ell^-\right) + E_T^{\mathrm{miss}}$ signatures considered in Section 8.

C.1 Four-top signature

In Section 7.2 we have presented a study of the $t\bar{t}t\bar{t}$ channel, splitting the total four-top production cross section into three different contributions: one that only includes the SM graphs ($\lvert \mathrm{SM} \rvert^2$), another one that is due to new-physics only ($\lvert \mathrm{NP} \rvert^2$) and finally a contribution that accounts for both the SM and the 2HDM+a diagrams ($\lvert \mathrm{SM} + \mathrm{NP} \rvert^2$). In Table 1 we provide the `MadGraph5_aMC@NLO` syntax that has been used to generate the three different samples using the Pseudoscalar_2HDM `UFO`.

C.2 Mono-Higgs signature

The $h\left(b\bar{b}\right) + E_T^{\mathrm{miss}}$ sensitivity study presented in Section 8.1 is based on the generation of the signal using the Pseudoscalar_2HDM `UFO` together with `MadGraph5_aMC@NLO` and NNPDF23_lo_as_0130 parton distribution functions (PDFs) [186]. The `MadGraph5_aMC@NLO` syntax used to generate the gg-fusion contribution reads

```
import model Pseudoscalar_2HDM
g g > h1 xd xd~ [QCD]
```

where `[QCD]` indicates that one deals with a loop-induced process.

The $b\bar{b}$-fusion channel is instead generated with

```
import model Pseudoscalar_2HDM-bbMET_5FS
p p > h1 xd xd~
```

The first command loads the version of Pseudoscalar_2HDM `UFO` corresponding to the five-flavour scheme (5FS). In this only the top quark is massive while the bottom quark is massless and thus can appear as a parton in the colliding protons. Both the top and bottom Yukawa coupling are, however, non-zero.
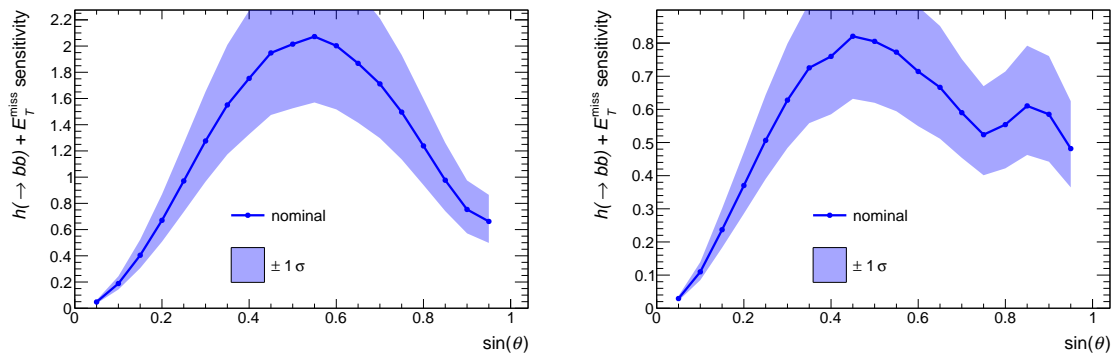
Figure 33: Estimated sensitivities of the $h\,(b\bar{b}) + E_T^{\mathrm{miss}}$ channel as a function of $\sin\theta$. The left (right) panel shows our results for $M_H = M_A = M_{H^\pm} = 600\,\mathrm{GeV}$ and $M_a = 200\,\mathrm{GeV}$ ($M_H = M_A = M_{H^\pm} = 1000\,\mathrm{GeV}$ and $M_a = 350\,\mathrm{GeV}$). The remaining parameters are set equal to (4.5). The sensitivities (points and curves), defined as the sum (8.1) over E_T^{miss} bins, as well as the uncertainty on the sensitivities (shaded bands) are based on the limits and uncertainties given in [160]. Bins with no content have a negligible sensitivity.

C.3   Mono-Z signature

The event samples that have been employed in the $Z\,(\ell^+\ell^-) + E_T^{\mathrm{miss}}$ sensitivity study (see Section 8.2) have been obtained using the Pseudoscalar_2HDM `UFO` in conjunction with `MadGraph5_aMC@NLO`, `NNPDF30_lo_as_0130` PDFs [187] and `PYTHIA 8.2` [188] for parton showering. The `MadGraph5_aMC@NLO` syntax that should be used to generate the gg-fusion process including the decay to charge leptons is

```
import model Pseudoscalar_2HDM
g g > l+ l- xd xd~ / h1 [QCD]
```

with $l = e$ or μ. To increase the efficiency of the event generation, Feynman diagrams with an intermediate s-channel SM Higgs boson have been explicitly rejected using the `MadGraph5_aMC@NLO` syntax `/ h1`.

In the case of the $b\bar{b}$-fusion channel the commands

```
import model Pseudoscalar_2HDM-bbMET_5FS
p p > l+ l- xd xd~ / h1 a
```

should instead been used. By loading the Pseudoscalar_2HDM-bbMET_5FS `UFO` the calculation is again performed in the 5FS and the `MadGraph5_aMC@NLO` syntax `/ h1 a` removes contributions with an intermediate Higgs or photon.

C.4   Heavy flavour signatures

In case of the generation of heavy flavour signatures, one must consider which flavour scheme to employ between the 5FS and four-flavour scheme (4FS). The 5FS is preferred to
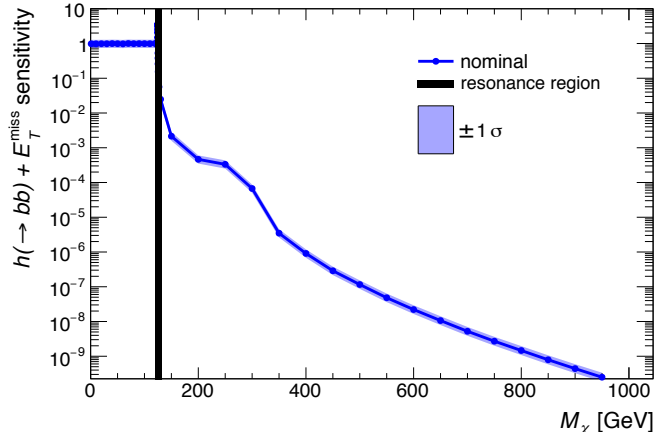
Figure 34: Estimated sensitivities of the $h\,(b\bar{b}) + E_T^{\mathrm{miss}}$ channel as a function of m_χ. The results shown correspond to $M_H = M_A = M_{H^\pm} = 600\,\mathrm{GeV}$, $M_a = 250\,\mathrm{GeV}$ and the parameter choices made in (4.5). The colour coding resembles that used in Figure 33. It is recommended to stay at least $1\,\mathrm{GeV}$ away from the region where $M_a = 2m_\chi$ to avoid numerical effects from the resonance in the generation.

keep the model predictions simpler to generate and to use, while a 4FS scheme may be more suitable if the mediator a is not much heavier that the bottom quark (i.e. $m_a \lesssim 20\,\mathrm{GeV}$) and the E_T^{miss} requirement imposed in the search is not large.

D Details on the mono-Higgs sensitivity study

In this appendix, we show additional results of our sensitivity study of the $h\,(b\bar{b}) + E_T^{\mathrm{miss}}$ signature presented in Section 8.1. Figure 33 displays the estimated sensitivities for the two $\sin\theta$ benchmarks recommended in Section 11, i.e. $M_H = M_A = M_{H^\pm} = 600\,\mathrm{GeV}$ and $M_a = 200\,\mathrm{GeV}$ (left panel) and $M_H = M_A = M_{H^\pm} = 1000\,\mathrm{GeV}$ and $M_a = 350\,\mathrm{GeV}$ (right panel). From the panels, one observes that for the benchmark value $\sin\theta = 0.35$ introduced in (4.5) the sensitivity of the mono-Higgs is enhanced compared to the choices $\sin\theta = 0.15$ and $\sin\theta = 0.7$ employed in Figure 13. In Figure 34 we furthermore plot the expected sensitivity of the $h\,(b\bar{b}) + E_T^{\mathrm{miss}}$ search as a function of the DM mass m_χ. The results shown correspond to $M_H = M_A = M_{H^\pm} = 600\,\mathrm{GeV}$, $M_a = 250\,\mathrm{GeV}$ and the choices made in (4.5). With the present data set mono-Higgs searches have already sensitivity to DM masses up to around $m_\chi \simeq M_a/2 = 125\,\mathrm{GeV}$. Recalling that the observed DM relic density can be obtained for $m_\chi \simeq M_a/2$ (see Section 10), the latter finding implies that the LHC can already test 2HDM+a scenarios that predict the correct value of Ωh^2.

References

[1] F. Kahlhoefer, *Review of LHC Dark Matter Searches*, *Int. J. Mod. Phys.* **A32** (2017), no. 13 1730006, [`arXiv:1702.02430`].

[2] G. Bertone, D. Hooper, and J. Silk, *Particle dark matter: Evidence, candidates and constraints*, *Phys. Rept.* **405** (2005) 279–390, [`hep-ph/0404175`].

[3] Q.-H. Cao, C.-R. Chen, C. S. Li, and H. Zhang, *Effective Dark Matter Model: Relic density, CDMS II, Fermi LAT and LHC*, *JHEP* **1108** (2011) 018, [`arXiv:0912.4511`].

[4] M. Beltran, D. Hooper, E. W. Kolb, Z. A. Krusberg, and T. M. Tait, *Maverick dark matter at colliders*, *JHEP* **1009** (2010) 037, [`arXiv:1002.4137`].

[5] J. Goodman, M. Ibe, A. Rajaraman, W. Shepherd, T. M. Tait, et al., *Constraints on Light Majorana dark Matter from Colliders*, *Phys.Lett.* **B695** (2011) 185–188, [`arXiv:1005.1286`].

[6] Y. Bai, P. J. Fox, and R. Harnik, *The Tevatron at the Frontier of Dark Matter Direct Detection*, *JHEP* **1012** (2010) 048, [`arXiv:1005.3797`].

[7] J. Goodman, M. Ibe, A. Rajaraman, W. Shepherd, T. M. Tait, et al., *Constraints on Dark Matter from Colliders*, *Phys.Rev.* **D82** (2010) 116010, [`arXiv:1008.1783`].

[8] P. J. Fox, R. Harnik, J. Kopp, and Y. Tsai, *Missing Energy Signatures of Dark Matter at the LHC*, *Phys. Rev.* **D85** (2012) 056011, [`arXiv:1109.4398`].

[9] J. Abdallah et al., *Simplified Models for Dark Matter Searches at the LHC*, *Phys. Dark Univ.* **9-10** (2015) 8–23, [`arXiv:1506.03116`].

[10] D. Abercrombie et al., *Dark Matter Benchmark Models for Early LHC Run-2 Searches: Report of the ATLAS/CMS Dark Matter Forum*, `arXiv:1507.00966`.

[11] A. Boveia et al., *Recommendations on presenting LHC searches for missing transverse energy signals using simplified s-channel models of dark matter*, `arXiv:1603.04156`.

[12] A. Albert et al., *Recommendations of the LHC Dark Matter Working Group: Comparing LHC searches for heavy mediators of dark matter production in visible and invisible decay channels*, `arXiv:1703.05703`.

[13] M. Chala, F. Kahlhoefer, M. McCullough, G. Nardini, and K. Schmidt-Hoberg, *Constraining Dark Sectors with Monojets and Dijets*, *JHEP* **07** (2015) 089, [`arXiv:1503.05916`].

[14] N. F. Bell, Y. Cai, J. B. Dent, R. K. Leane, and T. J. Weiler, *Dark matter at the LHC: Effective field theories and gauge invariance*, *Phys. Rev.* **D92** (2015), no. 5 053008, [`arXiv:1503.07874`].

[15] F. Kahlhoefer, K. Schmidt-Hoberg, T. Schwetz, and S. Vogl, *Implications of unitarity and gauge invariance for simplified dark matter models*, *JHEP* **02** (2016) 016, [`arXiv:1510.02110`].

[16] N. F. Bell, Y. Cai, and R. K. Leane, *Mono-W Dark Matter Signals at the LHC: Simplified Model Analysis*, *JCAP* **1601** (2016), no. 01 051, [`arXiv:1512.00476`].

[17] U. Haisch, F. Kahlhoefer, and T. M. P. Tait, *On Mono-W Signatures in Spin-1 Simplified Models*, *Phys. Lett.* **B760** (2016) 207–213, [`arXiv:1603.01267`].

[18] C. Englert, M. McCullough, and M. Spannowsky, *S-Channel Dark Matter Simplified Models and Unitarity*, *Phys. Dark Univ.* **14** (2016) 48–56, [`arXiv:1604.07975`].

[19] P. Ko, A. Natale, M. Park, and H. Yokoya, *Simplified DM models with the full SM gauge symmetry: the case of t-channel colored scalar mediators*, *JHEP* **01** (2017) 086, [arXiv:1605.07058].

[20] S. Ipek, D. McKeen, and A. E. Nelson, *A Renormalizable Model for the Galactic Center Gamma Ray Excess from Dark Matter Annihilation*, *Phys. Rev.* **D90** (2014), no. 5 055021, [arXiv:1404.3716].

[21] J. M. No, *Looking through the pseudoscalar portal into dark matter: Novel mono-Higgs and mono-Z signatures at the LHC*, *Phys. Rev.* **D93** (2016), no. 3 031701, [arXiv:1509.01110].

[22] D. Goncalves, P. A. N. Machado, and J. M. No, *Simplified Models for Dark Matter Face their Consistent Completions*, *Phys. Rev.* **D95** (2017), no. 5 055027, [arXiv:1611.04593].

[23] M. Bauer, U. Haisch, and F. Kahlhoefer, *Simplified dark matter models with two Higgs doublets: I. Pseudoscalar mediators*, *JHEP* **05** (2017) 138, [arXiv:1701.07427].

[24] P. Tunney, J. M. No, and M. Fairbairn, *Probing the pseudoscalar portal to dark matter via $\bar{b}bZ(\to \ell\ell) + \not{E}_T$: From the LHC to the Galactic Center excess*, *Phys. Rev.* **D96** (2017), no. 9 095020, [arXiv:1705.09670].

[25] P. J. Fox, R. Harnik, J. Kopp, and Y. Tsai, *LEP Shines Light on Dark Matter*, *Phys. Rev.* **D84** (2011) 014028, [arXiv:1103.0240].

[26] I. M. Shoemaker and L. Vecchi, *Unitarity and Monojet Bounds on Models for DAMA, CoGeNT, and CRESST-II*, *Phys. Rev.* **D86** (2012) 015023, [arXiv:1112.5457].

[27] G. Busoni, A. De Simone, E. Morgante, and A. Riotto, *On the Validity of the Effective Field Theory for Dark Matter Searches at the LHC*, *Phys. Lett.* **B728** (2014) 412–421, [arXiv:1307.2253].

[28] O. Buchmueller, M. J. Dolan, and C. McCabe, *Beyond Effective Field Theory for Dark Matter Searches at the LHC*, *JHEP* **01** (2014) 025, [arXiv:1308.6799].

[29] G. Busoni, A. De Simone, J. Gramling, E. Morgante, and A. Riotto, *On the Validity of the Effective Field Theory for Dark Matter Searches at the LHC, Part II: Complete Analysis for the s-channel*, *JCAP* **1406** (2014) 060, [arXiv:1402.1275].

[30] G. Busoni, A. De Simone, T. Jacques, E. Morgante, and A. Riotto, *On the Validity of the Effective Field Theory for Dark Matter Searches at the LHC Part III: Analysis for the t-channel*, *JCAP* **1409** (2014) 022, [arXiv:1405.3101].

[31] D. Racco, A. Wulzer, and F. Zwirner, *Robust collider limits on heavy-mediator Dark Matter*, *JHEP* **05** (2015) 009, [arXiv:1502.04701].

[32] S. Bruggisser, F. Riva, and A. Urbano, *The Last Gasp of Dark Matter Effective Theory*, *JHEP* **11** (2016) 069, [arXiv:1607.02475].

[33] S. Bruggisser, F. Riva, and A. Urbano, *Strongly Interacting Light Dark Matter*, *SciPost Phys.* **3** (2017), no. 3 017, [arXiv:1607.02474].

[34] D. Curtin et al., *Exotic decays of the 125 GeV Higgs boson*, *Phys. Rev.* **D90** (2014), no. 7 075004, [arXiv:1312.4992].

[35] U. Haisch, J. F. Kamenik, A. Malinauskas, and M. Spira, *Collider constraints on light pseudoscalars*, *JHEP* **03** (2018) 178, [arXiv:1802.02156].

[36] F. Maltoni, K. Paul, T. Stelzer, and S. Willenbrock, *Associated production of Higgs and single top at hadron colliders*, *Phys. Rev.* **D64** (2001) 094023, [hep-ph/0106293].

[37] M. Farina, C. Grojean, F. Maltoni, E. Salvioni, and A. Thamm, *Lifting degeneracies in Higgs couplings using single top production in association with a Higgs boson*, JHEP **05** (2013) 022, [arXiv:1211.3736].

[38] P. Pani and G. Polesello, *Dark matter production in association with a single top-quark at the LHC in a two-Higgs-doublet model with a pseudoscalar mediator*, Phys. Dark Univ. **21** (2018) 8–15, [arXiv:1712.03874].

[39] U. Haisch, F. Kahlhoefer, and J. Unwin, *The impact of heavy-quark loops on LHC dark matter searches*, JHEP **1307** (2013) 125, [arXiv:1208.4605].

[40] P. J. Fox and C. Williams, *Next-to-Leading Order Predictions for Dark Matter Production at Hadron Colliders*, Phys.Rev. **D87** (2013) 054030, [arXiv:1211.6390].

[41] M. R. Buckley, D. Feld, and D. Goncalves, *Scalar Simplified Models for Dark Matter*, Phys. Rev. **D91** (2015) 015017, [arXiv:1410.6497].

[42] P. Harris, V. V. Khoze, M. Spannowsky, and C. Williams, *Constraining Dark Sectors at Colliders: Beyond the Effective Theory Approach*, Phys. Rev. **D91** (2015) 055009, [arXiv:1411.0535].

[43] U. Haisch and E. Re, *Simplified dark matter top-quark interactions at the LHC*, JHEP **06** (2015) 078, [arXiv:1503.00691].

[44] O. Mattelaer and E. Vryonidou, *Dark matter production through loop-induced processes at the LHC: the s-channel mediator case*, Eur. Phys. J. **C75** (2015), no. 9 436, [arXiv:1508.00564].

[45] M. Backovic, M. Krämer, F. Maltoni, A. Martini, K. Mawatari, and M. Pellen, *Higher-order QCD predictions for dark matter production at the LHC in simplified models with s-channel mediators*, Eur. Phys. J. **C75** (2015), no. 10 482, [arXiv:1508.05327].

[46] M. Neubert, J. Wang, and C. Zhang, *Higher-Order QCD Predictions for Dark Matter Production in Mono-Z Searches at the LHC*, JHEP **02** (2016) 082, [arXiv:1509.05785].

[47] C. Arina et al., *A comprehensive approach to dark matter studies: exploration of simplified top-philic models*, JHEP **11** (2016) 111, [arXiv:1605.09242].

[48] S. L. Glashow and S. Weinberg, *Natural Conservation Laws for Neutral Currents*, Phys. Rev. **D15** (1977) 1958.

[49] E. A. Paschos, *Diagonal Neutral Currents*, Phys. Rev. **D15** (1977) 1966.

[50] **ATLAS** and **CMS** Collaborations, *Measurements of the Higgs boson production and decay rates and constraints on its couplings from a combined ATLAS and CMS analysis of the LHC pp collision data at $\sqrt{s} = 7$ TeV and 8 TeV*, JHEP **08** (2016) 045, [arXiv:1606.02266].

[51] **ATLAS** Collaboration, *Combined measurements of Higgs boson production and decay using up to 80 fb^{-1} of proton–proton collision data at $\sqrt{s} = 13$ TeV collected with the ATLAS experiment*, ATLAS-CONF-2018-031, CERN, Geneva, 2018.

[52] **CMS** Collaboration, *Combined measurements of the Higgs boson couplings in proton-proton collisions at $\sqrt{s} = 13$ TeV*, arXiv:1809.10733.

[53] **ATLAS** Collaboration, *Search for heavy resonances decaying into a W or Z boson and a Higgs boson in final states with leptons and b-jets in 36 fb^{-1} of $\sqrt{s} = 13$ TeV pp collisions with the ATLAS detector*, JHEP **03** (2018) 174, [arXiv:1712.06518].

[54] **CMS** Collaboration, *Search for a heavy pseudoscalar boson decaying to a Z boson and a Higgs boson at $\sqrt{s} = 13$ TeV*, CMS-PAS-HIG-18-005, CERN, Geneva, 2018.

[55] J. F. Gunion and H. E. Haber, *The CP conserving two Higgs doublet model: The Approach to the decoupling limit*, Phys. Rev. **D67** (2003) 075019, [`hep-ph/0207010`].

[56] T. Hermann, M. Misiak, and M. Steinhauser, *$\bar{B} \to X_s\gamma$ in the Two Higgs Doublet Model up to Next-to-Next-to-Leading Order in QCD*, JHEP **11** (2012) 036, [`arXiv:1208.2788`].

[57] M. Misiak et al., *Updated NNLO QCD predictions for the weak radiative B-meson decays*, Phys. Rev. Lett. **114** (2015), no. 22 221801, [`arXiv:1503.01789`].

[58] M. Misiak and M. Steinhauser, *Weak radiative decays of the B meson and bounds on $M_{H^\pm}$ in the Two-Higgs-Doublet Model*, Eur. Phys. J. **C77** (2017), no. 3 201, [`arXiv:1702.04571`].

[59] L. F. Abbott, P. Sikivie, and M. B. Wise, *Constraints on Charged Higgs Couplings*, Phys. Rev. **D21** (1980) 1393.

[60] C. Q. Geng and J. N. Ng, *Charged Higgs Effect in B_d^0–$\bar{B}_d^0$ Mixing, $K \to \pi$ Neutrino Anti-neutrino Decay and Rare Decays of B Mesons*, Phys. Rev. **D38** (1988) 2857. [Erratum: *Phys. Rev.* **D41** (1990) 1715].

[61] A. J. Buras, P. Krawczyk, M. E. Lautenbacher, and C. Salazar, *B^0–$\bar{B}^0$ Mixing, CP Violation, $K^+ \to \pi^+\nu\bar{\nu}$ and $B \to K\gamma X$ in a Two Higgs Doublet Model*, Nucl. Phys. **B337** (1990) 284–312.

[62] M. Kirk, A. Lenz, and T. Rauh, *Dimension-six matrix elements for meson mixing and lifetimes from sum rules*, JHEP **12** (2017) 068, [`arXiv:1711.02100`].

[63] W. Skiba and J. Kalinowski, *$B_s \to \tau^+\tau^-$ decay in a two Higgs doublet model*, Nucl. Phys. **B404** (1993) 3–19.

[64] H. E. Logan and U. Nierste, *$B_{s,d} \to \ell^+\ell^-$ in a two Higgs doublet model*, Nucl. Phys. **B586** (2000) 39–55, [`hep-ph/0004139`].

[65] P. H. Chankowski and L. Slawianowska, *$B_{d,s}^0 \to \mu^+\mu^-$ decay in the MSSM*, Phys. Rev. **D63** (2001) 054012, [`hep-ph/0008046`].

[66] C. Bobeth, T. Ewerth, F. Krüger, and J. Urban, *Analysis of neutral Higgs boson contributions to the decays $\bar{B}_{(s)} \to \ell^+\ell^-$ and $\bar{B} \to K\ell^+\ell^-$*, Phys. Rev. **D64** (2001) 074014, [`hep-ph/0104284`].

[67] C. Bobeth, M. Gorbahn, T. Hermann, M. Misiak, E. Stamou, and M. Steinhauser, *$B_{s,d} \to l^+l^-$ in the Standard Model with Reduced Theoretical Uncertainty*, Phys. Rev. Lett. **112** (2014) 101801, [`arXiv:1311.0903`].

[68] **LHCb** and **CMS** Collaborations, V. Khachatryan et al., *Observation of the rare $B_s^0 \to \mu^+\mu^-$ decay from the combined analysis of CMS and LHCb data*, Nature **522** (2015) 68–72, [`arXiv:1411.4413`].

[69] **LHCb** Collaboration, R. Aaij et al., *Measurement of the $B_s^0 \to \mu^+\mu^-$ branching fraction and effective lifetime and search for $B^0 \to \mu^+\mu^-$ decays*, Phys. Rev. Lett. **118** (2017), no. 19 191801, [`arXiv:1703.05747`].

[70] A. Denner, R. J. Guth, W. Hollik, and J. H. Kühn, *The Z width in the two Higgs doublet model*, Z. Phys. **C51** (1991) 695–705.

[71] U. Haisch and A. Weiler, *Determining the Sign of the Z-Penguin Amplitude*, Phys. Rev. **D76** (2007) 074027, [`arXiv:0706.2054`].

[72] A. Freitas and Y.-C. Huang, *Electroweak two-loop corrections to $sin^2\theta_{eff}^{b\bar{b}}$ and R_b using numerical Mellin-Barnes integrals*, *JHEP* **08** (2012) 050, [arXiv:1205.0299]. [Erratum: *JHEP* **10** (2013) 044].

[73] **ATLAS** Collaboration, *Search for additional heavy neutral Higgs and gauge bosons in the ditau final state produced in 36 fb^{-1} of pp collisions at $\sqrt{s}$ = 13 TeV with the ATLAS detector*, *JHEP* **01** (2018) 055, [arXiv:1709.07242].

[74] **CMS** Collaboration, *Search for additional neutral MSSM Higgs bosons in the $\tau\tau$ final state in proton-proton collisions at $\sqrt{s}$ = 13 TeV*, *JHEP* **09** (2018) 007, [arXiv:1803.06553].

[75] **ATLAS** Collaboration, *Search for Heavy Higgs Bosons A/H Decaying to a Top Quark Pair in pp Collisions at $\sqrt{s}$ = 8 TeV with the ATLAS Detector*, *Phys. Rev. Lett.* **119** (2017), no. 19 191803, [arXiv:1707.06025].

[76] **ATLAS** Collaboration, *Search for new phenomena in $t\bar{t}$ final states with additional heavy-flavour jets in pp collisions at $\sqrt{s}$ = 13 TeV with the ATLAS detector*, ATLAS-CONF-2016-104, CERN, Geneva, 2016.

[77] **CMS** Collaboration, A. M. Sirunyan et al., *Search for standard model production of four top quarks with same-sign and multilepton final states in pp collisions at $\sqrt{s}$ = 13 TeV*, *Eur. Phys. J.* **C78** (2018), no. 2 140, [arXiv:1710.10614].

[78] **ATLAS** Collaboration, *Search for pair production of up-type vector-like quarks and for four-top-quark events in final states with multiple b-jets with the ATLAS detector*, *JHEP* **07** (2018) 089, [arXiv:1803.09678].

[79] H. E. Haber and A. Pomarol, *Constraints from global symmetries on radiative corrections to the Higgs sector*, *Phys. Lett.* **B302** (1993) 435–441, [hep-ph/9207267].

[80] A. Pomarol and R. Vega, *Constraints on CP violation in the Higgs sector from the rho parameter*, *Nucl. Phys.* **B413** (1994) 3–15, [hep-ph/9305272].

[81] J. M. Gerard and M. Herquet, *A Twisted custodial symmetry in the two-Higgs-doublet model*, *Phys. Rev. Lett.* **98** (2007) 251802, [hep-ph/0703051].

[82] B. Grzadkowski, M. Maniatis, and J. Wudka, *The bilinear formalism and the custodial symmetry in the two-Higgs-doublet model*, *JHEP* **11** (2011) 030, [arXiv:1011.5228].

[83] H. E. Haber and D. O'Neil, *Basis-independent methods for the two-Higgs-doublet model III: The CP-conserving limit, custodial symmetry, and the oblique parameters S, T, U*, *Phys. Rev.* **D83** (2011) 055017, [arXiv:1011.6188].

[84] **ATLAS** Collaboration, *Search for heavy resonances decaying into WW in the e$\nu\mu\nu$ final state in pp collisions at $\sqrt{s}$ = 13 TeV with the ATLAS detector*, *Eur. Phys. J.* **C78** (2018), no. 1 24, [arXiv:1710.01123].

[85] **ATLAS** Collaboration, *Search for heavy ZZ resonances in the $\ell^+\ell^-\ell^+\ell^-$ and $\ell^+\ell^-\nu\bar{\nu}$ final states using proton-proton collisions at $\sqrt{s}$ = 13 TeV with the ATLAS detector*, *Eur. Phys. J.* **C78** (2018), no. 4 293, [arXiv:1712.06386].

[86] **CMS** Collaboration, *Search for beyond the standard model Higgs bosons decaying into a $b\bar{b}$ pair in pp collisions at $\sqrt{s}$ = 13 TeV*, *JHEP* **08** (2018) 113, [arXiv:1805.12191].

[87] **ATLAS** Collaboration, *Constraints on new phenomena via Higgs boson couplings and invisible decays with the ATLAS detector*, *JHEP* **11** (2015) 206, [arXiv:1509.00672].

[88] **CMS** Collaboration, *Searches for invisible decays of the Higgs boson in pp collisions at $\sqrt{s}$ = 7, 8, and 13 TeV*, *JHEP* **02** (2017) 135, [arXiv:1610.09218].

[89] N. F. Bell, G. Busoni, and I. W. Sanderson, *Self-consistent Dark Matter Simplified Models with an s-channel scalar mediator*, *JCAP* **1703** (2017), no. 03 015, [arXiv:1612.03475].

[90] N. F. Bell, G. Busoni, and I. W. Sanderson, *Two Higgs Doublet Dark Matter Portal*, *JCAP* **1801** (2018), no. 01 015, [arXiv:1710.10764].

[91] R. Mahbubani and L. Senatore, *The Minimal model for dark matter and unification*, *Phys. Rev.* **D73** (2006) 043510, [hep-ph/0510064].

[92] R. Enberg, P. J. Fox, L. J. Hall, A. Y. Papaioannou, and M. Papucci, *LHC and dark matter signals of improved naturalness*, *JHEP* **11** (2007) 014, [arXiv:0706.0918].

[93] T. Cohen, J. Kearney, A. Pierce, and D. Tucker-Smith, *Singlet-Doublet Dark Matter*, *Phys. Rev.* **D85** (2012) 075003, [arXiv:1109.2604].

[94] C. Cheung and D. Sanford, *Simplified Models of Mixed Dark Matter*, *JCAP* **1402** (2014) 011, [arXiv:1311.5896].

[95] A. Berlin, S. Gori, T. Lin, and L.-T. Wang, *Pseudoscalar Portal Dark Matter*, *Phys. Rev.* **D92** (2015) 015005, [arXiv:1502.06000].

[96] G. Arcadi, *2HDM portal for Singlet-Doublet Dark Matter*, arXiv:1804.04930.

[97] M. Bauer, M. Klassen, and V. Tenorth, *Universal properties of pseudoscalar mediators in dark matter extensions of 2HDMs*, *JHEP* **07** (2018) 107, [arXiv:1712.06597].

[98] N. G. Deshpande and E. Ma, *Pattern of Symmetry Breaking with Two Higgs Doublets*, *Phys. Rev.* **D18** (1978) 2574.

[99] R. Barbieri, L. J. Hall, and V. S. Rychkov, *Improved naturalness with a heavy Higgs: An Alternative road to LHC physics*, *Phys.Rev.* **D74** (2006) 015007, [hep-ph/0603188].

[100] Q.-H. Cao, E. Ma, and G. Rajasekaran, *Observing the Dark Scalar Doublet and its Impact on the Standard-Model Higgs Boson at Colliders*, *Phys. Rev.* **D76** (2007) 095011, [arXiv:0708.2939].

[101] E. Dolle, X. Miao, S. Su, and B. Thomas, *Dilepton Signals in the Inert Doublet Model*, *Phys.Rev.* **D81** (2010) 035003, [arXiv:0909.3094].

[102] X. Miao, S. Su, and B. Thomas, *Trilepton Signals in the Inert Doublet Model*, *Phys. Rev.* **D82** (2010) 035009, [arXiv:1005.0090].

[103] M. Gustafsson, S. Rydbeck, L. Lopez-Honorez, and E. Lundstrom, *Status of the Inert Doublet Model and the Role of multileptons at the LHC*, *Phys.Rev.* **D86** (2012) 075019, [arXiv:1206.6316].

[104] G. Belanger, B. Dumont, A. Goudelis, B. Herrmann, S. Kraml, and D. Sengupta, *Dilepton constraints in the Inert Doublet Model from Run 1 of the LHC*, *Phys. Rev.* **D91** (2015), no. 11 115011, [arXiv:1503.07367].

[105] A. Ilnicka, M. Krawczyk, and T. Robens, *Inert Doublet Model in light of LHC Run I and astrophysical data*, *Phys. Rev.* **D93** (2016), no. 5 055026, [arXiv:1508.01671].

[106] P. Poulose, S. Sahoo, and K. Sridhar, *Exploring the Inert Doublet Model through the dijet plus missing transverse energy channel at the LHC*, *Phys. Lett.* **B765** (2017) 300–306, [arXiv:1604.03045].

[107] A. Datta, N. Ganguly, N. Khan, and S. Rakshit, *Exploring collider signatures of the inert Higgs doublet model*, *Phys. Rev.* **D95** (2017), no. 1 015017, [arXiv:1610.00648].

[108] M. Hashemi and S. Najjari, *Observability of Inert Scalars at the LHC*, *Eur. Phys. J.* **C77** (2017), no. 9 592, [arXiv:1611.07827].

[109] **LHC Higgs Cross Section Working Group** Collaboration, D. de Florian et al., *Handbook of LHC Higgs Cross Sections: 4. Deciphering the Nature of the Higgs Sector*, arXiv:1610.07922.

[110] A. Belyaev, G. Cacciapaglia, I. P. Ivanov, F. Rojas-Abatte, and M. Thomas, *Anatomy of the Inert Two Higgs Doublet Model in the light of the LHC and non-LHC Dark Matter Searches*, *Phys. Rev.* **D97** (2018), no. 3 035011, [arXiv:1612.00511].

[111] B. Dutta, G. Palacio, J. D. Ruiz-Alvarez, and D. Restrepo, *Vector Boson Fusion in the Inert Doublet Model*, *Phys. Rev.* **D97** (2018), no. 5 055045, [arXiv:1709.09796].

[112] N. Wan, N. Li, B. Zhang, H. Yang, M.-F. Zhao, M. Song, G. Li, and J.-Y. Guo, *Searches for Dark Matter via Mono-W Production in Inert Doublet Model at the LHC*, *Commun. Theor. Phys.* **69** (2018), no. 5 617.

[113] S. von Buddenbrock, N. Chakrabarty, A. S. Cornell, D. Kar, M. Kumar, T. Mandal, B. Mellado, B. Mukhopadhyaya, R. G. Reed, and X. Ruan, *Phenomenological signatures of additional scalar bosons at the LHC*, *Eur. Phys. J.* **C76** (2016), no. 10 580, [arXiv:1606.01674].

[114] **ATLAS** Collaboration, *Search for dark matter in association with a Higgs boson decaying to two photons at $\sqrt{s} = 13$ TeV with the ATLAS detector*, *Phys. Rev.* **D96** (2017), no. 11 112004, [arXiv:1706.03948].

[115] C. Degrande, C. Duhr, B. Fuks, D. Grellscheid, O. Mattelaer, and T. Reiter, *UFO - The Universal FeynRules Output*, *Comput. Phys. Commun.* **183** (2012) 1201–1214, [arXiv:1108.2040].

[116] M. Bauer, U. Haisch, and F. Kahlhoefer, 2017. Available at https://github.com/LHC-DMWG/model-repository/tree/master/models/Pseudoscalar_2HDM.

[117] J. Alwall, R. Frederix, S. Frixione, V. Hirschi, F. Maltoni, O. Mattelaer, H. S. Shao, T. Stelzer, P. Torrielli, and M. Zaro, *The automated computation of tree-level and next-to-leading order differential cross sections, and their matching to parton shower simulations*, *JHEP* **07** (2014) 079, [arXiv:1405.0301].

[118] **ATLAS** Collaboration, *Search for Dark Matter Produced in Association with a Higgs Boson decaying to $b\bar{b}$ at $\sqrt{s} = 13$ TeV with the ATLAS Detector using $79.8\,fb^{-1}$ of proton-proton collision data*, ATLAS-CONF-2018-039, CERN, Geneva, 2018.

[119] **CMS** Collaboration, *Search for associated production of dark matter with a Higgs boson that decays to a pair of bottom quarks*, CMS-PAS-EXO-16-050, CERN, Geneva, 2018.

[120] **CMS** Collaboration, *Search for dark matter produced in association with a Higgs boson decaying to $\gamma\gamma$ or $\tau^+\tau^-$ at $\sqrt{s} = 13$ TeV*, *JHEP* **09** (2018) 048, [arXiv:1806.04771].

[121] **CMS** Collaboration, *Search for heavy resonances decaying into a vector boson and a Higgs boson in final states with charged leptons, neutrinos and b quarks at $\sqrt{s} = 13$ TeV*, [arXiv:1807.02826].

[122] G. Polesello, *Turning every stone at the LHC: diverse signatures with the 2HDM+a model*, Dark Matter @ LHC 2018, Heidelberg, Germany, April 3-6, 2018. Available at https://indico.cern.ch/event/669891/contributions/2813354/attachments/1626592/2590540/polesello_heidelberg.pdf.

[123] **ATLAS** Collaboration, *Search for an invisibly decaying Higgs boson or dark matter candidates produced in association with a Z boson in pp collisions at $\sqrt{s} = 13$ TeV with the ATLAS detector*, Phys. Lett. **B776** (2018) 318–337, [arXiv:1708.09624].

[124] **CMS** Collaboration, *Search for new physics in events with a leptonically decaying Z boson and a large transverse momentum imbalance in proton-proton collisions at $\sqrt{s} = 13$ TeV*, Eur. Phys. J. **C78** (2018), no. 4 291, [arXiv:1711.00431].

[125] F. J. Petriello, S. Quackenbush, and K. M. Zurek, *The Invisible Z′ at the CERN LHC*, Phys. Rev. **D77** (2008) 115020, [arXiv:0803.4005].

[126] N. F. Bell, J. B. Dent, A. J. Galea, T. D. Jacques, L. M. Krauss, and J. Thomas, *Searching for dark matter at the LHC with a mono-Z*, Phys. Rev. **D86** (2012) 096011, [arXiv:1209.0231].

[127] L. M. Carpenter, A. Nelson, C. Shimmin, T. M. P. Tait, and D. Whiteson, *Collider searches for dark matter in events with a Z boson and missing energy*, Phys. Rev. **D87** (2013), no. 7 074005, [arXiv:1212.3352].

[128] **ATLAS** Collaboration, *Search for dark matter in events with a hadronically decaying W or Z boson and missing transverse momentum in pp collisions at $\sqrt{s} = 8$ TeV with the ATLAS detector*, Phys. Rev. Lett. **112** (2014), no. 4 041802, [arXiv:1309.4017].

[129] **CMS** Collaboration, *Search for new physics in final states with an energetic jet or a hadronically decaying W or Z boson and transverse momentum imbalance at $\sqrt{s} = 13$ TeV*, Phys. Rev. **D97** (2018), no. 9 092005, [arXiv:1712.02345].

[130] D. Pinna, A. Zucchetta, M. R. Buckley, and F. Canelli, *Single top quarks and dark matter*, Phys. Rev. **D96** (2017), no. 3 035031, [arXiv:1701.05195].

[131] T. Plehn, J. Thompson, and S. Westhoff, *Dark Matter from Electroweak Single Top Production*, Phys. Rev. **D98** (2018), no. 1 015012, [arXiv:1712.08065].

[132] P. Konar, K. Kong, K. T. Matchev, and M. Park, *Dark Matter Particle Spectroscopy at the LHC: Generalizing M_{T2} to Asymmetric Event Topologies*, JHEP **04** (2010) 086, [arXiv:0911.4126].

[133] C. G. Lester and B. Nachman, *Bisection-based asymmetric M_{T2} computation: a higher precision calculator than existing symmetric methods*, JHEP **03** (2015) 100, [arXiv:1411.4312].

[134] C. G. Lester and D. J. Summers, *Measuring masses of semiinvisibly decaying particles pair produced at hadron colliders*, Phys. Lett. **B463** (1999) 99–103, [hep-ph/9906349].

[135] A. Barr, C. Lester, and P. Stephens, *m_{T2}: The Truth behind the glamour*, J. Phys. **G29** (2003) 2343–2363, [hep-ph/0304226].

[136] **CMS** Collaboration, *Search for dark matter produced in association with a single top quark or a top quark pair*, CMS-PAS-EXO-18-010, CERN, Geneva, 2018.

[137] **ATLAS** Collaboration, *Search for dark matter produced in association with bottom or top quarks in $\sqrt{s} = 13$ TeV pp collisions with the ATLAS detector*, Eur. Phys. J. **C78** (2018), no. 1 18, [arXiv:1710.11412].

[138] **CMS** Collaboration, *Search for dark matter particles produced in association with a top quark pair at $\sqrt{s} = 13$ TeV*, arXiv:1807.06522.

[139] U. Haisch, P. Pani, and G. Polesello, *Determining the CP nature of spin-0 mediators in associated production of dark matter and $t\bar{t}$ pairs*, *JHEP* **02** (2017) 131, [arXiv:1611.09841].

[140] **CMS** Collaboration, *Search for dark matter in association with a $t\bar{t}$ pair at $\sqrt{s}$ = 13 TeV in the dilepton channel with 2016 data*, CMS-PAS-EXO-17-014, CERN, Geneva, 2018.

[141] **ATLAS** Collaboration, *Search for dark matter and other new phenomena in events with an energetic jet and large missing transverse momentum using the ATLAS detector*, *JHEP* **01** (2018) 126, [arXiv:1711.03301].

[142] K. J. F. Gaemers and F. Hoogeveen, *Higgs Production and Decay Into Heavy Flavors With the Gluon Fusion Mechanism*, *Phys. Lett.* **146B** (1984) 347–349.

[143] D. Dicus, A. Stange, and S. Willenbrock, *Higgs decay to top quarks at hadron colliders*, *Phys. Lett.* **B333** (1994) 126–131, [hep-ph/9404359].

[144] W. Bernreuther, M. Flesch, and P. Haberl, *Signatures of Higgs bosons in the top quark decay channel at hadron colliders*, *Phys. Rev.* **D58** (1998) 114031, [hep-ph/9709284].

[145] R. Frederix and F. Maltoni, *Top pair invariant mass distribution: A Window on new physics*, *JHEP* **01** (2009) 047, [arXiv:0712.2355].

[146] B. Hespel, F. Maltoni, and E. Vryonidou, *Signal background interference effects in heavy scalar production and decay to a top-anti-top pair*, *JHEP* **10** (2016) 016, [arXiv:1606.04149].

[147] D. Buarque Franzosi, E. Vryonidou, and C. Zhang, *Scalar production and decay to top quarks including interference effects at NLO in QCD in an EFT approach*, *JHEP* **10** (2017) 096, [arXiv:1707.06760].

[148] N. Craig, F. D'Eramo, P. Draper, S. Thomas, and H. Zhang, *The Hunt for the Rest of the Higgs Bosons*, *JHEP* **06** (2015) 137, [arXiv:1504.04630].

[149] J. Hajer, Y.-Y. Li, T. Liu, and J. F. H. Shiu, *Heavy Higgs Bosons at 14 TeV and 100 TeV*, *JHEP* **11** (2015) 124, [arXiv:1504.07617].

[150] S. Gori, I.-W. Kim, N. R. Shah, and K. M. Zurek, *Closing the Wedge: Search Strategies for Extended Higgs Sectors with Heavy Flavor Final States*, *Phys. Rev.* **D93** (2016), no. 7 075038, [arXiv:1602.02782].

[151] M. Carena and Z. Liu, *Challenges and opportunities for heavy scalar searches in the $t\bar{t}$ channel at the LHC*, *JHEP* **11** (2016) 159, [arXiv:1608.07282].

[152] D. Franzosi and C. Zhang, 2014. Available at https://cp3.irmp.ucl.ac.be/projects/madgraph/wiki/Models/ggHFullLoop.

[153] E. Alvarez, D. A. Faroughy, J. F. Kamenik, R. Morales, and A. Szynkman, *Four Tops for LHC*, *Nucl. Phys.* **B915** (2017) 19–43, [arXiv:1611.05032].

[154] U. Haisch and G. Polesello, *Searching for heavy Higgs bosons in the $t\bar{t}Z$ and tbW final states*, *JHEP* **09** (2018) 151, [arXiv:1807.07734].

[155] **ATLAS** Collaboration, *Search for charged Higgs bosons produced in association with a top quark and decaying via $H^{\pm} \to \tau\nu$ using pp collision data recorded at $\sqrt{s}$ = 13 TeV by the ATLAS detector*, *Phys. Lett.* **B759** (2016) 555–574, [arXiv:1603.09203].

[156] **CMS** Collaboration, *Search for charged Higgs bosons with the $H^{\pm} \to \tau^{\pm}\nu_{\tau}$ decay channel in the fully hadronic final state at $\sqrt{s}$ = 13 TeV*, CMS-PAS-HIG-16-031, CERN, Geneva, 2016.

[157] **ATLAS** Collaboration, *Search for charged Higgs bosons in the $H^{\pm} \to tb$ decay channel in pp collisions at $\sqrt{s} = 8$ TeV using the ATLAS detector*, *JHEP* **03** (2016) 127, [arXiv:1512.03704].

[158] **CMS** Collaboration, *Search for a charged Higgs boson in pp collisions at $\sqrt{s} = 8$ TeV*, *JHEP* **11** (2015) 018, [arXiv:1508.07774].

[159] **ATLAS** Collaboration, *Search for charged Higgs bosons in the $H^{\pm} \to tb$ decay channel in pp collisions at $\sqrt{s} = 13$ TeV using the ATLAS detector*, ATLAS-CONF-2016-089, CERN, Geneva, 2016.

[160] **ATLAS** Collaboration, *Search for Dark Matter Produced in Association with a Higgs Boson Decaying to $b\bar{b}$ using $36\,fb^{-1}$ of pp collisions at $\sqrt{s} = 13$ TeV with the ATLAS Detector*, *Phys. Rev. Lett.* **119** (2017), no. 18 181804, [arXiv:1707.01302].

[161] G. Cowan, K. Cranmer, E. Gross, and O. Vitells, *Asymptotic formulae for likelihood-based tests of new physics*, *Eur. Phys. J.* **C71** (2011) 1554, [arXiv:1007.1727]. [Erratum: *Eur. Phys. J.* **C73** (2013) 2501].

[162] G. Cowan, *Discovery sensitivity for a counting experiment with background uncertainty*, 2012. Available at http://www.pp.rhul.ac.uk/~cowan/stat/medsig/medsigNote.pdf.

[163] G. Arcadi, M. Lindner, F. S. Queiroz, W. Rodejohann, and S. Vogl, *Pseudoscalar Mediators: A WIMP model at the Neutrino Floor*, *JCAP* **1803** (2018), no. 03 042, [arXiv:1711.02110].

[164] N. F. Bell, G. Busoni, and I. W. Sanderson, *Loop Effects in Direct Detection*, *JCAP* **1808** (2018), no. 08 017, [arXiv:1803.01574].

[165] T. Li, *Revisiting the direct detection of dark matter in simplified models*, *Phys. Lett.* **B782** (2018) 497–502, [arXiv:1804.02120].

[166] **LUX** Collaboration, D. S. Akerib et al., *Results from a search for dark matter in the complete LUX exposure*, *Phys. Rev. Lett.* **118** (2017), no. 2 021303, [arXiv:1608.07648].

[167] **XENON** Collaboration, E. Aprile et al., *First Dark Matter Search Results from the XENON1T Experiment*, *Phys. Rev. Lett.* **119** (2017), no. 18 181301, [arXiv:1705.06655].

[168] **XENON** Collaboration, E. Aprile et al., *Physics reach of the XENON1T dark matter experiment*, *JCAP* **1604** (2016), no. 04 027, [arXiv:1512.07501].

[169] J. Billard, L. Strigari, and E. Figueroa-Feliciano, *Implication of neutrino backgrounds on the reach of next generation dark matter direct detection experiments*, *Phys. Rev.* **D89** (2014), no. 2 023524, [arXiv:1307.5458].

[170] **XENON** Collaboration, E. Aprile et al., *Dark Matter Search Results from a One Tonne $\times$ Year Exposure of XENON1T*, *Phys. Rev. Lett.* **121** (2018), no. 11 111302, [arXiv:1805.12562].

[171] T. Abe, M. Fujiwara, and J. Hisano, *Loop corrections to dark matter direct detection in a pseudoscalar mediator dark matter model*, arXiv:1810.01039.

[172] F. Ambrogi, C. Arina, M. Backovic, J. Heisig, F. Maltoni, L. Mantani, O. Mattelaer, and G. Mohlabeng, *MadDM v.3.0: a Comprehensive Tool for Dark Matter Studies*, arXiv:1804.00044.

[173] J. D. Simon and M. Geha, *The Kinematics of the Ultra-Faint Milky Way Satellites: Solving the Missing Satellite Problem*, *Astrophys. J.* **670** (2007) 313–331, [arXiv:0706.0516].

[174] M. G. Walker, M. Mateo, and E. Olszewski, *Stellar Velocities in the Carina, Fornax, Sculptor and Sextans dSph Galaxies: Data from the Magellan/MMFS Survey*, Astron. J. **137** (2009) 3100, [arXiv:0811.0118].

[175] **DES, Fermi-LAT** Collaboration, *Searching for Dark Matter Annihilation in Recently Discovered Milky Way Satellites with Fermi-LAT*, Astrophys. J. **834** (2017), no. 2 110, [arXiv:1611.03184].

[176] L. M. Carpenter, R. Colburn, and J. Goodman, *Indirect Detection Constraints on the Model Space of Dark Matter Effective Theories*, Phys. Rev. **D92** (2015), no. 9 095011, [arXiv:1506.08841].

[177] L. M. Carpenter, R. Colburn, J. Goodman, and T. Linden, *Indirect Detection Constraints on s and t Channel Simplified Models of Dark Matter*, Phys. Rev. **D94** (2016), no. 5 055027, [arXiv:1606.04138].

[178] M. Backovic, K. Kong, and M. McCaskey, *MadDM v.1.0: Computation of Dark Matter Relic Abundance Using MadGraph5*, Phys. Dark Univ. **5-6** (2014) 18–28, [arXiv:1308.4955].

[179] M. Backovic, A. Martini, O. Mattelaer, K. Kong, and G. Mohlabeng, *Direct Detection of Dark Matter with MadDM v.2.0*, Phys. Dark Univ. **9-10** (2015) 37–50, [arXiv:1505.04190].

[180] LHC Dark Matter Working Group website, 2015. Available at http://lpcc.web.cern.ch/content/lhc-dm-wg-wg-dark-matter-searches-lhc.

[181] **ATLAS** Collaboration, *Search for top-squark pair production in final states with one lepton, jets, and missing transverse momentum using $36\,fb^{-1}$ of $\sqrt{s}$ = 13 TeV pp collision data with the ATLAS detector*, JHEP **06** (2018) 108, [arXiv:1711.11520].

[182] R. C. Cotta, J. L. Hewett, M. P. Le, and T. G. Rizzo, *Bounds on Dark Matter Interactions with Electroweak Gauge Bosons*, Phys. Rev. **D88** (2013) 116009, [arXiv:1210.0525].

[183] U. Haisch, A. Hibbs, and E. Re, *Determining the structure of dark-matter couplings at the LHC*, Phys. Rev. **D89** (2014) 034009, [arXiv:1311.7131].

[184] A. Crivellin, U. Haisch, and A. Hibbs, *LHC constraints on gauge boson couplings to dark matter*, Phys. Rev. **D91** (2015) 074028, [arXiv:1501.00907].

[185] M. Bauer, U. Haisch, and F. Kahlhoefer, 2017. Available at https://github.com/LHC-DMWG/model-repository/blob/master/models/Pseudoscalar_2HDM/README.txt.

[186] R. D. Ball et al., *Parton distributions with LHC data*, Nucl. Phys. **B867** (2013) 244–289, [arXiv:1207.1303].

[187] **NNPDF** Collaboration, R. D. Ball et al., *Parton distributions for the LHC Run II*, JHEP **04** (2015) 040, [arXiv:1410.8849].

[188] T. Sjöstrand, S. Ask, J. R. Christiansen, R. Corke, N. Desai, P. Ilten, S. Mrenna, S. Prestel, C. O. Rasmussen, and P. Z. Skands, *An Introduction to PYTHIA 8.2*, Comput. Phys. Commun. **191** (2015) 159–177, [arXiv:1410.3012].